STRESS PARTITIONING IN FCC THIN METAL FILMS WITH MIXED TEXTURE

A Dissertation

Presented to the Faculty of the Graduate School

of Cornell University

In Partial Fulfillment of the Requirements for the Degree of

Doctor of Philosophy

by

Aaron Michael Vodnick

February 2010

STRESS PARTITIONING IN FCC THIN METAL FILMS WITH MIXED TEXTURE

Aaron Michael Vodnick, Ph.D.

Cornell University, 2010

Thin FCC metal films are used in a wide range of micro- and nano-fabricated devices. These films may support stresses up to an order of magnitude greater than would be predicted based on bulk scaling laws. These stresses drive failure mechanisms and are one of the main limitations on the reliability of film-containing devices. Thus, there has been a great deal of interest in thin film mechanical behavior. In experimental studies, a homogeneous equal-biaxial stress state in the plane of the film is typically assumed and data are analyzed accordingly. However, annealed FCC metal films tend to have columnar grained microstructures with grain size on the order of the film thickness and strong fiber texture with (111) and/or (100) planes parallel to the plane of the film. Due to anisotropy, these orientations often have very different elastic stiffnesses both in and out of the film plane. Thus, for a uniform applied strain (e.g. thermal strain), very different three-dimensional stress states should be expected in each orientation. In this thesis experimental and analytical methods for accurately determining the stress states in films with mixed (111)/(100) texture are presented. Synchrotron x-ray diffraction was used to characterize the strains in each texture component individually during thermal cycling of Cu films on Si substrates. A new analysis method is presented that allows the 3-D stress states in the different texture components to be determined with reasonable accuracy. Stress states are found to be dramatically different from the simple biaxial stresses typically assumed. Further analysis allowed the plastic strain and the geometrically necessary dislocation density

in each texture component to be determined throughout the temperature cycle. Again, results are quite different from those found following the biaxial assumption. Finite element simulations of stress states as a function of grain aspect ratio and texture volume fractions confirmed that the experimental results were reasonable, and detailed studies were conducted to explore the effects of inhomogeneous stresses on x-ray peak widths and on texture formation. This work suggests that many models of thin film mechanical behavior should be revised.

BIOGRAPHICAL SKETCH

Aaron was born and raised in Cloquet, MN. He attended the University of Minnesota, Twin Cities in Minneapolis, MN, earning a B.S. in Materials Science & Engineering. While at the University of Minnesota, Aaron worked as a Research Assistant in the lab of Robert F. Cook, where he performed research on the fracture mechanics of brittle materials using indentation techniques and developed the motivation to attend graduate school, against the best advice of the graduate students he was working with. Immediately after leaving the University of Minnesota, Aaron moved to Ithaca, NY to begin graduate school in Materials Science & Engineering at Cornell. Throughout Aaron's time at Cornell he was involved in G-Line, a graduate student oriented beamline at the Cornell High Energy Synchrotron Source (CHESS). Upon completion of his Ph.D., Aaron is looking forward to gaining industry experience.

ACKNOWLEDGEMENTS

A large amount of gratitude is owed to the many people who have contributed to the work in this thesis and have offered support throughout the years. First and foremost, thank you to my advisor, Shefford Baker, without whom none of this would be possible, and has taught me that the Devil is, indeed, in the details. Thank you to my committee members, Professors Joel Brock and Paul Dawson for useful discussions and ideas. Also, thank you to Matt Miller for useful insights and questions regarding x-ray strain measurements.

Support for the research in this thesis has been provided by a variety of sources. I have been privileged to receive partial support through an Applied Materials Graduate Fellowship and a Cornell McMullen Fellowship. Aspects of this work are based upon research conducted at the Cornell High Energy Synchrotron Source (CHESS) which is supported by the National Science Foundation and the National Institutes of Health/National Institute of General Medical Sciences under NSF award DMR-0225180. Funding was also provided through the National Science Foundation (INT-0233283) and the Department of Energy (DE-FG02-02ER46001). Partial support for ANSYS was provided by the Swanson Engineering Simulation Program, thanks to Rajesh Bhaskaran.

Thank you to many past members of the Baker Research Group, who deserve much of the credit for the work in this thesis. Thank you to David Nowak for getting me started with work at G-Line and providing a background in x-ray strain measurements. Thank you to Ray Fertig for many fruitful discussions, always impressing me with his depth of knowledge and never failing to point out holes in my logic. Thank you to Robert Knepper and Michael Lawrence for preparation of films and for being a springboard for ideas.

Thank you to the entire CHESS staff, especially Arthur Woll and Detlef Smilgies for all the work maintaining the G2 Hutch, and to all the G-Line students, especially Daniel Blasini, Yi Li and John Ferguson for help with equipment and experiments.

Without my experiences as an undergraduate researcher at the University of Minnesota I may have never began graduate school. For this, thank you to Robert Cook and his graduate students Michael Hughey, Yvete Toivola and Dylan Morris.

Finally, thank you to all those people who have helped me to navigate graduate school and Ithaca, especially Dan Bernards, Matt Lloyd and Becky Kessler. A special thank you to my parents, Margaret and Jim Vodnick, for their constant support.

TABLE OF CONTENTS

LIST OF FIGURES

LIST OF TABLES

CHAPTER 1

Introduction

1.1 MOTIVATION

Thin face-centered-cubic (FCC) films are used in a variety of technologies. For example, Al and Cu films serve as interconnect materials in micro-electronic and –mechanical devices [1-3], Al and Ag films are used as optical reflectors [4-6] and biosensors [7], Au is used as a substrate for self-assembled-monolayers [8], and Pt films are used as catalysts [9]. While FCC films are selected for these applications for their electronic, optical, or chemical properties, it is their mechanical behaviors that often lead to issues with failure and reliability. Thin films commonly support extreme stress states (up to an order of magnitude larger than their bulk counterparts), which can be detrimental to performance due to a variety of processes, such as deadhesion, fracture, voiding and hillocking, or elastic distortion [1, 3]. Thus, understanding the stress states and resultant deformation behaviors within these films will allow for improved device performance, reliability and manufacturability.

The most common technique for characterization of stresses in FCC thin films has been based on the curvature induced in the substrate through a stress interaction with the film during thermal cycling (*i.e.* substrate curvature measurements) [1, 10, 11]. Such measurements can provide accurate values for the average stress interaction with the substrate, but provide no information on the distribution of stresses within a film. Many other techniques for characterizing stresses within thin films have been developed [12-14]. Similar to substrate curvature measurements, these have typically also treated the films and stress states as both homogeneous and isotropic. However, many failures are expected to occur in regions of high stresses, such that knowledge of

the stress distributions is important for furthering our understanding of stress driven processes.

Annealed FCC metal films typically have highly oriented columnar-grained microstructures with (111) and (100) crystal orientations normal to the film plane [15], commonly with mixed texture. Due to anisotropy, these two texture components can exhibit very different mechanical behaviors [1, 16, 17], and knowledge of the stress states in each orientation will help the understanding of stress driven phenomena. X-ray diffraction has been used to experimentally characterize the average strains within each texture component individually [16, 17], though these investigations have relied on the assumption that out-of-plane stresses are zero everywhere in the film, when in fact large out-of-plane stresses may be expected in each orientation. Finite element models (FEM) of mixed texture microstructures have provided information on the partitioning of stresses between the (111) and (100) orientations, confirming out-of-plane stresses may be expected, but have been limited in scope; both in the microstructures investigated and accompanying analyses of stress partitioning on stress driven processes. Stress states in mixed texture metal films have been, thus far, poorly understood.

This thesis is dedicated to understanding how stresses are partitioned across the microstructure of metal films having mixed (111)/(100) texture using experimental, analytic and simulation approaches, and applying this knowledge of stress partitioning to enhance the understanding of stress driven phenomena.

1.2 STRUCTURE OF THIS THESIS

This thesis is organized into eight chapters. This first chapter provides background information on thin film strains, microstructures, elastic constants, stress states, and deformation processes. Chapter 2 contains a review of the current status of thin film x-

ray strain measurements. Chapters 3-6 are stand alone papers prepared for publication as journal articles, and Chapter 7 has been published as a Materials Research Society Conference Proceedings. In Chapter 3 we present a new x-ray strain analysis which allows the triaxial stress states in the (111) and (100) texture components of a mixed texture film to be determined, report the first experimentally characterized triaxial stress states in each texture component of a Cu film during thermal cycling, and discuss the impacts of the newly observed triaxial stress states on stress driven processes. In Chapter 4 we use the x-ray analysis of elastic strains from Chapter 3 to derive a new method to calculate the required changes in plastic strains and dislocation densities within each texture component over a temperature cycle, and use this to accurately investigate the strain hardening and anelastic behaviors of each texture components of a Cu film, finding the (111) orientation never deforms purely elastically. In Chapter 5, we present the results of finite element models (FEM) of idealized mixed texture Cu film microstructures to describe the impacts or grain aspect ratio and film texture and on stress partitioning, and validate the reasonableness of the experimental stress states we reported in Chapter 3. We also utilize these FEM results to produce, for the first time, a model which can explain the stability of mixed (111)/(100) texture films—a response to a long-standing question in the thin film community. Chapter 6 is a letter combining information from Chapters 4 and 5 in order to describe the behavior of diffraction peak widths in FCC thin films during thermal cycling, demonstrating that peak widths are not a good indicator of plastic deformation alone and are substantially impacted by inhomogeneous strains from texture interactions. In Chapter 7, an example of future work is presented which combines concepts from the previous chapters to investigate texture evolution using *in-situ* x-ray diffraction measurements. Finally, in Chapter 8 the contributions from the previous chapters are summarized and suggestions for future work are proposed which

make use of the knowledge of and tools to characterize stress partitioning developed in this thesis in order to understand stress driven processes.

1.3 SOURCES OF STRAIN

In general there are many possible sources of strains in thin films, including substrate coherence effects, ion bombardment, interfacial stresses, thermal expansion mismatch, microstructural evolution, or even external loading [18]. However, for annealed metal films on amorphous layers on rigid substrates (*i.e.* films on a Si substrate with an amorphous barrier), the topic of this thesis, the primary sources of strain are due to thermal expansion with the substrate and densification during grain growth.

Differential thermal expansion between a film and the substrate to which it is attached is the most commonly discussed source of strains in metal films, since changing the temperature is a simple and convenient approach to imposing strains for mechanical testing. For a change in temperature from an initial temperature, T_0, to some final temperature, T_f, the thermal strain imposed is described by the equation

$$\varepsilon_{Th} = \int_{T_0}^{T_f} \left(\alpha_s(T) - \alpha_f(T)\right) dT \,, \tag{1.1}$$

where $\alpha_s(T)$ and $\alpha_f(T)$ are the temperature dependent thermal expansion coefficients of the film and substrate, respectively. Since the thermal expansion coefficients of cubic materials are isotropic, changes in temperature impose equal biaxial strains within the film plane. Throughout this thesis, thermal expansion coefficients from ref.'s [19, 20] are used.

Strains in metal films on substrates can also arise due to microstructural changes. Metal films on amorphous layers are typically polycrystalline, and changes in the average crystallite size will change the film strain due to a change in the free

volume stored in grain boundaries. The change in strain $\Delta\varepsilon$ depends on the initial, d_i, and final, d_f, grain diameters, described by

$$\Delta\varepsilon = \delta\left(\frac{1}{d_i} - \frac{1}{d_f}\right), \tag{1.2}$$

where δ is the grain boundary width [21, 22]. The strains imposed by grain growth are equal biaxial in the film plane if the grains are equiaxed in the film plane.

The elastic strain tensor resulting from these sources of strain is of the form

$$[\varepsilon] = \begin{bmatrix} \varepsilon_f & 0 & 0 \\ 0 & \varepsilon_f & 0 \\ 0 & 0 & \varepsilon_3 \end{bmatrix}, \tag{1.3}$$

where ε_f are the strains in the film plane and ε_3 is the strain along the film normal direction, resulting from Poisson contraction. The shear strains must be zero since the free surface of the film is traction free and the film must be rotationally symmetric.

The average stress state in the film corresponding to the strains in Eq. 1.3, for a homogeneous isotropic material, is of the form

$$[\sigma] = \begin{bmatrix} \sigma_f & 0 & 0 \\ 0 & \sigma_f & 0 \\ 0 & 0 & 0 \end{bmatrix}, \tag{1.4}$$

where σ_f are the stresses in the plane of the film, and the out-of-plane stress is zero since the free surface cannot support normal tractions. The relevant elastic modulus relating the stresses to strains is the "biaxial modulus" $Y = \sigma_f/\varepsilon_f = E/(1-\nu)$ with E the Young modulus and ν the Poisson ratio. Of course, the stress state is not always so simple, as will be demonstrated throughout this thesis.

The average in-plane stress response of a film due to thermal (Eq. 1.1) and densification (Eq. 1.2) strains, typical of reports in the literature [1, 23-25], is

demonstrated in Figure 1.1. This plot shows the biaxial stress in the plane of the film, σ_f, *vs.* temperature for a 500 nm Cu film on a Si substrate, with SiN_x barrier and passivation layers. Two temperature cycles are shown and stresses were measured using substrate curvature. Initially, the film was in its as deposited state, that is, a small grain size. On the first heating cycle, the stress initially begins to become more compressive due to differential thermal expansion. After the film reaches a sufficient temperature, grain growth occurs and the densification strains cause the stress to become more tensile near 150°C. After grain growth slows, the stress again becomes more compressive up to about 400°C, above which the stress decreases due to decreasing film strength at high temperature. On cooling during the first cycle, differential thermal expansion increases the film stress and the film strain hardens to a large stress at room temperature.

On the second heating cycle in Fig. 1.1, the stress initially decreases, passing through zero, after which the film strain hardens to up the maximum temperature. An interesting feature of this behavior is that the film begins to even yield before the stress becomes compressive (This behavior is discussed further in §1.8.2). On cooling of the second cycle, the stress in the film first changes rapidly becoming tensile as the film deforms elastically, after which the film strain hardens to roughly the same stress at room temperature. Subsequent cycles will exhibit repeatable stress-temperature behavior similar to that of the second cycle.

1.4 THIN FILM MICROSTRUCTURE

Annealed FCC metal films on amorphous barrier layers have highly oriented microstructures, with columnar grains that traverse the film thickness. For FCC films, grains have (111) or (100) crystal plans parallel to the plane of the film, in order to minimize the surface energy or strain energy of the film, respectively (more about this

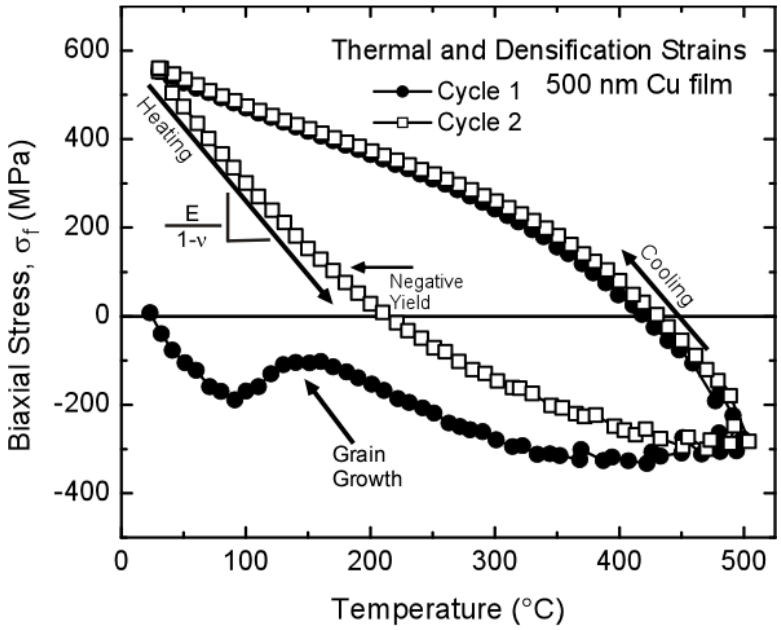

Figure 1.1: Demonstration of the effects of thermal and densification strains on an as-deposited 500 nm Cu film over the first two temperature cycles [Unpublished data courtesy of Robert Knepper, Cornell University]. After the second temperature cycle the microstructure is stable and the stress-temperature loop is repeatable.

in §1.6) [15, 22, 26]. In the plane of the film, grain orientations are randomly oriented about the film normal, referred to as a fiber texture. A cross section illustration of the microstructure is presented in Figure 1.2. For anisotropic materials, the different texture components can have very different elastic and plastic properties (§1.5, §1.8).

The grain diameters in thin films often follow a lognormal distribution,

$$f(d) = \frac{1}{\sigma d\sqrt{2\pi}} \exp\left\{ \frac{-(\ln(d) - \ln(d_{50}))^2}{2\sigma^2} \right\} \tag{1.5}$$

where d_{50} is the median grain size and σ is the lognormal standard deviation [27, 28]. For typical films, the median grain size is typically on the order of the film thickness [15, 27]. However, in some cases grain diameters have bimodal distributions [28, 29] or can exhibit abnormal grain growth in which a subset of grains, typically (100), becomes substantially larger than the film thickness [15, 27, 28].

1.5 ELASTIC ANISOTROPY

As a result of crystal anisotropy, the (111) and (100) texture components of FCC metal films can have very different elastic constants relative to the film system. Both of these orientations have biaxial moduli which are transversely isotropic, such that for a perfect (111) or (100) textured film, a uniform applied strain in the film plane (Eq. 1.3) results in a stress that is also invariant in the plane of the film (Eq. 1.4). However, the biaxial modulus for each orientation, Y^{hkl}, relating the stresses and strains are very different in the two orientations,

$$Y^{111} = \frac{\sigma_f}{\varepsilon_f} = \frac{6C_{44}(C_{11} + 2C_{12})}{C_{11} + 2C_{12} + 4C_{44}}, \tag{1.6}$$

and

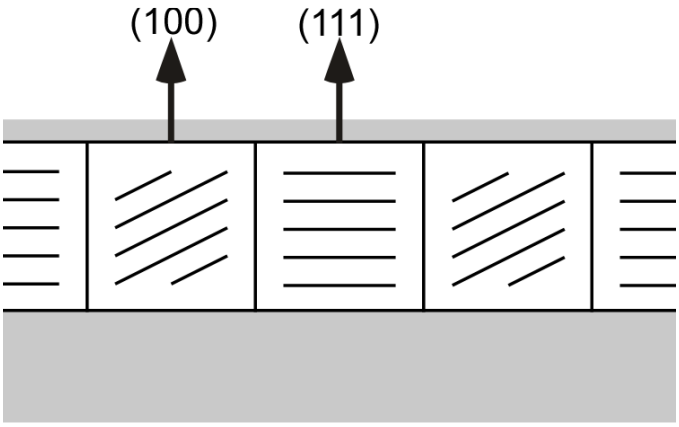

Figure 1.2: Cross section illustration of the microstructure of a passivated FCC metal film with mixed texture on an amorphous layer. Columnar grains have (100) or (111) crystal orientations along the film normal direction. In the film plane, these grains are randomly oriented about the film normal.

$$Y^{100} = \frac{\sigma_f}{\varepsilon_f} = C_{11} + C_{12} - \frac{2C_{12}^2}{C_{11}}, \tag{1.7}$$

where C_{ij} are the single crystal elastic constants [1]. For all FCC metals, the stiffness of the (111) texture is larger than that of the (100) orientation, though the difference depends on the anisotropy of the crystal. Values of Y^{111} and Y^{100}, calculated using elastic constants from ref.'s [30, 31], for selected FCC metals, are listed in Table 1, demonstrating the large difference between these values that may exist for anisotropic materials. Due to elastic anisotropy, in FCC metal films of the same material, but with different textures, very different stress states may arise.

Elastic anisotropy also produces very different elastic behaviors in the out-of-plane direction. That is, for an applied biaxial in-plane strain, the resulting out-of-plane Poisson contractions are a strong function of orientation [32, 33]. The relevant constant is the biaxial Poisson ratio $v^{hkl} = -\varepsilon_3^{hkl} \big/ \varepsilon_f^{hkl}$, which for the (111) and (100) texture components can be shown to be

$$v^{111} = -\frac{\varepsilon_3^{111}}{\varepsilon_f^{111}} = -\left(\frac{2C_{11} + 4C_{12} - 4C_{44}}{C_{11} + 2C_{12} + 4C_{44}} \right), \tag{1.8}$$

and

$$v^{100} = -\frac{\varepsilon_3^{100}}{\varepsilon_f^{100}} = -\left(\frac{2C_{12}}{C_{11}} \right), \tag{1.9}$$

respectively [16]. Values of the biaxial Poisson ratio for (111) and (100) oriented films are summarized in Table 1for selected FCC metals.

1.6 TEXTURE THERMODYNAMICS

The (111) and (100) texture components of FCC metal films arise due to competing forces of interfacial and strain energies in order to minimize the total energy of the film, as presented by Thompson [15, 22, 26]. Interfacial energies are minimized by

Table 1.1: Elastic constants for the (111) and (100) texture components of selected FCC metals. Due to elastic anisotropy, large differences in the biaxial modulus, Y^{hkl}, and biaxial Poisson ratio, ν^{hkl}, are common between the two texture components.

	Y^{111} (GPa)	Y^{100} (GPa)	Y^{111}/Y^{100}	ν^{111}	ν^{100}
Copper	261	115	2.27	0.73	1.44
Silver	169	75	2.25	0.90	1.51
Gold	191	81	2.36	1.25	1.68
Aluminum	114	99	1.15	1.03	1.16

(111) textured films, since (111) planes have the smallest interfacial energies, γ^{111},of all FCC grain orientations, while (100) oriented films have the largest interfacial energy, γ^{100}. Strain energies are minimized in (100) oriented films, which have the smallest biaxial modulus of all FCC grain orientations, compared to (111) textured films which have the largest biaxial modulus.

The thermodynamics of thin film texture is considered by comparing the total energy densities of two films with the same thickness and strain, but with different orientations. The difference in interfacial energy density between the (111) and (100) oriented films, ΔW_i, is given by

$$\Delta W_i = \frac{\gamma^{111} - \gamma^{100}}{h}, \tag{1.10}$$

where h is the film thickness. Since this is an energy per unit volume, its influence decreases as films become thicker.

The strain energy density within a film under an equal biaxial strain, ε, is given by $W = Y\varepsilon^2$. The difference in strain energy densities between a (111) and (100) oriented film with the same strain, ΔW_ε, is then

$$\Delta W_\varepsilon = \left(Y^{111} - Y^{100}\right)\varepsilon^2. \tag{1.11}$$

The influence of these two driving forces on film texture is often illustrated on a "Texture Map" of the texture equilibrium condition, when $\Delta W_i = \Delta W_\varepsilon$. This condition is illustrated in Figure 1.3 as a plot of the film strain *vs.* film thickness. For thin films and small strains (111) texture is expected, while for thick films and large strains a (100) texture is predicted through this model; a sharp texture transition is expected at the equilibrium boundary. Though this general trend is observed experimentally, a sharp transition from (111) to (100) texture with increasing thickness is rarely observed. Instead, with increasing thickness the texture gradually transitions from (111) to (100) texture, with a broad thickness range of films with

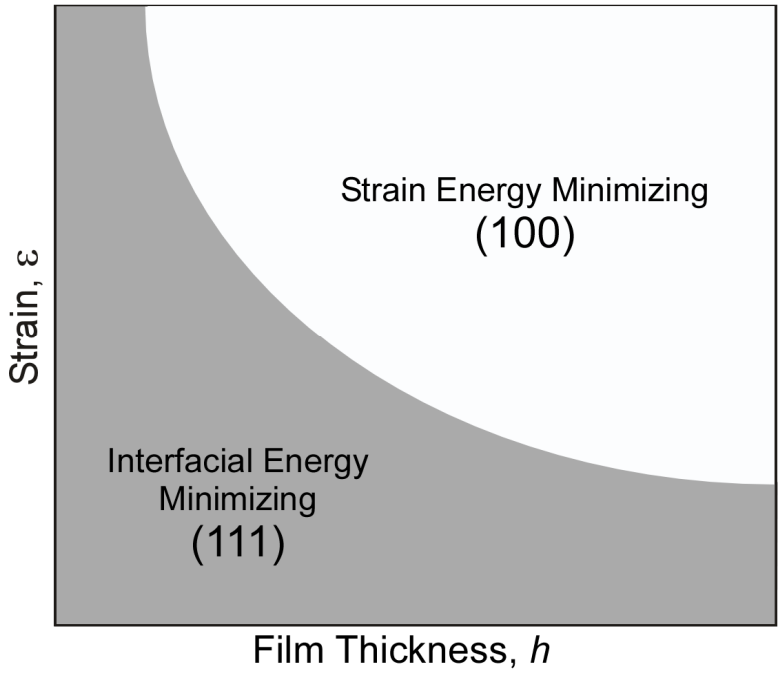

Figure 1.3: Texture map of the equilibrium boundary between an interfacial energy and strain energy from the Thompson texture model. For thin films and smalls trains, the interfacial energy minimizing (111) texture is expected, while at thicker thicknesses and larger strains (100) texture is preferred. At the equilibrium boundary a sharp (111)-(100) texture transition is expected. This simple model cannot explain the stability of mixed texture films.

mixed texture [17, 29, 34, 35]. This is the primary failure of Thompson's texture model—it cannot predict or explain the stability of mixed texture films. An explanatory model for mixed texture film stability is suggested in Chapter 5. In Chapter 7, the strain energy driving forces within (111) and (100) oriented grains within an evolving microstructure of a Ag film, as characterized using x-ray diffraction methods, are presented.

1.7 TEXTURE INTERACTIONS

Elastic anisotropy is very important to stress partitioning in mixed texture metal films. For instance, due to the large difference in the biaxial moduli between the two texture components, a large in-plane discontinuity in the elastic constants exists at (111)/(100) texture boundaries. This will result in significant grain interactions at (111)/(100) boundaries, since for a given in-plane strain these orientations support very different stresses. However, in order to maintain equilibrium at texture boundaries, tractions on each side of the boundary must balance, requiring the in-plane stresses in each orientation acting on this boundary, σ_f^{hkl}, to be equal. This requires significant strain transfer from one orientation to the other, likely through grain boundary bowing, or even sliding along the film/substrate or film/passivation interfaces in cases of weak adhesion.

Since the film is attached to a substrate, strain transfer between grains is limited to a region within a few film thicknesses of the texture boundary, as has been shown through analytic and numerical models of similar geometries [36-38]. Therefore, in-plane stress gradients will occur near (111)/(100) boundaries, with equal in-plane stresses in each orientation at the boundary, decaying to the value prescribed by the biaxial moduli after a few film thicknesses from the boundary. These in-plane stress gradients require shear stresses, τ_{f3}, to arise near texture boundaries in order to

satisfy the equilibrium conditions, $\sigma_{ij,j} = 0$ [39]. A schematic of how the normal and shear stress components may vary near a (111)/(100) boundary, at some constant height in the film, is shown in Figure 1.4. While stress states within individual grains are indeed expected to be complex (likely with more than these two stress components), the average of the shear stresses over each texture component in a film must sum to zero resulting in a simple stress state over each orientation, on average. This fact is due to the rotationally symmetric film microstructure; for every boundary in a film similar to Figure 1.4 there is also a boundary with an opposite stress gradient, for which the shear stresses are negative, such that total shear stress over each texture component is expected to be null. In this thesis, we will focus on the *average* stresses in the (111) and (100) texture components of mixed texture films, for which the average principal stress/strain axes must coincide with film coordinates (*i.e.* Eq. 1.3). While details of stress gradients within each texture component may be important to understanding their behaviors, knowledge of the average stress states driving deformation behaviors is an important step toward this goal and will be the focus of this thesis.

As a result of stress interactions occurring over distances of roughly a few film thicknesses from the grain boundary [36-38], the average stress partitioning in mixed texture films is a function of the distance between texture boundaries, which is related to the grain size. For very wide grains relative to the film thickness (Figure 1.5, Bottom Left), under an applied thermal strain, the region near the boundary becomes small relative to the total grain volume such that, on average, the same strain is applied to each orientation (*i.e.* isostrain) and the ratio of the in-plane stresses within each texture component approaches the ratio of the biaxial moduli, $\sigma_f^{111} \big/ \sigma_f^{100} = Y^{111} \big/ Y^{100}$. In the other limit, for grains that are very narrow relative to the film thickness (Figure 1.5, Bottom Right), the interaction region near the boundaries become large relative to

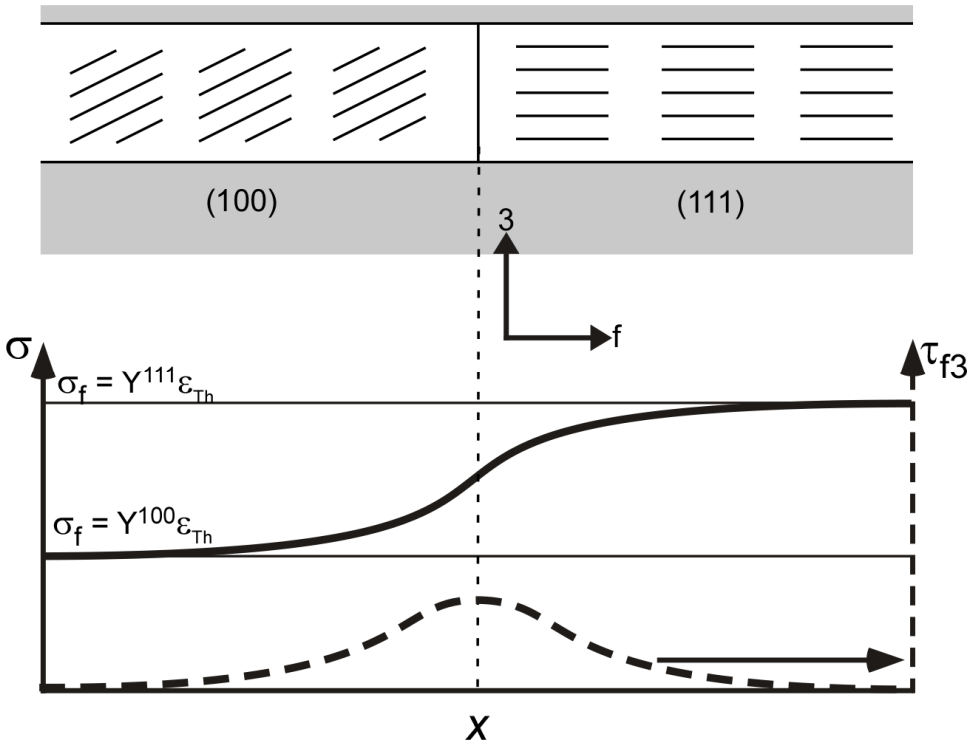

Figure 1.4: Schematic of how the in-plane normal and shear stress components may vary near a (100)/(111) texture boundary at some constant height across the film. A boundary with the opposite orientation will have shear stresses of the opposite sign, such that the average shear stress over each texture component must sum to zero when considering the fiber texture in the film. While the stress state near any one boundary will be much more complex, likely with other non-zero stress components and a dependence on the height in the film, the goal of this thesis is to determine the average stresses within each texture component.

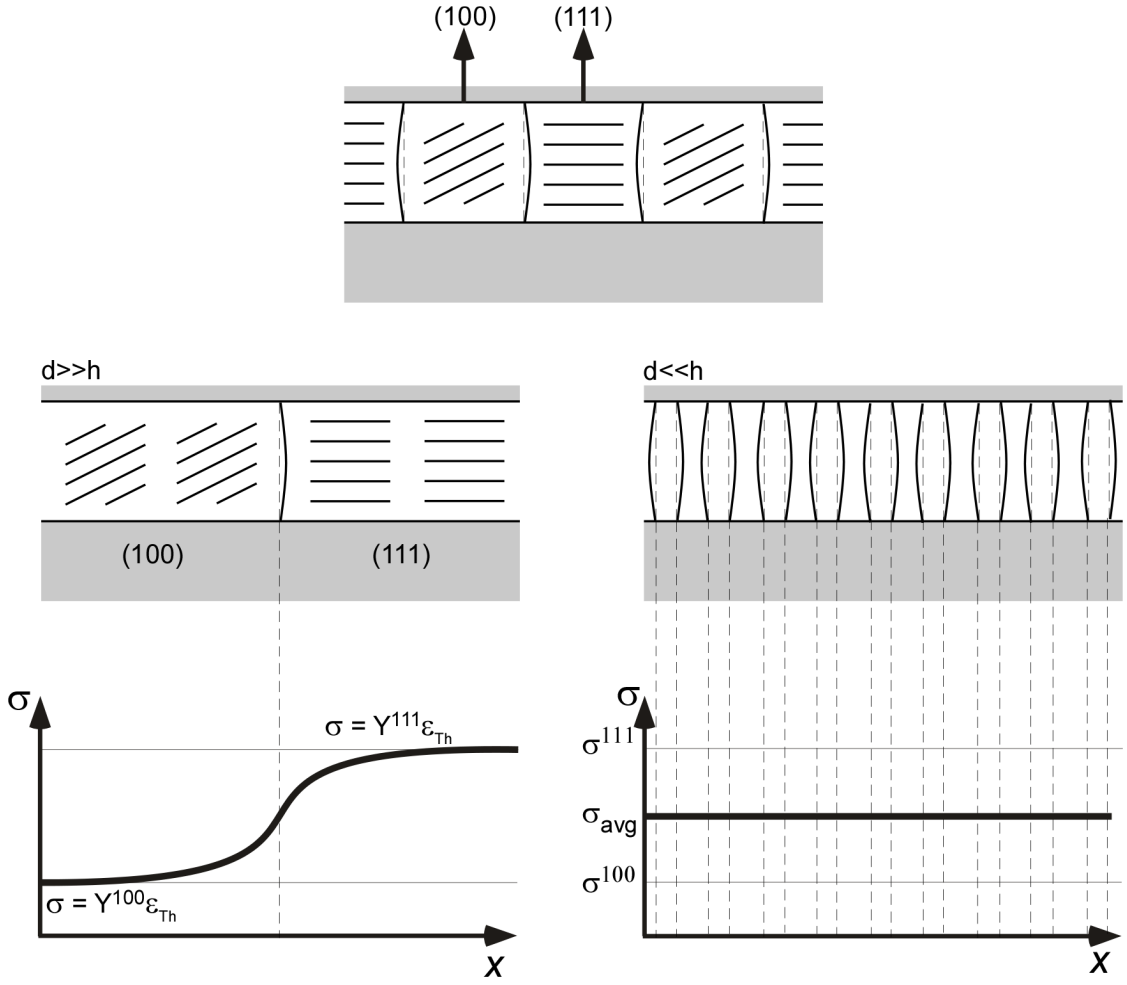

Figure 1.5: (Top) Cross section of a thin film with columnar grains and (111) and (100) crystal directions normal to the film plane. Elastic discontinuities at texture boundaries will lead to grain boundary bowing in order to equilibrate stresses across the boundary. For grains that are very wide relative to the film thickness (Bottom left), stresses relax away from the boundary such that on average an isostrain case is expected. For grains narrow relative to the film thickness (Bottom Right), there is no room between boundaries for stress redistribution and the in-plane stresses relax to some average value, σ_{avg}.

the grain volume and there is no room for stress gradients to redistribute in-plane stresses between boundaries, such that each texture component will be subjected to approximately the same in-plane stress, $\sigma_f^{111} \big/ \sigma_f^{100} = 1$ (*i.e.* isostress).

These texture interactions are important, since many failure mechanisms may occur in regions of extreme stress, and all stress driven phenomena in thin films will depend on how the stresses are distributed throughout the microstructure. Thus, it has been the aim of numerous experimental investigations to characterize the stresses within the (111) and (100) orientations individually using x-ray diffraction [16, 17, 40-42]. In these investigations, it was reported that the stress in the (111) orientation was much larger than the stress in the (100) texture, as may be expected based on the difference in the biaxial moduli, with behaviors very close to isostrain. However, this isostrain behavior is surprising considering that strain transfer is expected to occur over distances of roughly the film thickness, which is on the order of the grain diameter.

A common thread in each of these of these experimental investigations [16, 17, 40-42] was the reliance on the common assumption for thin films that the out-of-plane stress is zero everywhere in the film ($\sigma_3 = 0$). This neglects the possibility for significant out-of-plane texture interactions due to differences in the biaxial Poisson ratios (Eq.'s 1.7-8), as have been demonstrated by Wikstrom *et al.* using finite element models [43, 44]. Thus, systematic errors in the x-ray measurements may be expected [45]. In Chapters 3 and 5 the $\sigma_3 = 0$ assumption used in these x-ray analyses is addressed—out-of-plane texture interactions are described and we demonstrate that for typical film microstructures the in-plane interactions should in fact be closer to isostress, with large out-of-plane stresses.

1.8 PLASTIC DEFORMATION

Dislocation motion in FCC metals occurs on close packed {111}-type slip planes along $\vec{b} = a/\sqrt{2}\langle 110 \rangle$-type Burgers vectors. Due to the strong texture of FCC metal films, and simple form of the strain tensor (Eq. 1.1), shear stresses are only resolved on certain slip systems in each grain orientation. That is, on average, no shear stress acts on burgers vectors which lie within the film plane, limiting the number of active slip systems in the (111) and (100) texture components.

Figure 1.6 illustrates the active {111}-type slip systems in each grain orientation. Within each texture component, all active slip systems have angles between the slip plane and the film normal directions, ϕ, and between the Burger's vector and the film normal direction, λ, that are all equal [1, 46, 47]. Thus, since the stress state is transversely isostropic about the film normal, the same resolved shear stresses acts on each active slip system. Active slip systems for each film orientation will therefore exhibit identical behaviors, on average, and many dislocation processes (*i.e.* yield, anelasticity) can be considered by analyzing a single slip system.

1.8.1 Thin film strength

The truncated geometry of thin films places an intrinsic constraint on the motion of dislocations. This is illustrated in Figure 1.7, which demonstrates that as a dislocation moves through a passivated film (referred to as a threading dislocation), it must deposit dislocation line length at the film/substrate and film/passivation interfaces (referred to as a misfit dislocation). This has a pervasive influence on dislocation behaviors within thin films and directly impacts their yield behaviors.

The influence of the interfacial misfit dislocation on yield has been described by Freund [48] and Nix [1], based on a large body of work describing the stress fields

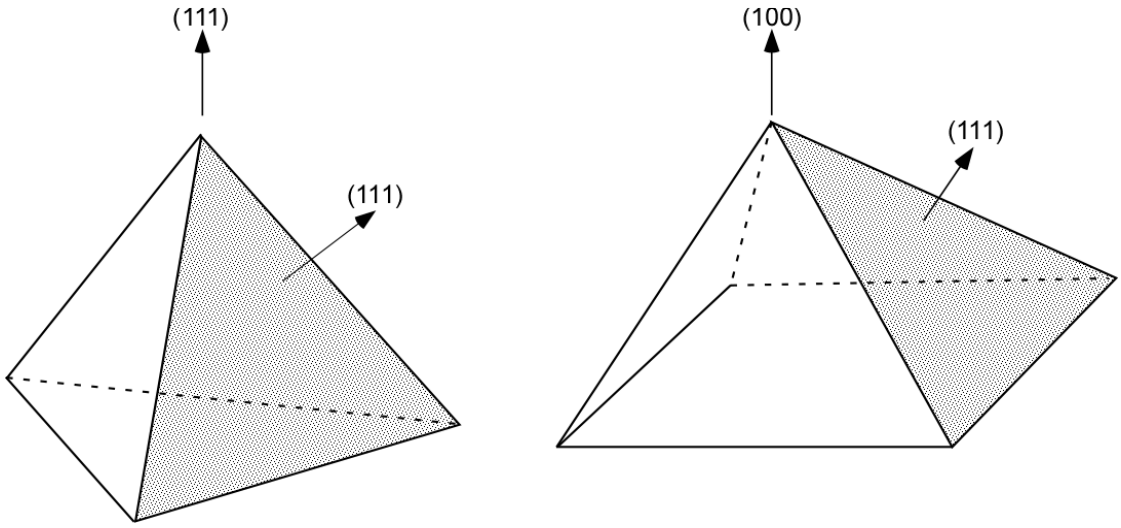

Figure 1.6: Active {111} type slip planes in the (111) and (100) texture components of an FCC metal film. Burgers vectors along {110} directions are on the edges of the pyramids. No shear stress is resolved on Burgers vectors lying within the film plane, and all inclined Burgers vectors have similar geometries with respect to the stress state thus exhibiting similar behaviors.

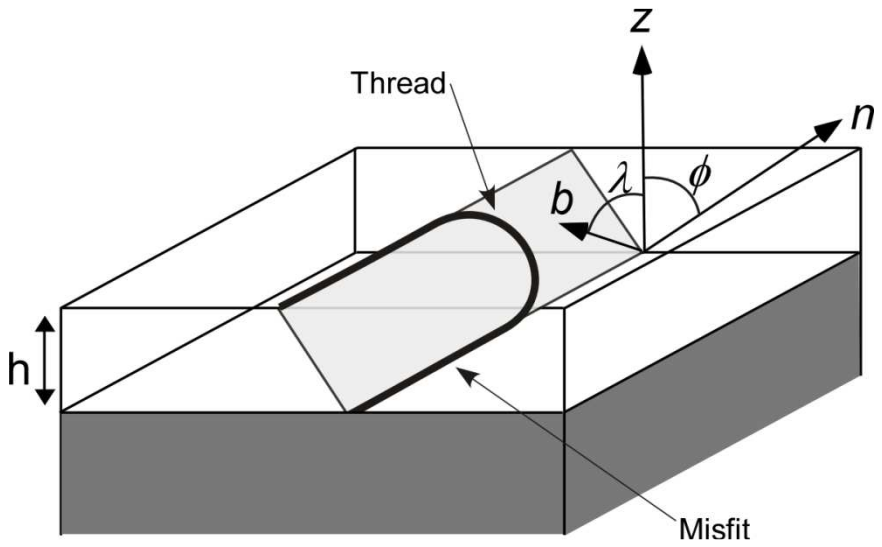

Figure 1.7: Channeling dislocation model with the threading dislocation through the film thickness and the misfit dislocation at the film/substrate and film/passivation interfaces (passivation layer not shown). The slip system is defined by the angle, λ, between the Burgers vector, *b*, and film normal, *z*, and the angle ϕ, between the slip plane normal, *n,* and *z*. The constraint on the motion of dislocation thin films leads to large film strengths [1] and significant anelastic behavior [48].

around dislocations at interfaces (for example [49-52]). The energy per unit length associated with the misfit dislocation strain fields is given by [1]

$$W_m = \frac{b^2}{4\pi(1-\nu)}\left[\frac{2\mu_f\mu_s}{(\mu_f+\mu_s)}\ln\left(\frac{\beta_s h}{b}\right)+\frac{2\mu_f\mu_p}{(\mu_f+\mu_p)}\ln\left(\frac{\beta_p t_p}{b}\right)\right], \tag{1.12}$$

where b is the magnitude of the Burgers vector, μ_f, μ_s, and μ_p are the shear moduli of the film, substrate, and passivation, respectively, h and t_p are the film and passivation thickness, respectively, and β_s and β_p are constants on the order of one for the substrate and passivation interfaces, respectively. This misfit dislocation energy must be overcome by the work done on the threading dislocation for the thread to advance. The work on the threading dislocation as it is driven from the top to the bottom of the film is of the form $W_t = \tau b x$, where τ is the shear stress resolved on the dislocation and x is the distance the dislocation travelled,

$$W_t = \sigma\cos\lambda\cos\phi b\frac{h}{\sin\phi}. \tag{1.13}$$

The biaxial stress at which $W_t = W_m$ has been termed the "channeling stress",

$$\sigma_{ch} = \frac{\sin\phi}{\cos\lambda\cos\phi}\frac{b}{4\pi(1-\nu)h}\left[\frac{2\mu_f\mu_s}{(\mu_f+\mu_s)}\ln\left(\frac{\beta_s h}{b}\right)+\frac{2\mu_f\mu_p}{(\mu_f+\mu_p)}\ln\left(\frac{\beta_p t_p}{b}\right)\right]. \tag{1.14}$$

Due to the different slip system geometries, the critical stress for dislocation advancement in (111) and (100) oriented films is different by a factor of roughly 1.7 [53], regardless of the film material. Variations of this model to account for the presence or lack of passivation layers [1] and grain boundaries in polycrystalline films [54] have also been considered. In Chapter 3, it is demonstrated how this yield criterion is altered in a triaxial stress state within different texture components of a mixed texture film.

1.8.2 Anelasticity

A direct corollary of the dislocation channeling behavior in Sec. 1.8.1 is that as the film stress falls below the channeling stress, thermodynamics requires the threading dislocation to reverse direction in order to recover the excess energy associated with its misfit dislocation. This phenomena results in a significant Bauschinger effect, also called “anelastic recovery”, “negative yield”, or “anomalous behavior”, which is commonly observed in thin films [11, 14, 25, 55]. This negative yield behavior is indicated on heating of the second temperature cycle for a passivated 500 nm Cu film in Figure 1.1. X-ray strain measurements are used to investigate anelastic behaviors within (111) and (100) texture components of a mixed texture film individually in Chapter 4.

REFERENCES

1. Nix WD. Metallurgical Transactions A 1989; 20A: 2217.
2. Spearing SM. Acta Materialia 2000; 48: 179.
3. Tu KN. Journal of Applied Physics 2003; 94: 5451.
4. Zhao J, Wang A, Altermatt P, Green MA. Applied Physics Letters 1995; 66: 3636.
5. Hornbeck LJ. MRS Bulletin 2001; 26: 325.
6. Chopra KL, Paulson PD, Dutta V. Progress in Photovoltaics 2004; 12: 69.
7. Homola J, Yee SS, Gauglitz G. Sensors and Actuators B-Chemical 1999; 54: 3.
8. Love JC, Estroff LA, Kriebel JK, Nuzzo RG, Whitesides GM. Chemical Reviews 2005; 105: 1103.
9. Shin W, Matsumiya M, Izu N, Murayama N. Sensors and Actuators B-Chemical 2003; 93: 304.
10. Venkatraman R, Bravman JC. Journal of Materials Research 1992; 7: 2040.
11. Shu JB, Clyburn B, Mates TE, Baker SP. Journal of Materials Research 2003; 18: 2122.
12. Huang H, Spaepen F. Acta Materialia 2000; 48: 3261.
13. Schwaiger R, Kraft O. Journal of Materials Research 2004; 19: 315.
14. Xiang Y, Vlassak JJ. Acta Materialia 2006; 54: 5449.
15. Thompson CV. Annual Review of Materials Science 2000; 30: 159.
16. Vinci RP, Zielinski EM, Bravman JC. Thin Solid Films 1995; 262: 142.
17. Baker SP, Kretschmann A, Arzt E. Acta Materialia 2001; 49: 2145.
18. Ohring M. Materials Science of Thin Films. San Diego, CA: Academic Press, 2002.

19. Touloukian YS, Ho CY, editors. Thermal Expansion: Non-Metallic Elements and Alloys. New York: IFI/Plenum, 1975.
20. Touloukian YS, Ho CY, editors. Thermal Expansion Metallic Elements and Alloys. New York: IFI/Plenum, 1977.
21. Doerner MF, Nix WD. Crc Critical Reviews in Solid State and Materials Sciences 1988; 14: 225.
22. Thompson CV, Carel R. Journal of the Mechanics and Physics of Solids 1996; 44: 657.
23. Shen Y-L, Suresh S, He MY, Bagchi A, Kienzle O, Ruhle M, Evans AG. Journal of Materials Research 1998; 13: 1928.
24. Weiss D, Gao H, Arzt E. Acta Materialia 2001; 49: 2395.
25. Baker SP, Keller-Flaig R-M, Shu JB. Acta Materialia 2003; 51: 3019.
26. Thompson CV, Carel R. Materials Science and Engineering B-Solid State Materials for Advanced Technology 1995; 32: 211.
27. Thompson CV. Annual Review of Materials Science 1990; 20: 245.
28. Zielinski EM, Vinci RP, Bravman JC. Journal of Applied Physics 1994; 76: 4516.
29. Sonnweber-Ribic P, Gruber P, Dehm G, Arzt E. Acta Materialia 2006; 54: 3863.
30. Hellwege KH, Hellwege AM, editors. Landolt-Bernstein Numerical data and functional relationships in science and technology. New York: Springer-Verlag, 1966.
31. Hellwege KH, Hellwege AM, editors. Landolt-Bernstein Numerical data and functional relationships in science and technology. New York: Springer-Verlag, 1969.
32. Murakami M, Chaudhari P. Thin Solid Films 1977; 46: 109.

33. Murakami M, Kuan TS, Blech IA. Treatise on Materials Science and Technology 1982; 24: 163.
34. Knorr DB, Tracy DP. Materials Chemistry and Physics 1995; 41: 206.
35. Kuschke WM, Kretschmann A, Keller RM, Vinci RP, Kaufmann C, Arzt E. Journal of Materials Research 1998; 13: 2962.
36. Blech IA, Levi AA. Transactions of the ASME. Journal of Applied Mechanics 1981; 48: 442.
37. Loubens A, Fortunier R, Fillit R, Thomas O. Microelectronic Engineering 2003; 70: 455.
38. Sauter AI, Nix WD. IEEE Transactions on Components, Hybrids, and Manufacturing Technology 1992; 15: 594.
39. Fung YC. A first course in continuum mechanics: for physical and biological scientists and engineers. 3rd ed.: Prentice Hall, 1994.
40. Zielinski EM, Vinci RP, Bravman JC. Applied Physics Letters 1995; 67: 1078.
41. Hommel M, Kraft O, Arzt E. Journal of Materials Research 1999; 14: 2373.
42. Hommel M, Kraft O. Acta Materialia 2001; 49: 3935.
43. Gudmundson P, Wikstrom A. Microelectronic Engineering 2002; 60: 17.
44. Wikstrom A, Nygards M. Acta Materialia 2002; 50: 857.
45. Noyan IC. Metallurgical Transactions A - Physical Metallurgy and Materials Science 1983; 14: 249.
46. Weihnacht V, Bruckner W. Acta Materialia 2001; 49: 2365.
47. Pant P, Baker SP. Multiscale Phenomena in Materials - Experiments and Modeling Related to Mechanical Behavior. Symposium, 22-24 April 2003,779. San Francisco, CA, USA: Mater. Res. Soc, 2003. 171.
48. Freund LB. Journal of Applied Mechanics 1987; 54: 553.
49. Matthews JW, Blakeslee AE. Journal of Crystal Growth 1974; 27: 118.

50. People R, Bean JC. Applied Physics Letters 1985; 47: 322.
51. Vandermerwe JH. Journal of Applied Physics 1963; 34: 117.
52. Chaudhari P. Ibm Journal of Research and Development 1969; 13: 197.
53. Sanchez JE, Arzt E. Scripta Metallurgica Et Materialia 1992; 27: 285.
54. Thompson CV. Journal of Materials Research 1993; 8: 237.
55. Xiang Y, Vlassak JJ. Scripta Materialia 2005; 53: 177.

CHAPTER 2

X-ray Strain Measurements in Thin Films

2.1 OVERVIEW

With increased access to high intensity synchrotron sources, x-ray diffraction has become a common method for the characterization of strains in thin films. A wide range of techniques exist, some of which return the effective average stress over the sample [1-3], stresses within subsets of ideally oriented grains in textured samples [4-12], depth profiles of strain with distance from the free surface [13, 14], or submicron strain maps [15-17]. In this section, we will focus on common techniques based on the common $sin^2\psi$ analysis, and review the current state of those methods which return the effective average stress within a film or the average stresses within groups of ideally oriented crystallites (*i.e.* the texture components described in §1).

X-ray strain measurements are based on the ability to use inter-atomic distances within crystalline materials as *in-situ* strain gauges. Strained interplanar distances, *d*, are obtained using Bragg's law

$$n\lambda = 2d\sin\theta, \tag{2.1}$$

where *n* is the reflection order, λ is the wavelength, and θ is the Bragg angle. The effective strained lattice constant, *a*, for a cubic crystal, is then given by $a = d\sqrt{h^2 + k^2 + l^2}$. Strains perpendicular to the measured lattice planes, $\varepsilon_\perp$, are calculated using

$$\varepsilon_\perp = \frac{a - a_0}{a_0} \tag{2.2}$$

where a_0 is the unstrained lattice parameter, which typically is not known to sufficient accuracy or precision from literature values and must be determined directly from experiment.

In terms of the strain tensor for the sampled material, ε_{ij}, the strain $\varepsilon_{\perp}$ along some unit vector n_i (parallel to the scattering vector, $\boldsymbol{q}$) can be written as $\varepsilon_{\perp} = \varepsilon_{ij} n_i n_j$, or in matrix form as

$$\varepsilon_{\perp} = \begin{bmatrix} n_x & n_y & n_z \end{bmatrix} \begin{bmatrix} \varepsilon_{11} & \varepsilon_{12} & \varepsilon_{13} \\ \varepsilon_{21} & \varepsilon_{22} & \varepsilon_{23} \\ \varepsilon_{31} & \varepsilon_{32} & \varepsilon_{33} \end{bmatrix} \begin{bmatrix} n_x \\ n_y \\ n_z \end{bmatrix}. \tag{2.3}$$

The objective of x-ray strain measurements is to measure values of $\varepsilon_{\perp}$ along enough scattering vectors to obtain the full strain tensor. The stress tensor can be calculated using Hooke's law, if the elastic properties of the sample are known.

When possible, large Bragg angle reflections are preferred for strain measurements in order to maximize resolution [18]. This can be demonstrated by differentiation of Bragg's law (Eq. 2.1) at constant wavelength

$$0 = 2\Delta d \sin\theta + 2d \cos\theta \Delta\theta, \tag{2.4}$$

where Δd and $\Delta\theta$ are changes in the interplanar spacing and Bragg angle (in radians), respectively. This can be rearranged into the form

$$\Delta\varepsilon = \Delta d/d = -\cot\theta \Delta\theta, \tag{2.5}$$

where $\Delta\varepsilon$ is the change in strain. Thus, for high angle reflections, small changes in the interplanar spacing, d, will result in larger changes in the Bragg angle, offering improved precision.

Generally, six strain measurements along independent scattering vectors are required to calculate the full strain tensor (Eq. 2.3). If the principal strain coordinate system is known, three strain measurements along the principal axes would suffice.

However, for thin films and surface layers the principal axes often lie within the surface plane, such that these scattering vectors are inaccessible. This is the advantage of the $sin^2\psi$ analysis, which reduces the number of strain measurements required to characterize the strain tensor for surface layers. Many variations in the analysis exist, mainly due to differing approaches in the representation of the sample's elastic properties, as will be demonstrated in §2.3 and §2.4.

2.2 BASICS OF $sin^2\psi$ ANALYSES

The $sin^2\psi$ analysis is a straightforward approach to solving for the strain tensor in Eq. 2.3, when the coordinate system of the principal strains is known. The analysis is based on measuring strains along scattering vectors, $\boldsymbol{q}$, inclined along different directions ψ from the film normal, as illustrated in Figure 2.1. While this analysis can be used for a variety of loading conditions [2, 19-21], let us focus our attention on the case of blanket films $\left(\varepsilon_1 = \varepsilon_2 = \varepsilon_f \neq \varepsilon_3\right)$. For this strain state, the strain, ε_ψ, measured along a scattering vector, $\boldsymbol{q}$, at some angle ψ from the film normal can be shown to vary as

$$\varepsilon_\psi = \left(\varepsilon_f - \varepsilon_3\right)\sin^2\psi + \varepsilon_3 \tag{2.6}$$

(using Eq. 2.3, see Appendix 1). The origin of the name for the analysis now becomes clear. Through measurement of the strain ε_ψ along various angles from the film normal (a minimum of two measurements is required), a straight line can be defined and the strain state can be determined from the slope and intercept. This is an important result, since scattering vectors lying within the film plane are not accessible for a direct measurement of ε_f. Similar results can be obtained within planes defined by the principal axes for any principal strain state in the sample coordinates [2, 6, 22-25], though we will not address these cases here. For cases in which the principal axes of

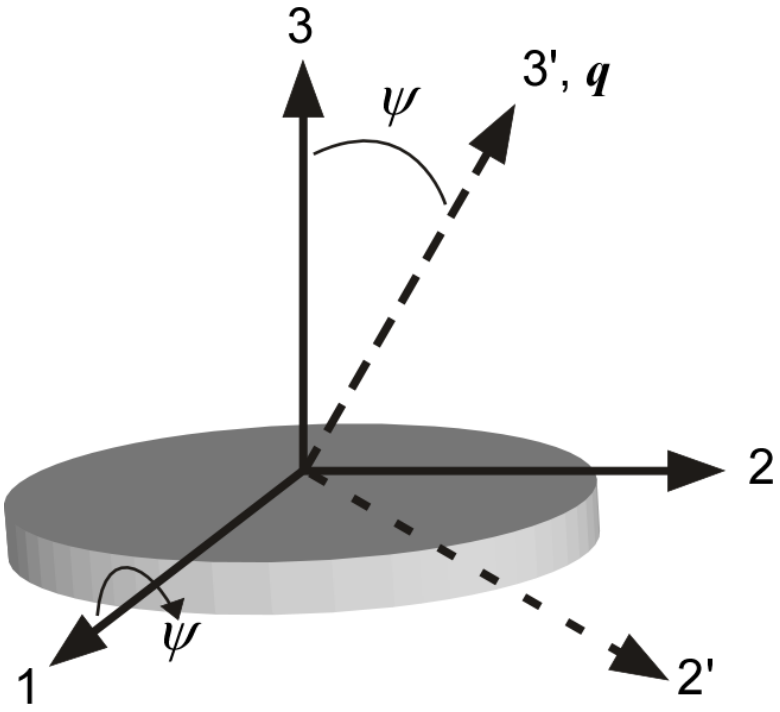

Figure 2.1: Coordinate systems describing the $sin^2\psi$ analysis. Strains are measured along the scattering vector, ***q***, at an angle ψ from the film normal. Since, for equal biaxial strain states in the film plane, rotations along the film normal (**3**) direction do not alter the measured strains, the strains along ***q*** (**3'**) can be described as a rotation around the **1** axis, Eq. 2.3 (see Appendix 1). Strains measured along ***q*** vary linearly with $sin^2\psi$.

the average strains in a sample do not coincide with the sample coordinates, Eq. 2.6 is not representative. In fact, in such cases, nonlinear $sin^2\psi$ behavior may be observed [21].

If the form of the stress tensor is known, Eq. 2.6 can be written to include this information, increasing its utility. For stress states common to thin films $\left(\sigma_1 = \sigma_2 = \sigma_f, \sigma_3 = 0\right)$, the strain in an isotropic film can be written in terms of the film stress

$$\varepsilon_f = \frac{1-\nu}{E}\sigma_f \tag{2.7}$$

$$\varepsilon_3 = \frac{-2\nu}{E}\sigma_f \tag{2.8}$$

where E is the Young modulus and ν is the Poisson ratio. Inserting these values into the $sin^2\psi$ equation (Eq. 2.6), we find

$$\varepsilon_\psi = \sigma_f\left(\frac{1+\nu}{E}\right)\sin^2\psi - 2\sigma_f\frac{\nu}{E}. \tag{2.9}$$

Historically, the coefficients containing elastic constant have been called "X-ray Elastic Constants", or XECs; $S_1 = -\nu/E$ and $1/2\,S_2 = (1+\nu)/E$, which relate the average stresses to measured sample strains according to [21]

$$\varepsilon_{ij} = \frac{1}{2}S_2\sigma_{ij} - \delta_{ij}S_1\left(\sigma_{11}+\sigma_{22}+\sigma_{33}\right). \tag{2.10}$$

While the term XEC is widely used, it is an admitted misnomer, as for anisotropic materials these "constants" are typically a function of the sample and measurement details. Different approaches to represent the elastic properties of anisotropic and textured samples will be addressed in §2.3 and §2.4.

Since diffraction provides a measure of interplanar distances, and not strains, equations similar to Eq. 2.9 used in these measurements are commonly written in

terms of lattice parameters using Eq. 2.2, since these can be obtained from Bragg's law,

$$a_{\psi} = a_0\sigma_f\left(\frac{1+\nu}{E}\right)\sin^2\psi - a_0\left(\sigma_f\frac{2\nu}{E}+1\right), \tag{2.11}$$

where a_{ψ} is the lattice parameter measured along a direction at an angle ψ from the film normal. The line described by Eq. 2.11 can now be defined experimentally, from which the values for the slope and intercept can be obtained providing a system of two equations in terms of a_0 and σ_f. Thus, both the stress and unstrained lattice parameter can be calculated directly from this analysis. However, if the wrong form of the stress tensor is assumed to formulate Eq. 2.9 significant artifacts can exist in the results [19, 20] (for example, see Appendix 2).

Traditionally, the line defined by Eq. 2.11 is experimentally determined by measuring the lattice spacings corresponding to a single *hkl* reflection over a wide range of ψ. However, for anisotropic and/or textured samples (as are most thin metal films) the strain measured along a single *hkl* reflection often exhibits a nonlinear or *hkl*-dependent $sin^2\psi$ behavior, since the different subsets of illuminated grains at different angles, ψ, are under subjected to varying states of strain. There is a large body of literature addressing this limitation following two approaches: (1) Advancing the traditional approach of using XECs to characterize the average stress within the sample [2], or (2) Utilizing highly oriented microstructures to define $sin^2\psi$ lines using specifically oriented reflections, in order to separately characterize different subsets of ideally oriented grains—known as the *Crystallite Group Method* [4, 5].

2.3 X-RAY ELASTIC CONSTANTS

The traditional approach for $sin^2\psi$ analyses of thin films or bulk surfaces layers is based on measuring lattice spacings for a single *hkl* reflection over a range of

ψ [2, 20, 21]. In this approach, the experimental strains are related to the average stresses in the sample by representing the elastic properties of the material using "X-ray Elastic Constants" (XECs), or more recently "X-ray Stress Factors" (XSFs) to account for crystal anisotropy and texture. This section will briefly overview this approach.

For randomly oriented, polycrystalline samples of anisotropic materials, the strain along a given sample direction within any grain will be a function of the grain's crystalline orientation relative to the loading axis, as well as the orientation if its neighbors. Therefore, the strain measured along some sample direction, ψ, will depend on the subset of grains sampled, which is dependent on the *hkl* reflection used. As a result, in the traditional single reflection $sin^2\psi$ method, the slope and intercept of the $sin^2\psi$ line depend on the *hkl* reflection used. In other terms, XECs are *hkl*-dependent. However, it is difficult to know *a priori* what strain will exist along a certain sample direction in a grain with a specific orientation. This depends on the type of grain interactions prevalent in the sample, which is a function of the loading state and grain morphology. Thus, for samples of anisotropic materials, the *hkl*-dependent XECs must somehow be determined.

The most straightforward approach to determine the XECs for a given sample is direct measurement. This is done performing $sin^2\psi$ analyses on samples subjected to known loading states. Originally, this approach was developed for bulk materials under uniaxial tension or three point bending [20, 21]. Once XECs are determined such that that the x-ray measurements agree with the known applied loads, the XECs can be used to characterize residual stresses within samples of interest. These values for various materials have been tabulated and treated as constants for widespread use [20], though they are truly function of the specific microstructures examined.

Of course, independent characterization of XECs for every sample of interest is not always practical or feasible. Thus, it is common to approximate XECs for different materials in terms of effective grain interaction models (*i.e.* Reuss and Voigt being the most common), since by utilizing interaction models the strain along different sample directions in grains with different orientations can be approximated [20, 21].

For example, in an assumed Reuss grain interaction model, all crystallites have the same stress state. Thus, due to elastic anisotropy, crystallites with different orientations are subjected to different strain states. To relate the different measured strains with the same stress states, elastic constants have been approximated by the *directional modulus*, E^{hkl}, which is the Young's modulus of a single crystal uniaxially loaded along the <*hkl*> direction, and the contraction ratio, ν^{hkl}, which is the average Poisson contraction for a load applied along <*hkl*> [21]. Essentially, the Reuss average approach treats samples as isotropic mediums with these *hkl*-specific elastic properties.

For a Voigt grain interaction model, grains of all orientations are subjected to an identical strain tensor, such that XECs have no dependence on the orientation of diffracting crystallites, *i.e.* no *hkl* dependence. The elastic constants used for Voigt interaction XECs are the average of the single crystal compliance constants for all crystal orientations [21] (this is the definition of the Voigt average). Of course, real polycrystals have grain interactions that typically fall between the Voigt and Reuss limits, and as such, XEC calculations have used other interaction types such as Neerfeld-Hill [21] to accurately capture behaviors. While XECs may be approximated from assumed grain interaction types, difficulties arise in determining a proper interaction model. Thus, an independent measurement of XECs (*e.g.* during external loading) may be required to confirm results.

XECs are primarily for randomly oriented samples that exhibit linear $sin^2\psi$ behaviors. However, for textured specimens with macroscopically anisotropic elastic constants (the vast majority of thin films), the strain measured along a single *hkl* reflection at various angles ψ typically no longer varies linearly with $sin^2\psi$. To address this additional complexity, building on the approach used to define XECs, so called "X-ray Stress Factors" or XSFs were introduced [3, 21]. These XSFs are *hkl*- and direction-dependent representations of elastic properties which relate the average measured strain along a direction at an angle ψ from the film normal, ε_ψ, to the average stress tensor in the sample coordinates, σ_{ij},

$$\varepsilon_\psi = F_{ij}(hkl,\psi)\sigma_{ij} \tag{2.12}$$

where $F_{ij}(hkl,\psi)$ represent the XSFs.

The average strain measured along a scattering vector at an angle of ψ from the film normal can be written in terms of the strain within grains properly oriented for diffraction (*hkl* plane unit normal directions, $\vec{s}$, parallel to $\boldsymbol{q}$), weighted by the orientation distribution function, $f(\Omega)$, or fraction of grains with orientation Ω,

$$\varepsilon_\psi = \frac{\int_0^{2\pi} \varepsilon_{ij}(\vec{s}=q,\eta) n_i n_j f(\vec{s}=q,\eta) d\eta}{\int_0^{2\pi} f(\vec{s}=q,\eta) d\eta}, \tag{2.13}$$

where η represents a rotation around the *hkl* plane normal vector [21]. By comparing Eq. 2.12 and Eq. 2.13, and differentiating with respect to the stress tensor, an equation can be given that represents the X-ray Stress Factors,

$$F_{ij}(hkl,\psi) = \frac{\int_0^{2\pi} \frac{\partial \varepsilon_{ij}(\vec{s}=q,\eta)}{\partial \sigma_{kl}} n_i n_j f(\vec{s}=q,\eta) d\eta}{\int_0^{2\pi} f(\vec{s}=q,\eta) d\eta}. \tag{2.14}$$

In this equation, the relation between strain tensor in a grain properly oriented for diffraction and the average stress tensor in the sample must be defined in terms of a model for elastic grain interactions, similar to the approach with XECs. Straightforward details of the calculations for $F_{ij}(hkl,\psi)$ are rare in the literature, and are beyond the scope of this overview. However, general properties of XSFs are important to note.

The same limitation exists for defining XSFs in terms of effective grain interaction models that exists for XECs—the prevalent grain interaction type within a sample is typically unknown. Additionally, for highly textured samples that are macroscopically anisotropic, different grain interactions may occur along different sample directions. This behavior is not captured in traditional grain interaction models, which assume similar behaviors in all sample directions. Thus, in order to address directional grain interactions for XSFs, so called *direction dependent grain interaction models* [1, 26, 27] were introduced, which consider isostrain behavior in-plane, and isostress behavior out-of-plane, or vice versa, and are referred to as Vook-Witt and inverse Vook-Witt grain interaction models, respectively. Of course, in real samples grain interactions are rarely described by extreme isostrain or isostress models, and as such, averages are commonly used. For instance, Welzel *et al.* modeled non-linear $sin^2\psi$ behaviors for various *hkl* reflections in thin films using best fits to the data using linear combinations of XSFs from Voigt, Reuss, Vook-Witt, and Inverse Vook-Witt grain interaction models [1, 26].

Though much work has gone into describing grain interactions for the calculation of XSFs, the direct measurement approach is also possible. For instance, x-ray strain measurements for single *hkl* reflections over ranges of ψ have been performed on thin films in tandem with substrate curvature measurements to provide

the macroscopic stress state [28], allowing residual stress characterization of similar films on thick substrates.

In the end, x-ray strain measurements using XECs and XSFs have limited utility for *in-situ* characterization of stresses and deformation behaviors in thin films for several reasons. Firstly, since these approaches return the average stress over the film, other characterization techniques such as substrate curvature [29] can return quick and accurate values without the uncertainty and complexity of XECs and XSFs. Secondly, accurate descriptions of the average grain interactions in a sample, to accurately describe XSFs, require measurement of strains along numerous *hkl* reflections analyses over wide ranges of ψ. This is time consuming, making these measurements ill-suited for *in-situ* behaviors. Lastly, grain interaction models are always an approximation of the average behavior in the film. If orientation-dependent strains are of interest for films with complex texture, an approach described by Miller *et al.* [30, 31] may be more appropriate, and accurate. In short, Miller *et al.* demonstrated for bulk samples that with knowledge of the orientation distribution function, and measurements of the average strains for multiple *hkl* reflections over a wide range of sample orientations, a Lattice Strain Distribution Function (LSDF) can be determined—a description of the average strain tensor as a function of grain orientation.

For highly oriented samples, in which the vast majority of the sample volume is found in a few specific grain orientations, a more straightforward approach can be used to characterize the strain states, as described in §2.4.

2.4 THE CRYSTALLITE GROUP METHOD

The difficulty in characterization of samples without, or with weak, preferred orientations is that the exact orientation of grains sampled for some *hkl* reflection at

some angle ψ from the film normal is not known, requiring optimizations and approximations of the elastic properties to determine stresses, as described above. This is not the case for strongly textured samples, for which scattering vectors can be unambiguously attributed to grains with a specific orientation. If sufficient scattering vectors can be attributed to a certain texture component, the average strain tensor within that grain orientation can be obtained (Eq. 2.3) and single crystal elastic constants can be used to calculate stresses. This approach is known as the Crystallite Group Method (CGM).

An early variation of the Crystallite Group Method for textured metal films was presented by Murakami for the case of a highly (111) textured Pb thin film [32, 33]. Commonly, the development of the Crystallite Group Method is attributed to later publications by Willemse & Naughton who used x-ray diffraction to characterize strains within ideally oriented texture components within cold drawn steel wire [4] or Hauk *et al.* who reported the strains within ideal texture components of rolled steels [9, 10]. For thin films with (111) and (100) fiber textures, *i.e.* FCC metal films, an excellent overview of the Crystallite Group Method was presented by Clemens & Bain [5]. This approach has been employed in numerous investigations to measure strains in thin films with single [7, 8, 23, 32-37] or mixed (111)/(100) [6, 11, 12, 38] fiber textures.

The basic basis of the CGM is that for highly oriented samples, scattering vectors can be attributed to grains with specific orientations. If enough scattering vectors can be found, the CGM is able to return the average strains within subsets of ideally oriented grains in a sample that exhibit similar behaviors. Texture selection is demonstrated in Figure 2.2 for a mixed fiber textured FCC metal film with (111) and (100) crystal orientations normal to the film plane. For the (111) texture, the diffraction conditions can be set to measure a {111} reflection with a scattering vector

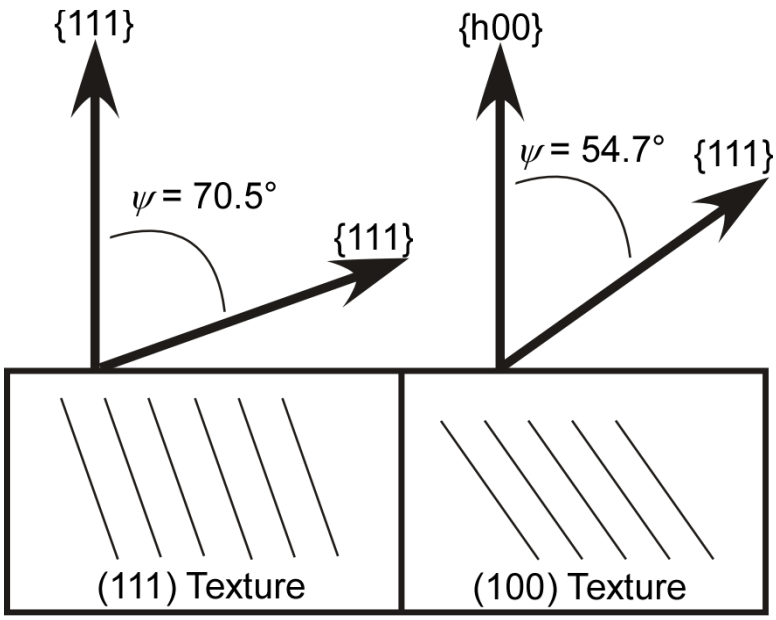

Figure 2.2: Orientation selection in films with mixed texture. For example, as defined by the crystal geometry, in (111) textured grains, a {111} type reflection can be found at an angle of $\psi = 70.5°$ from the film normal, as well as normal to the film plane ($\psi = 0°$). In the (100) orientation, {111} type reflections can be found at an angle of $\psi = 54.7°$ from the film normal. Normal to the film plane in the (100) orientation ($\psi = 0°$), only {h00} type reflections can be measured. For other *hkl* reflections, crystal geometry can be used to attribute specific scattering vectors to one of the two texture components.

normal to the film plane. Additionally, in the (111) texture component, the scattering conditions may be set to measure a {111}-type reflection at an angle $\psi = 70.5°$ from the film normal, as defined by the crystal geometry. At no other angle ψ can a {111}-type reflection belonging to the (111) texture component be found, and due to the fiber texture, there is no dependence on in-plane orientation. In the other texture component, (100), the scattering conditions can be set to measure a {111}-type reflection belonging to (100) grains at an angle of $\psi = 54.7°$ as defined by the crystal geometry. For a scattering vector normal to the film plane in the (100) texture component, the only lattice spacing that can be measured is for {h00}-type reflections. Similar crystal geometry arguments can be used to calculate the angles ψ for the orientations of other *hkl* reflections in either the (111) or (100) texture components. It is important to ensure scattering vectors can only be attributed to a single crystallite group. Since the grain orientations are well known, single crystal elastic constants can be used to calculate stresses from the measured strains.

Since the biaxial moduli of the (111) and (100) orientations are transversely isostropic, the strain tensor within each of these orientations is of the form of Eq. 1.3. Thus, there is no in-plane orientation dependence of measurements, and strains within each texture component vary according to Eq. 2.6. Following the outline of Clemens & Bain [5], the general steps to derive a useful form of $sin^2\psi$ equations incorporating the stress states within each crystallite group and the single crystal elastic constants (similar to Eq. 2.9 for the isotropic case) are as follows:

1.) Assume the form of the stress (and strain) tensors in sample coordinates for the crystallite group
2.) Rotate the stress tensor from sample coordinates to crystal coordinates

3.) Use Hooke's law to calculate the strains in crystal coordinates from the assumed stress state using the single crystal compliance constants.

4.) Rotate the equations for the strains back from crystal coordinates to sample coordinates.

5.) Calculate the strain along a scattering vector, $\boldsymbol{q}$, at an angle ψ from the film normal (*i.e.* Eq. 2.3, Appendix 1)

6.) Use Eq. 2.2 to write the strains in terms of the measured and unstrained lattice parameter.

For the (111) and (100) texture components of an FCC metal film, each under an equal biaxial stress state, this procedure yields

$$\varepsilon_{\psi}^{111} = \frac{a_{\psi}^{111} - a_0}{a_0} = \left(\frac{S_{44}}{2}\right)\left(\sigma_f^{111}\right)\sin^2\psi + \frac{2S_{11} + 4S_{12} - S_{44}}{3}\sigma_f^{111}\,, \qquad (2.15)$$

and

$$\varepsilon_{\psi}^{100} = \frac{a_{\psi}^{100} - a_0}{a_0} = \left(S_{11} - S_{12}\right)\left(\sigma_f^{100}\right)\sin^2\psi + 2S_{12}\sigma_f^{100}\,, \qquad (2.16)$$

where ε_{ψ}^{hkl} are the strains along a vector at an angle ψ, a_{ψ}^{hkl} are the measured lattice parameters, σ_f^{hkl} are the in-plane stresses within each texture component, and S_{ij} are the single crystal compliance constants. Experimentally, these lines can be quickly defined by measuring a_{ψ}^{hkl} along a minimum of two angles ψ, making this analysis convenient for time sensitive *in-situ* strain characterizations. Since the experimental $sin^2\psi$ line provides values for the slope and intercept, both the unknown unstrained lattice parameter and film stress can be solved for within each texture component independently. However, if the incorrect form of the stress tensor is assumed (Step 1 in the derivation of these equations) significant artifacts can arise in the analysis, as is discussed in Chapter 3 (also demonstrated in Appendix 2).

A simplification to this analysis commonly made for an assumed equal biaxial stress states (Equations 2.15-2.16), if the unstrained lattice parameter is known independently or can be approximated, is to only measure strain perpendicular to the film plane, ε_3, in order to solve for the stresses [12, 32, 33, 38]. This approach speeds measurements by taking advantage of the strong intensity of reflections along the fiber axis and by not requiring a second off-axis peak. However, this approach is susceptible to measurement artifacts if an incorrect stress state is assumed [39], or if the film composition changes, altering a_0 [40], as neither of these errors can be identified with this simplified analysis. However, by including the off-axis reflection to solve for both the stress and lattice parameter, these artifacts could be observed in the data.

For non equal-biaxial strain states, such as those found in film under uniaxial tension [6, 8, 24] or in patterned lines [22, 23, 25], variations of the Crystallite Group Method have been proposed to characterize the average stresses. However, when strain states are unequal in the film plane, the transverse isostropy of the (111) and (100) texture components are not utilized, and the in-plane orientations of grains within the (111) and (100) fiber textures may influence mechanical behaviors—due to elastic anisotropy or different orientations of slip systems relative to the loading axis. Thus, the (111) and (100) orientations may not represent self consistent crystallite groups, and these investigations [6, 8, 22-25] have actually reported strains within subsets of the (111) or (100) textured components having in-plane orientations properly aligned for diffraction.

Despite the difficulty of defining representative crystallite groups for non-equal biaxial strain states in fiber textured samples, the ability to rapidly characterize the average strains within groups of ideally oriented crystallites makes this approach useful for time sensitive measurements. In mixed texture films, the CGM can provide

information on the distribution of stress in a film, and potentially the locations of peak stresses that may drive failure mechanisms. However, any randomly oriented grains will not be represented in the measurements.

2.5 SUMMARY

Many variations of x-ray strain analyses based on the $sin^2\psi$ method have been proposed for the characterization of thin metal films. In the conventional approach, a single *hkl* reflection is measured over a wide range of sample orientations, and the measurement- and microstructure-dependent behaviors are related to the stress state through approximations and optimizations of the sample's elastic properties, XECs or XSFs. While this approach (or an approach similar to ref.'s [30, 31]) is necessary when the exact orientations of diffracting grains are unknown, for highly oriented films, the Crystallite Group Method can quickly provide the average strain states within representative groups of like-oriented crystals. Since the orientations of the diffracting crystallites are well known, established single crystal elastic constants can be used to calculate the stresses, eliminating the ambiguity found in the XEC and XSF approach. Additionally, the CGM can provide information of the partitioning of stresses across the different texture components of a mixed texture microstructure. Throughout this thesis, the CGM will be used to characterize strain states within textured thin films.

REFERENCES

1. Welzel U, Leoni M, Mittemeijer EJ. Philosophical Magazine 2003; 83: 603.
2. Welzel U, Ligot J, Lamparter P, Vermeulen AC, Mittemeijer EJ. Journal of Applied Crystallography 2005; 38: 1.
3. Welzel U, Mittemeijer EJ. Journal of Applied Physics 2003; 93: 9001.
4. Willemse PF, Naughton BP, Verbraak CA. Materials Science and Engineering 1982; 56: 25.
5. Clemens BM, Bain JA. MRS Bulletin 1992; 17: 46.
6. Hommel M, Kraft O. Acta Materialia 2001; 49: 3935.
7. Gruber PA, Bohm J, Onuseit F, Wanner A, Spolenak R, Arzt E. Acta Materialia 2007; 56: 2318.
8. Bohm J, Gruber P, Spolenak R, Stierle A, Wanner A, Arzt E. Review of Scientific Instruments 2004; 75: 1110.
9. Hauk V, Krug WK, Oudelhoven RWM, Pintschovius L. Zeitschrift fur Metallkunde 1988; 79: 159.
10. Hauk V, Vaessen G. Zeitschrift fur Metallkunde 1985; 76: 102.
11. Baker SP, Kretschmann A, Arzt E. Acta Materialia 2001; 49: 2145.
12. Vinci RP, Zielinski EM, Bravman JC. Thin Solid Films 1995; 262: 142.
13. Dehm G, Inkson BJ, Balk TJ, Wagner T, Arzt E. Dislocations and Deformation Mechanisms in Thin Films and Small Structures Symposium, 17-19 April 2001. San Franciso, CA, USA: Mater. Res. Soc, 2001. 2.
14. Brennan S, Munkholm A, Leung OS, Nix WD. Physica B 2000; 283: 125.
15. Phillips MA, Spolenak R, Tamura N, Brown WL, MacDowell AA, Celestre RS, Padmore HA, Batterman BW, Arzt E, Patel JR. Microelectronic Engineering 2004; 75: 117.

16. Spolenak R, Brown WL, Tamura N, MacDowell AA, Celestre RS, Padmore HA, Valek B, Bravman JC, Marieb T, Fujimoto H, Batterman BW, Patel JR. Physical Review Letters 2003; 90.
17. Tamura N, MacDowell AA, Spolenak R, Valek BC, Bravman JC, Brown WL, Celestre RS, Padmore HA, Batterman BW, Patel JR. Journal of Synchrotron Radiation 2003; 10: 137.
18. Megaw HD, Stokes AR. Journal of the Institute of Metals 1945; 71: 279.
19. Noyan IC. Metallurgical Transactions A - Physical Metallurgy and Materials Science 1983; 14: 249.
20. Noyan IC, Cohen JB. Residual Stress. New York: Springer-Verlag, 1987.
21. Hauk V. Structural and Residual Stress Analysis by Nondestructive Methods. Amsterdam: Elsevier, 1997.
22. Besser PR, Brennan S, Bravman JC. Journal of Materials Research 1994; 9: 13.
23. Flinn PA, Chiang C. Journal of Applied Physics 1990; 67: 2927.
24. Hommel M, Kraft O, Arzt E. Journal of Materials Research 1999; 14: 2373.
25. Besser PR, Marieb TN, Lee J, Flinn PA, Bravman JC. Journal of Materials Research 1996; 11: 184.
26. Welzel U, Freour S, Mittemeijer EJ. Philosophical Magazine 2005; 85: 2391.
27. Welzel U, Mittemeijer EJ. Jom 2007; 59: 66.
28. Martinschitz KJ, Eiper E, Massl S, Kostenbauer H, Daniel R, Fontalvo G, Mitterer C, Keckes J. Journal of Applied Crystallography 2006; 39: 777.
29. Nix WD. Metallurgical Transactions A 1989; 20A: 2217.
30. Miller MP, Bernier JV, Park JS, Kazimirov A. Review of Scientific Instruments 2005; 76.
31. Bernier JV, Miller MP. Journal of Applied Crystallography 2006; 39: 358.

32. Murakami M, Chaudhari P. Thin Solid Films 1977; 46: 109.

33. Murakami M. Acta Metallurgica 1978; 26: 175.

34. Korhonen MA, Paszkiet CA. Scripta Metallurgica 1989; 23: 1449.

35. Leung OS, Munkholm A, Brennan S, Nix WD. Journal of Applied Physics 2000; 88: 1389.

36. Zoo Y, Alford TL. Journal of Applied Physics 2007; 101: 033505.

37. Gruber PA, Olliges S, Arzt E, Spolenak R. Journal of Materials Research 2008; 23: 2406.

38. Zielinski EM, Vinci RP, Bravman JC. Applied Physics Letters 1995; 67: 1078.

39. Vodnick AM, Nowak DE, Labat S, Thomas O, Baker SP. to be submitted 2009.

40. Vodnick AM, Lawrence MD, Little B, Warden D, Shefford BP. Mater. Res. Soc. Symp. Proc.,1027E. Boston, MA: Materials Research Society, 2008. 1027.D01.01.

CHAPTER 3

Out-of-plane Stresses Arising from Grain Interactions in Textured Thin Films

Aaron M. Vodnick[1] , David E. Nowak[1], Stephane Labat[2], Olivier Thomas[2] and Shefford P. Baker[1]

[1]*Cornell University, Department of Materials Science and Engineering, Bard Hall, Ithaca, NY 14853*

[2]*IM2NP, UMR CNRS 6242, Université Paul Cézanne Aix-Marseille III, 13397 Marseille Cedex 20, France*

3.1 ABSTRACT

FCC thin films often have mixed (111)/(100) fiber texture. These orientations can have very different in-plane stiffnesses, leading to the possibility of significant stress inhomogeneities. Previous x-ray studies appeared to confirm this, reporting isostrain conditions with much higher stresses in (111)- than (100)-oriented grains. In those studies, the stress in the film normal direction was assumed to be zero everywhere, but Poisson effects suggest that out-of-plane stresses may be significant. Here, an x-ray data analysis that allows for out-of-plane stresses is presented and applied to x-ray data taken from a Cu film. The in-plane stress is shown to be homogeneous, and significant out-of plane stresses arise. This analysis is shown to be more accurate and more consistent with the microstructure than previous methods. Consideration of inhomogeneous triaxial stress states is seen to be critical to understanding mechanical behavior of films with mixed fiber texture. Models for yielding and texture development are discussed.

3.2 INTRODUCTION

Thin face-centered-cubic (FCC) metal films on substrates are surprisingly common. For example, Al and Cu films serve as interconnect materials in micro-electronic and -mechanical devices [1-3], Al, Au, and Ag films are used as optical reflectors [4], Au is used as a substrate for creating self assembled monolayers [5], and Pt films are used as catalysts [6]. Like all films, FCC metal films are subjected to extremely high stresses which can lead to failure due to fracture, deadhesion, void or hillock formation, or elastic distortion [1, 3]. As a result, there has been intense interest in their mechanical behavior [1, 3, 7-14].

In most studies of FCC metal films, film stresses were determined from measurements of the curvature induced in the substrate by interaction with the film during thermal cycling (e.g. [1, 7, 14, 15]. Such measurements can be quite accurate, but give only the average stress interaction with the substrate. No information about the stress distribution within the film is obtained. Accordingly, the stress state is typically assumed to be equal-biaxial, given by

$$\sigma_{ij} = \begin{bmatrix} \sigma_f & 0 & 0 \\ 0 & \sigma_f & 0 \\ 0 & 0 & 0 \end{bmatrix}, \tag{3.1}$$

and the strain state triaxial, given by

$$\varepsilon_{ij} = \begin{bmatrix} \varepsilon_f & 0 & 0 \\ 0 & \varepsilon_f & 0 \\ 0 & 0 & \varepsilon_3 \end{bmatrix}. \tag{3.2}$$

This corresponds to the strain state in a homogeneous isotropic material subjected to an equal-biaxial stress in the film plane. The relevant elastic modulus is the "biaxial modulus" $Y = \sigma_f/\varepsilon_f = E/(1-\nu)$ with E the Young modulus and ν the Poisson ratio.

But of course most crystalline films are not isotropic—with significant repercussions for both microstructure and mechanical behavior. For example, FCC films tend to have (111) or (100) planes parallel to the substrate [16]. These orientations have biaxial moduli which are transversely isotropic about the film normal so that a uniform strain applied in the plane of the film results in a stress that is also invariant in the film plane. Thus, in this case, both (111) or (100) single-crystal films and polycrystalline cubic films with perfect (111) or (100) fiber texture have simple uniform biaxial stress states as given in Eq. 3.1. The corresponding biaxial moduli can be shown to be

$$Y^{111} = \frac{\sigma_f}{\varepsilon_f} = \frac{6C_{44}\left(C_{11} + 2C_{12}\right)}{C_{11} + 2C_{12} + 4C_{44}} \tag{3.3}$$

and

$$Y^{100} = \frac{\sigma_f}{\varepsilon_f} = C_{11} + C_{12} - \frac{2C_{12}^2}{C_{11}} \ , \tag{3.4}$$

where the C_{ij}'s are the single crystal elastic constants. Y^{111} and Y^{100} can be quite different. For example, Y^{111}/Y^{100} = 1.15, 2.25, 2.3, and 3.0 for Al, Cu, Ag, and Pb, respectively.

Interface energies are also anisotropic, and it is straightforward to construct a thermodynamic model in which FCC films adopt either a (100) orientation when thick since this orientation minimizes strain energy or a (111) orientation when thin since this orientation minimizes interface energy [16]. However, the microstructures of real FCC films are not always so simple. Films with both (111) and (100) fiber texture components are also common [8, 12, 13, 17-19]. Since $Y^{111} > Y^{100}$, one might expect a uniform applied strain (*e.g.* due to differential thermal expansion between film and substrate), to produce higher stresses in (111) grains than in (100) grains.

The prospect of inherently inhomogeneous stresses in a mixed texture film frames stress-driven processes in a new light. Since failures occur at locations of peak

stress, it is important to determine maximum stresses, not just the average. Stress gradients, which affect diffusive processes, must also be considered. Finally, strain transfer between texture components will affect the stress states and strain energies in the texture components.

In principle, as long as enough diffraction peaks can be found that can be attributed to only one texture component, x-ray diffraction can be used to unambiguously determine the average stress states in the (111) and (100) texture components in an FCC film having only those components. Several attempts have been made in recent years to do just that. Vinci, Zielinski, and Bravman [8] (VZB); Baker, Kretchmann, and Arzt [12] (BKA); and Hommel and Kraft [13] (H&K) all used x-ray methods to characterize the stress states in the (111) and (100) texture components in thin Cu films simultaneously during testing. VZB and BKA measured strains in Cu films on Si substrates during thermal cycling, while H&K studied strain imposed isothermally during tensile tests of Cu films on thick polyimide substrates. In all three studies, the in-plane stresses in (111) oriented grains were found to be much larger than those in (100) oriented grains, apparently confirming expectations raised by Equations 3.3 and 3.4. In fact, BKA found $\sigma_f^{111} / \sigma_f^{100} \approx 2.3$, the ratio of the biaxial moduli during cooling in their thermomechanical measurements, and H&K found $\sigma_f^{111} / \sigma_f^{100} \approx 2$, the ratio of the Young moduli, in their tensile tests, suggesting that isostrain conditions prevailed in both cases.

These perfect isostrain results are surprising for two reasons. First, the lack of strain transfer between texture components suggests that texture boundaries are few and far between, yet the mean grain sizes reported in all three studies were near the film thickness. As a possible explanation, BKA suggested that, if grains in each fiber texture component clump together, the spacing between texture boundaries could be much larger than the spacing between grain boundaries. Second, since isostrain

conditions are found even during plastic deformation, this implies that plastic strain must also be the same in both texture components. While not precluded, it is not evident why strain hardening should exhibit this behavior.

We note that, while the x-ray analyses in these studies were different, all used the assumption that the out-of-plane stress is zero, *i.e.* $\sigma_3 = 0$ as in Eq. 3.1, everywhere in the film. This assumption is common in x-ray stress analyses and is defended based on the requirement that the stress at the free surface be zero [8, 12, 13, 20-25]. If the film is homogenous, then the traction-free surface in fact ensures that out of plane stress in the interior of the film will be zero. However, if the film is inhomogenous, this assumption breaks down. In the present case, different out-of-plane Poisson strains can lead to out of plane stresses along texture boundaries due to their mutual constraint. This problem has been described for surface layers with hard and soft regions [26]. We here describe it for anisotropic films with mixed texture.

Clearly, if out-of-plane stresses are significant, an analysis that assumes they are zero will be in error. In the present paper, we present an x-ray stress analysis that accounts for out-of-plane stresses in films having mixed texture and apply it to x-ray data obtained from Cu films in a manner similar to the methods reported by VZB, BKA, and H&K. We show that many of the conclusions reached in these earlier works are incorrect, and that the data are much more self-consistent if out-of-plane stresses are taken into account. Finally, we discuss a few key models for stress-driven phenomena in thin films that should be reconsidered in light of more realistic triaxial stress states.

3.3 STRESS STATES IN THIN FILMS

We begin with a conceptual discussion of the stress states that might be expected based on the microstructure of an FCC film with mixed (111)/(100) texture.

3.3.1 In-plane stresses

The average in-plane stress distribution in the texture components can range from isostress ($\sigma_f^{100} = \sigma_f^{111}$) to isostrain ($\varepsilon_f^{100} = \varepsilon_f^{111}$), depending on the microstructure, as the following thought experiment demonstrates: Consider an elastically-deforming film with alternating (111) and (100) regions as shown in Figure 3.1a. If the film could be subjected to a uniform substrate interaction strain (dashed lines in Fig. 3.1b), the stress in the (111) regions would be higher than that in the (100) regions following Eq.'s 3.3 and 3.4. However, the stress field must be continuous in the direction perpendicular to the texture boundaries, necessitating transfer of strain from the stiffer (111) texture components to the more compliant (100) texture components. (Note that due to the transverse isotropy of the biaxial moduli in these texture components, grain boundaries between two grains with (111) or (100) orientations require no strain transfer. Only boundaries between (111)- and (100)- oriented grains, which we refer to as texture boundaries, are of interest here). This strain transfer could be accomplished by elastic bowing of the texture boundaries as shown in Fig. 3.1b (solid lines). Since this strain transfer is expected to occur within a few film thicknesses of the texture boundary [27, 28], the average stress state in either texture component depends on the ratio of texture boundary spacing d_{tb} to film thickness t_f [12]. As d_{tb}/t_f becomes small, as in Fig. 3.1c, the in-plane strain transfer becomes complete such that $\sigma_f^{100} = \sigma_f^{111}$ (isostress) through most of the film thickness. As d_{tb}/t_f becomes very large, as in Fig. 3.1d, the in-plane strain transfer is limited to regions near texture boundaries so that regions away from texture boundaries support the applied strain. In this case, the average in-plane strains in the texture components approach $\varepsilon_f^{100} = \varepsilon_f^{111}$ (isostrain) and $\sigma_f^{111} \big/ \sigma_f^{100}$ approaches $Y^{111} \big/ Y^{100}$.

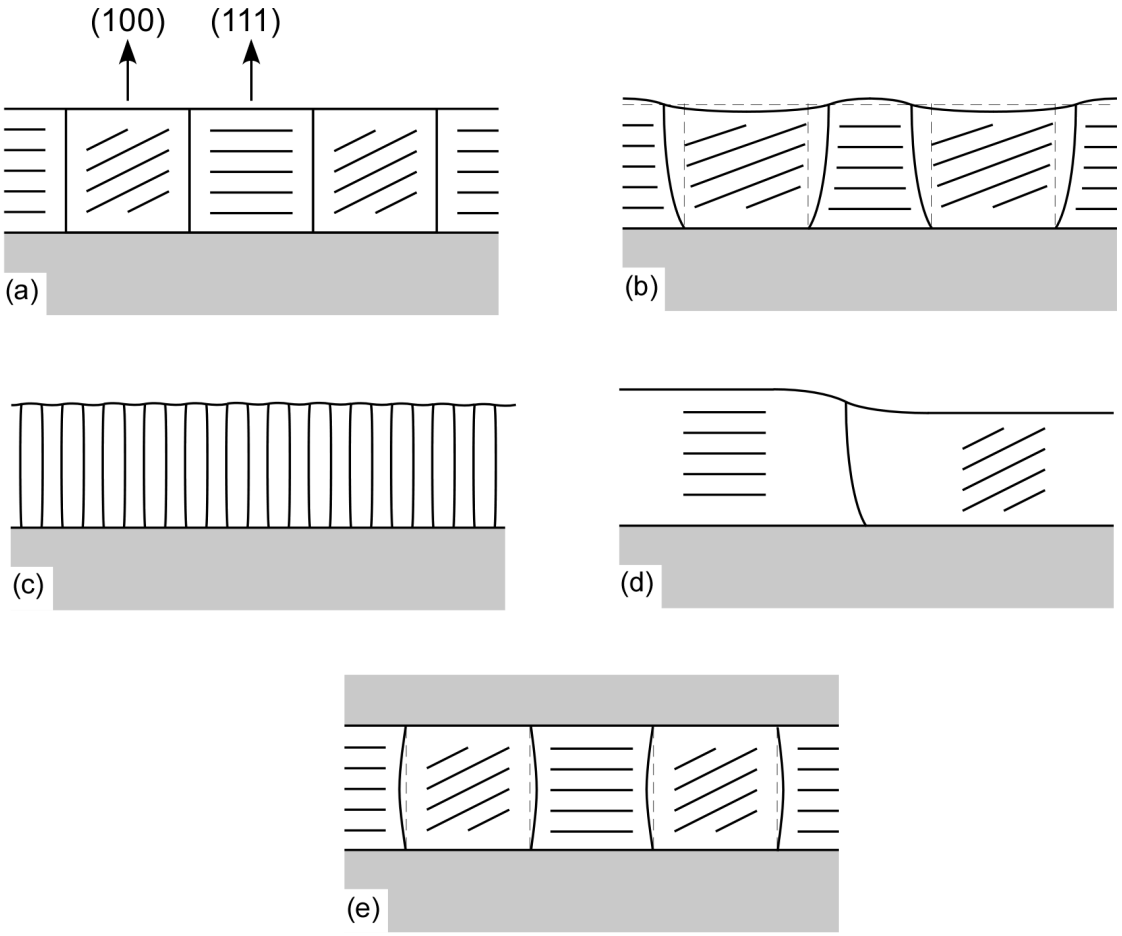

Figure 3.1: (a) Schematic illustrating a film with mixed (111) and (100) fiber textures. (b) Strain redistribution due to a stress interaction in a strained film. Texture boundaries bow towards (111) and away from (100) orientations to maintain stress continuity across the boundary. Out-of plane strains are different in the two orientations due to different Poisson ratios. (c) for small width/height ratios, boundary bowing leads to isostress in-plane, while constraint on relative strains leads to isotrain out-of-plane. (d) For large width/height ratios, strain transfer occurs only near texture boundaries such that the average in plane strain approaches the applied strain and the stress in the out of plane direction approaches zero. (3) A rigid passivation enforces isostrain conditions in the out of plane direction regardless of texture boundary spacing.

3.3.2 Out-of-plane stresses

Just as the biaxial moduli (Eq.'s 3.3 and 3.4) are different, the relevant "biaxial Poisson ratios" $\nu^{111} = -\varepsilon_3^{111} \big/ \varepsilon_f^{111}$ and $\nu^{100} = -\varepsilon_3^{100} \big/ \varepsilon_f^{100}$ in the different texture components can be quite different [29, 30]. For FCC films having perfect (111) or (100) fiber texture and subjected to an equal biaxial stress (Eq. 3.1), these relationships are given by

$$\nu^{111} = -\frac{\varepsilon_3^{111}}{\varepsilon_f^{111}} = -\left(\frac{2C_{11} + 4C_{12} - 4C_{44}}{C_{11} + 2C_{12} + 4C_{44}} \right) \tag{3.5}$$

and

$$\nu^{100} = -\frac{\varepsilon_3^{100}}{\varepsilon_f^{100}} = -\left(\frac{2C_{12}}{C_{11}} \right), \tag{3.6}$$

respectively. For example, for Cu, $\nu^{111} = 0.73$ and $\nu^{100} = 1.44$. For Ag, $\nu^{111} = 0.90$ and $\nu^{100} = 1.51$. Even Al, which is relatively isotropic, has $\nu^{111} = 1.03$ and $\nu^{100} = 1.16$. Thus, the equilibrium out-of-plane strains in the different texture components will be quite different, even if the in-plane strain is everywhere the same.

At texture boundaries, however, the out of plane strains must be the same in both texture components unless sliding at the boundary is allowed. Thus, out-of-plane stresses will be generated near the boundary. Again, these out-of-plane stresses should decay within a few film thicknesses of the texture boundary so the average out-of-plane strain in each texture component is expected to depend on the aspect ratio, d_{tb}/t_f. For small values of d_{tb}/t_f (Fig. 3.1c), the out-of-plane strains cannot relax and isostrain conditions are approached, *i.e.* $\varepsilon_3^{100} = \varepsilon_3^{111}$. As d_{tb}/t_f becomes large (Fig. 3.1d), the out-of-plane strains should reach the equilibrium values given by Eq's 3.5 and 3.6 away from the boundary, so that the average out-of-plane stresses in both texture components approach zero. Of course, at the free surface the out-of-plane stress must be zero in all cases. The variation in the out-of-plane stress state from isostrain to zero

with increasing grain width/height ratios in films having mixed (111)/(100) fiber textures was demonstrated in finite element studies by Wikström and Nygårds [19]. Depending on aspect ratio, the average out-of-plane stresses reached 40% of the in plane stresses in their simulations.

3.4 THIN FILM X-RAY STRESS ANALYSIS

If the elastic constants are known, stresses can be accurately determined by using x-rays to determine the elastic strains and applying Hooke's law. The strain in any direction, $\varepsilon = (a\text{-}a_0)/a_0$, is found by using Bragg diffraction to determine the strained lattice spacing, a. The unstrained lattice spacing, a_0, must be known, either independently or from the measurement.

In thin films, an applied strain that is uniform in the film plane is common (arising from, *e.g.* differential thermal expansion or microstructural evolution). Although the local strains may vary due to inhomogeneity or anisotropy in deformation and grain-grain interactions, the average strain tensor for such a film, represented in film coordinates, must be of the form of Eq. 3.2. In this case, the strain along a direction at an angle ψ from the surface normal is given by

$$\varepsilon_\psi = (\varepsilon_f - \varepsilon_3)\sin^2\psi + \varepsilon_3 \ . \tag{3.7}$$

Equation 3.7 is the basis of the well-known "$sin^2\psi$ method" [31] upon which the vast majority of thin film and surface layer stress analyses are based. In this method, the principal strains, ε_f and ε_3, are found from the slope and intercept of the variation of measured ε_ψ *vs.* $\sin^2\psi$ values.

For films with mixed (111)/(100) texture, the average strain state within each texture component is also of the form of Eq. 3.2, due to the transverse isotropy of the biaxial moduli in these orientations. Therefore, the linear $sin^2\psi$ behavior of Eq. 3.7 is expected within each texture component. Since the orientations of the diffracting

crystallites are well known, Bragg reflections can be found which can be unambiguously attributed to a specific grain orientation. Thus, if enough reflections can be measured, the linear $\sin^2\psi$ analysis can be used to determine the average strain state for each orientation separately, and established single crystal elastic constants can then be used to calculate the stresses. Because this technique probes groups of similarly-oriented grains it is often called the *Crystallite Group Method* [32-34]. Variants of the crystallite group method have been used to characterize stresses in well-oriented thin films with single [21, 23-25, 35], or mixed [8, 12, 13, 22], fiber textures.

In the following, we develop a general description for the characterization of a triaxial stress state within both texture components of a film with mixed (111) and (100) fiber texture. As above, the average principal strain state in each texture component is of the form of Eq. 3.1. If we allow out of plane stresses arising from grain interactions, then, given the transverse symmetry of the biaxial moduli in both fiber texture components, the average stress state in each texture component is of the form

$$\sigma_{ij}^{hkl} = \begin{bmatrix} \sigma_f^{hkl} & 0 & 0 \\ 0 & \sigma_f^{hkl} & 0 \\ 0 & 0 & \sigma_3^{hkl} \end{bmatrix}. \tag{3.8}$$

Following a standard linear elastic analysis (*e.g.* see ref. [20]), Eq. 3.7 can then be rewritten in terms of the stresses and single crystal elastic constants. For a film with (111) fiber texture, we find

$$\varepsilon_\psi^{111} = \frac{a_\psi^{111} - a_0}{a_0} = \left(\frac{S_{44}}{2}\right)\left(\sigma_f^{111} - \sigma_3^{111}\right)\sin^2\psi + \frac{2S_{11} + 4S_{12} - S_{44}}{3}\sigma_f^{111} + \frac{S_{11} + 2S_{12} + S_{44}}{3}\sigma_3^{111}, \tag{3.9}$$

and, for a film with (100) fiber texture,

$$\varepsilon_{\psi}^{100} = \frac{a_{\psi}^{100} - a_0}{a_0} = \left(S_{11} - S_{12}\right)\left(\sigma_f^{100} - \sigma_3^{100}\right)\sin^2\psi \;, \qquad (3.10)$$
$$+ 2S_{12}\sigma_f^{100} + S_{11}\sigma_3^{100}$$

where the S_{ij} are the single crystal compliance constants.

To implement this method, diffraction peaks that can be unambiguously attributed to lattice planes from just one texture component are measured at a variety of ψ angles. The calculated values of a_{ψ}^{hkl} are plotted as a function of $\sin^2\psi$. Following Eq's 3.9 and 3.10, straight lines are fit to these data and the slopes m^{hkl} and intercepts b^{hkl} of these lines are determined. This yields a set of four equations, one each for m^{hkl} and b^{hkl} from each of the two texture components, in terms of the five unknown values $\sigma_f^{111}, \sigma_3^{111}, \sigma_f^{100}, \sigma_3^{100}$, and a_0.

Clearly an additional assumption is needed to solve for the stresses. The usual procedure, and that followed by VZB and BKA, as well as virtually all others who use a variant of this method, is to assume that the out-of-plane stress is zero everywhere, *i.e.* $\sigma_3^{111} = \sigma_3^{100} = 0$ in Eq's 3.9 and 3.10. With this constraint, it is straightforward to solve for the film stresses in each texture component, $\sigma_{f,B}^{111}$ and $\sigma_{f,B}^{100}$, separately. Furthermore, since there are now only three unknowns, it is possible to solve for the unstrained lattice parameters in the two texture components separately, yielding

$$a_{0,B}^{100} = b^{100} + m^{100}\frac{2S_{12}}{S_{12} - S_{11}} \quad \text{and} \quad a_{0,B}^{111} = b^{111} - m^{111}\frac{2}{3}\frac{2S_{11} + 4S_{12} - S_{44}}{S_{44}}. \quad (3.11)$$

Note that we indicate use of the biaxial stress state assumption by denoting the values determined using this method using a subscript *B*, *e.g.* $\sigma_{f,B}^{111}$, $a_{0,B}^{111}$, $\sigma_{f,B}^{100}$, and $a_{0,B}^{100}$.

To incorporate non-zero out-of-plane stresses in the present work, we impose a different constraint. The fact that the free surface cannot support normal tractions requires only that the average out-of-plane stress over the film volume be zero [26]. If

we treat the texture components as different homogeneous entities, this constraint simply requires that

$$\sum_{hkl} f^{hkl}\sigma_3^{hkl} = 0 \ , \tag{3.12}$$

where f^{hkl} is the volume fraction of crystallites having the *hkl* out-of-plane orientation and the sum is over the texture components. .

Equation 3.12 along with the equations for m^{100}, b^{100}, m^{111} and b^{111} from Eq's 3.9 and 3.10 now constitute 5 equations in the 5 unknowns, $\sigma_f^{111}, \sigma_3^{111}, \sigma_f^{100}, \sigma_3^{100}$, and a_0, which can be solved to find

$$a_0 = f^{100}\left(b^{100} + m^{100}\frac{2S_{12}}{S_{12}-S_{11}}\right) + f^{111}\left(b^{111} - m^{111}\frac{2}{3}\frac{2S_{11}+4S_{12}-S_{44}}{S_{44}}\right) \tag{3.13}$$

(note that this is just the weighted average of the unstrained lattice parameters calculated using the biaxial stress assumption in Eq. 3.11). Using this value of a_0, we find for the out-of-plane stresses,

$$\sigma_3^{111} = m^{111}\left(\frac{-2}{3}\right)\frac{(2S_{11}+4S_{12}-S_{44})}{S_{44}a_0(S_{11}+2S_{12})} + \frac{(b^{111}-a_0)}{a_0(S_{11}+2S_{12})} \tag{3.14a}$$

and

$$\sigma_3^{100} = \frac{2m^{100}S_{12}}{a_0(S_{11}+2S_{12})(S_{12}-S_{11})} + \frac{b^{100}-a_0}{a_0(S_{11}+2S_{12})} \ . \tag{3.14b}$$

And, for the in-plane stresses

$$\sigma_f^{111} = \frac{2m^{111}}{a_0 S_{44}} + \sigma_3^{111} \tag{3.15a}$$

and

$$\sigma_f^{100} = \frac{m^{100}}{a_0(S_{11}-S_{12})} + \sigma_3^{100} \ . \tag{3.15b}$$

If σ_3^{111} and σ_3^{100} are taken to be zero, Equations 3.15 are the same as those found for the film stresses $\sigma_{f,B}^{111}$ and $\sigma_{f,B}^{100}$ using the biaxial stress analysis, where the unstrained lattice parameters would be found using Eq. 3.11. By comparing the solutions for the in-plane stresses using the biaxial and triaxal stress state assumptions, it can clearly be seen that applying the biaxial stress assumption when in fact the stress state is triaxial, will result in erroneous values for the in-plane stresses following

$$\sigma_{f,B}^{hkl} \approx \sigma_f^{hkl} - \sigma_3^{hkl} \ , \tag{3.16}$$

where the approximation arises because of the different values of a_0—Eq. 3.11 or Eq. 3.13—that are used [36].

3.5 EXPERIMENTS

To compare results obtained using the traditional biaxial stress assumption with those obtained including out-of-plane stresses, a Cu thin film was prepared and the strains in the (111) and (100) fiber texture components were measured using x-ray diffraction during thermal cycling at the Cornell High Energy Synchrotron Source (CHESS).

Specifics of the film preparation process have been reported elsewhere [14]. Briefly, a thin copper film was sputter deposited from a 99.999% pure target onto a 50 nm SiN_x barrier layer that had been prepared by plasma enhanced chemical vapor deposition on a 100 mm Si (001) substrate. Deposition was performed in ultra high vacuum (UHV) with a base pressure of 1.5×10^{-10} Torr. Cu was deposited at a rate of 60 nm/min to a thickness of 500 nm. The Cu film was immediately capped with a 50 nm SiN_x passivation layer by reactive sputtering. The sample was then transferred *in situ* in UHV to a chamber where ultra-high-purity, oxygen-filtered helium was introduced and the sample was thermally cycled once to 500°C to stabilize the microstructure. The specimen was then exposed to atmosphere before all subsequent characterization.

To characterize the grain size, a Ga-ion beam in a focused ion beam (FIB) microscope was used to strip the passivation from a 30 × 30 μm^2 area of the surface of the film. The grain structure was then imaged by channeling contrast with a beam energy of 30 kV and no specimen tilt. The grain size distribution was determined by calculating the area of each grain in order to determine effective grain diameters. A total of 404 grains were used in the analysis. The frequency of twins was also determined by counting the number of twins within a subset of 367 of these grains.

Film texture was characterized using Electron Backscattered Diffraction (EBSD) (HKL Nordlys detector on a Leica 440 scanning electron microscope, HKL Channel 5 EBSD analysis software). Imaging was performed at a working distance of 20 mm with a specimen tilt of 70° and beam voltage of 25 kV. Prior to EBSD imaging, the SiN_x passivation layer was removed using an ion mill for 10 minutes at 3 kV and 5 mA. The ion beam was oriented at 12˚ with respect to the sample surface and the sample was rotated in-plane 360° during milling. To quickly obtain a statistically significant sample size for texture analysis, several line scans with a 0.1 μm step size were performed along arrays of parallel lines 40 μm in length separated by 5 μm at various locations on the sample. Area fractions of (100) and (111) oriented grains were calculated using the HKL software including all grains within a 15° of the film normal.

X-ray strain measurements of (100) and (111) oriented grains were performed as a function of temperature using a Huber (Rimsting, Germany) four circle diffractometer in the Ω-geometry at the C1 beamline at CHESS. The specimen was placed on a high-temperature sample stage consisting of a ceramic heater that was pressed against a metal reference plane from behind using springs. The reference plane is water cooled and displacements of the sample surface away from the center of rotation during thermal cycling were found to be minimal. The heater stage was placed

in a sealed chamber with a beryllium window. The chamber was evacuated with a rotary-vane pump and then filled with a reducing gas mixture of high purity N_2 with 900 ppm CO to remove oxygen from the system. The gas flowed over the sample continuously at atmospheric pressure during experiments at a rate of a few sccm. The sample temperature was monitored using a K-type thermocouple located between the specimen and heating element. The sample stage, gas handling system, and calibration procedures have been described in more detail elsewhere [37]. A double-bounce Si (111) monochromator was used to select an x-ray energy of 8 keV. Diffraction was performed in the vertical plane and the beam dimensions were set by upstream slits to 3 mm horizontal by 1 mm vertical. To speed diffraction measurements and minimize sample relaxation during data collection, entire diffraction peaks were captured simultaneously using an Ordela 1100x (Oak Ridge, TN USA) linear position sensitive detector.

Four Bragg peaks were measured at each sample temperature. For grains having (100) orientations, {420} reflections were measured at $\psi = 26.6°$ and 63.4°. For the (111) texture component, reflections from the {331} planes at $\psi = 22.0°$ and 48.5° were used. For each diffraction peak, a linear background was subtracted and a Gaussian distribution was fit to the data. The peak position was used to determine the strained lattice parameters, a_{ψ}^{hkl}, for each of the four sets of lattice planes at each temperature.

3.6 RESULTS, ANALYSES, AND INTERPRETATION

The FIB and EBSD measurements showed the film to have a typical polycrystalline microstructure with (111) and (100) texture components. For x-ray stress analyses, the measured a_{ψ}^{hkl} values were plotted *vs.* $\sin^2\psi$ and the slope, m^{hkl}, and intercept, b^{hkl}, of a line fit to these data for each texture component were calculated. These values and the

volume fractions of the texture components were then used to determine stresses using both the conventional biaxial stress assumption and the criterion that out of plane stresses average to zero as described in Section 3.4 In all calculations, single crystal elastic constants from references [38, 39] and thermal expansion coefficients from [40, 41] were used.

3.6.1 Microstructure

The FIB imaging revealed a highly twinned grain structure with a median grain size of 455 nm. The average volume-weighted grain size, which is representative for x-ray measurements, was 550 nm. Each grain had one twin on average. EBSD analysis showed the film to be highly textured with strong (111) and (100) fiber components along with randomly distributed orientations. The volume fractions were $f^{111} = 0.6$, $f^{100} = 0.2$, and a fraction of randomly oriented grains $f^{rand} = 0.2$. The half-widths for the distributions of (100) and (111) orientations with ψ about the film normal were both about 6°. To facilitate our x-ray data analysis, we neglect the random fraction and define effective volume fractions as $f_e^{111} = f^{111} \Big/ \left(f^{111} + f^{100} \right) = 0.75$ and $f_e^{100} = f^{100} \Big/ \left(f^{111} + f^{100} \right) = 0.25$. Since the random component is expected to have little influence on the measured Bragg peaks, and since all other grain orientations have biaxial moduli and Poisson ratios that lie between those of the (111) and (100) texture components, this approximation should be acceptable.

3.6.2 Stress analysis using the biaxial stress assumption

We first present the film stresses and strains calculated from the x-ray data using the conventional assumption that the stress state within each texture component is biaxial, *i.e.* $\sigma_3^{111} = \sigma_3^{100} = 0$ as described in Sec 3. That is, we use the values of m^{hkl} and b^{hkl} to

determine $\sigma_{f,B}^{hkl}$ and $a_{0,B}^{hkl}$ at each temperature for the (111) and (100) texture components individually.

The strains and stresses determined for each texture component are shown as a function of temperature in Figure 3.2. These results are in excellent agreement with those of BKA who used the same data analysis procedure in all pertinent details. They also agree well with the results of VZB who measured only out-of-plane strains and calculated film stresses using Eq's 3.1-3.6. In both cases, the shapes of the thermal cycle hystereses are similar. The in-plane strains in the (100) texture component are generally somewhat larger than those in (111) throughout the thermal cycle but the difference in the moduli makes it such that the stresses are significantly larger in (111)- than in (100)-oriented grains, particularly at low temperature. For comparison the stress ratio at room temperature was $\sigma_{f,B}^{111}/\sigma_{f,B}^{100}$ = 1.8 (3.2b) for our 500 nm passivated film, 2.0 for BKA's 1000 nm passivated film, and 1.4 for VZB's 800 nm unpasivated film. Since our results are essentially the same as those of VZB and BKA, we use them to discuss the validity of the biaxial analysis method.

The predicted thermoelastic behavior has been interpreted as a check on the accuracy of the data in a themomechanical stress measurement [12]. We note that, if strain transfer between texture components occurs, it is no longer sensible to compare the in-plane strains determined from the individual texture components with predicted thermoelastic behavior. However, it *is* possible to check the accuracy of the method by comparing the *unstrained* lattice parameters obtained from the x-ray data analysis with the expected thermal expansion behavior.

Figure 3.3 shows $a_{0,B}^{111}$ and $a_{0,B}^{100}$ plotted as a function of temperature. There is a systematic difference between these values, particularly at room temperature. The solid lines show the expected behavior starting at the values of $a_{0,B}^{111}$ and $a_{0,B}^{100}$ determined from the experiment at room temperature and extrapolating using the

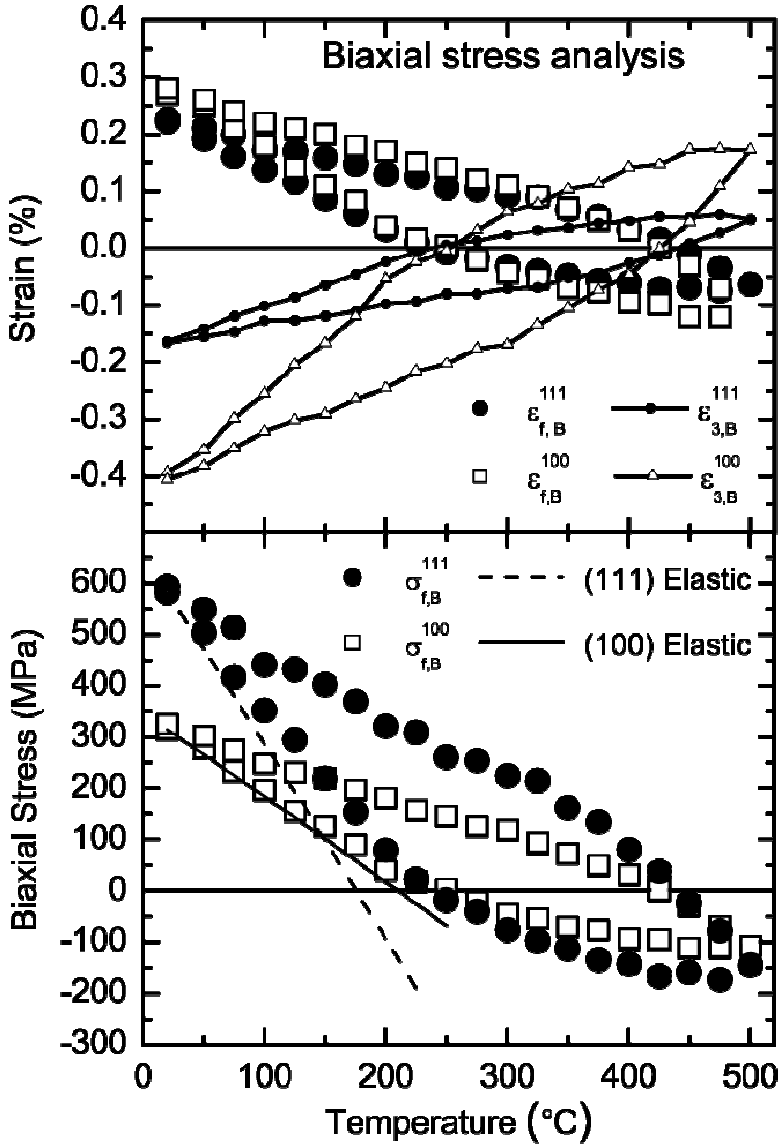

Figure 3.2: In-plane (a) elastic strains and (b) biaxial stresses calculated from x-ray data taken from the (111) and (100) fiber texture components in a Cu film using the assumption that the stresses in the out-of-plane direction are everywhere zero as described in Sec. 3.4. In agreement with others who also used this method [12], the film stresses in the texture components are very different. The solid lines (b) show the predicted thermoelastic behaviors. The relationship of the data to the predictions indicates that there are systematic errors in the analysis.

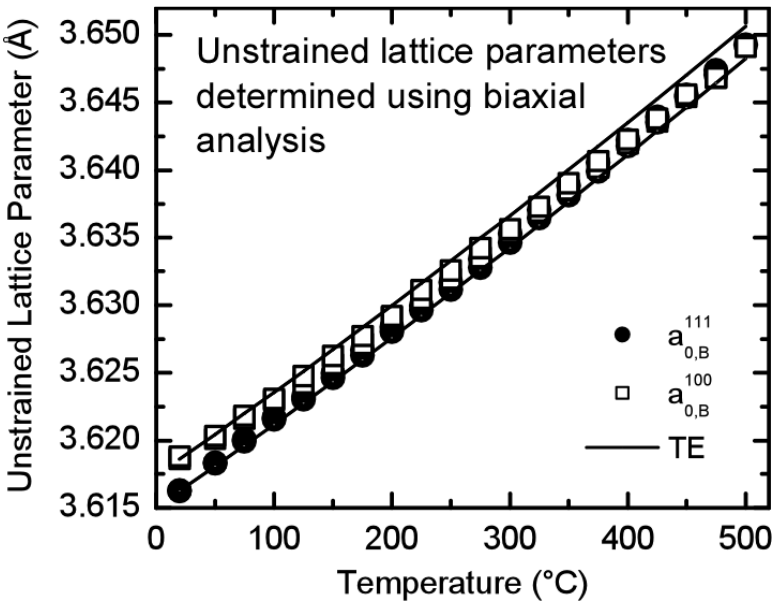

Figure 3.3: The unstrained lattice parameters in the (111) and (100) texture components calculated using Eq. 3.11 in the biaxial analysis used to find the stresses shown in Fig. 3.2 as a function of temperature. The solid lines show the expected thermal expansion behavior for each texture component using room temperature values as initial values. An unphysical systematic difference between the unstrained lattice parameters in the two orientations reaches about 0.07% at room temperature, indicating again that there are systematic errors in the analysis.

temperature-dependent thermal expansion coefficient. The (111) orientation follows the expected behavior more closely, while the (100) grains deviate significantly. Since Cu is cubic, the thermal expansion coefficient is isotropic. Therefore, differences in a_0 between the texture components are unphysical, indicating that there are errors in the analysis. The observed errors are inconsistent with misalignment of the diffractometer, which would lead to a constant offset at all temperatures. A temperature-dependent sample displacement error also cannot account for these variations, as the response of the measured Bragg reflections to sample offsets was calculated and cannot reproduce these trends. A simple error in the measured temperature also cannot explain the deviations from thermal expansion. Instead, the errors appear to arise from the assumption of a biaxial stress state.

Figure 3.4 shows that the discrepancies in the lattice parameter are correlated with the calculated biaxial stresses. Here, the differences in the unstrained lattice parameters in the two different texture components, normalized by the difference at room temperature (*i.e.* $(a_{0,B}^{111} - a_{0,B}^{100})_T/(a_{0,B}^{111} - a_{0,B}^{100})_{RT}$), and the differences in the stresses in the two different texture components, normalized by the difference at room temperature (*i.e.* $(\sigma_{f,B}^{111} - \sigma_{f,B}^{100})_T/(\sigma_{f,B}^{111} - \sigma_{f,B}^{100})_{RT}$), are plotted as a function of temperature. It is evident that the systematic deviations in a_0 are directly correlated with the differences in the calculated biaxial stresses. Clearly the analysis based on assumption of a biaxial stress state leads to significant systematic errors in the unstrained lattice parameter and in the calculated stresses.

3.6.3 Stress analysis including out-of-plane stresses

The same x-ray data were reanalyzed allowing the average out-of-plane stresses in the different texture components to be non-zero under the condition that Eq. 3.12 is satisfied. In this case, we used the measured values of m^{hkl} and b^{hkl} in Eq. 3.13 to

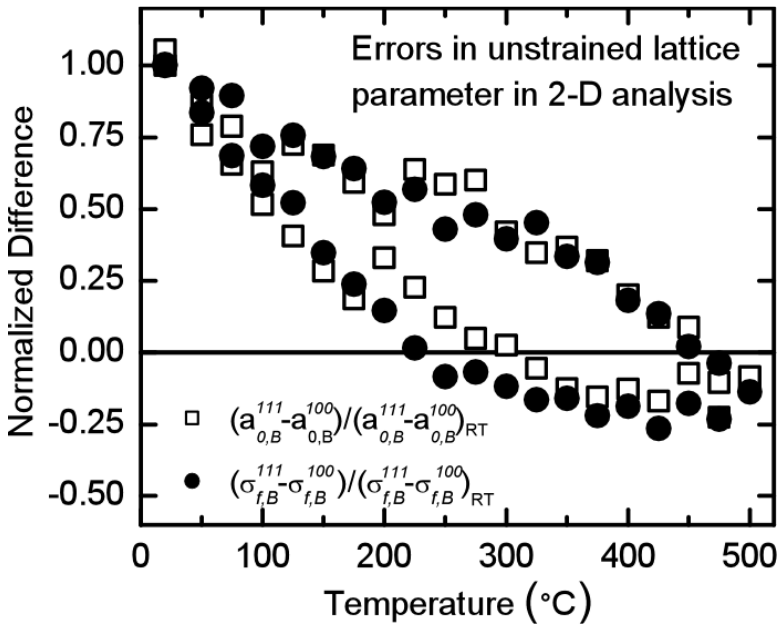

Figure 3.4: The differences in the lattice parameters and stresses calculated for the (111) and (100) texture components using the biaxial analysis (Fig.'s 3.2 and 3.3 respectively) as a function of temperature, normalized by the differences in those quantities at room temperature. That these differences scale with each other again indicates that there are systematic errors in the analysis. The correlation indicates that the deviations in the unstrained lattice parameter (Fig. 3.3) arise from errors in the stress analysis (Fig. 3.2)

determine a single value of a_0 at each temperature. Both in-plane and out-of-plane stresses were calculated using Eq.'s 3.14 and 3.15.

The in- and out-of-plane strains and stresses in each texture component are shown as functions of temperature in Figure 3.5. This new analysis yields a very different picture of the stress distribution than that provided by the conventional biaxial stress analysis (Fig. 3.2). In particular the two texture components exhibit nearly the same stress in the film plane throughout the temperature cycle, reaching a maximum of about 550 MPa at room temperature. The out-of-plane stresses are also sizeable, with a difference in σ_3^{hkl} between the two texture components that reaches almost 300 MPa at room temperature. The strains generated by the two analyses are qualitatively similar.

As a check on the veracity of the results, the values of a_0 determined using Eq. 3.13 are shown as a function of temperature in Figure 3.6, along with the expected temperature-dependent thermal expansion behavior. Excellent agreement between calculated and predicted behaviors is seen.

3.7 DISCUSSION

The triaxial stress analysis presented here gives very different results (Fig. 3.5) from the biaxial analysis (Fig. 3.2) that has been used to analyze similar films in the past [8, 12, 13]. In the following sections, we discuss the reasonableness of the triaxial stresses in Fig. 3.5, discuss the implications of these stress states on thin film behavior, and revisit conclusions about film behaviors based on biaxial stress analyses [8, 12, 13].

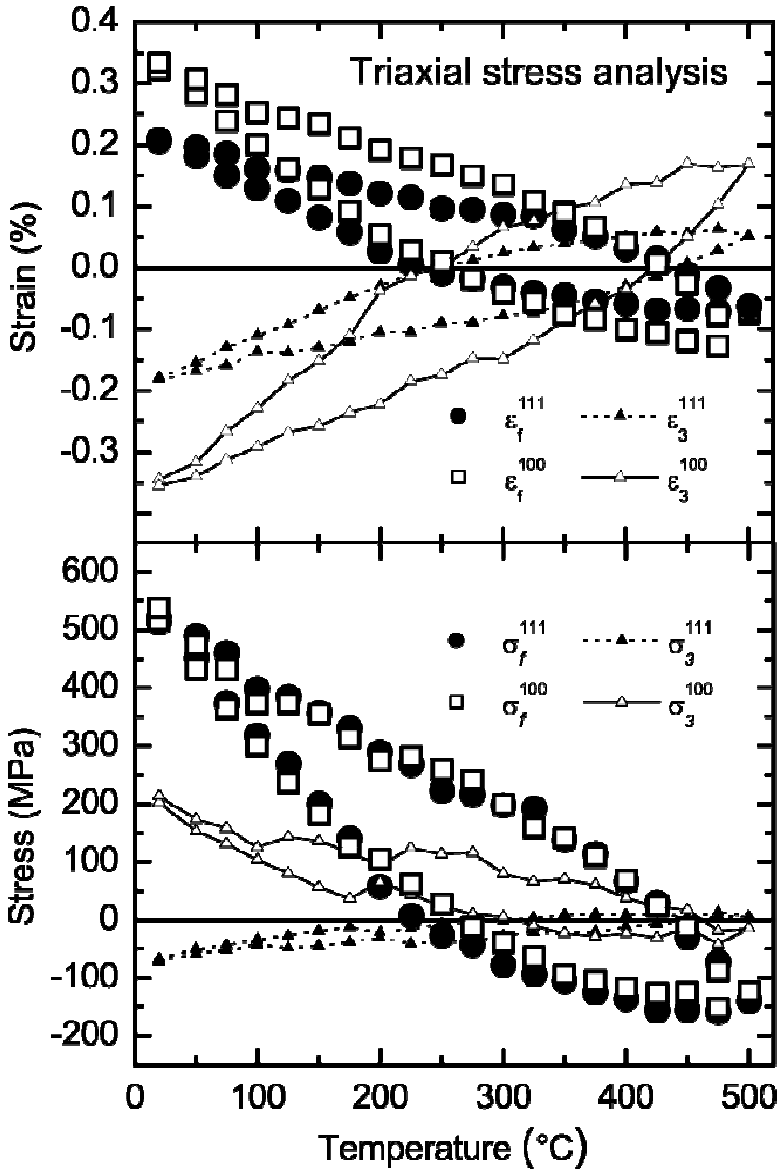

Figure 3.5: In-plane (a) elastic strains and (b) stresses calculated from $\sin^2\psi$ x-ray data taken from the (111) and (100) fiber texture components in a Cu film allowing non-zero out-of-plane stresses as described in Sec. 3.4. In contrast to the biaxial analysis of the same x-ray data shown in Fig. 3.2, the in-plane stresses in the texture components are very similar to each other throughout the temperature cycle. These data are very different from previous results based on the biaxial stress assumption. The out-of plane stresses are significant.

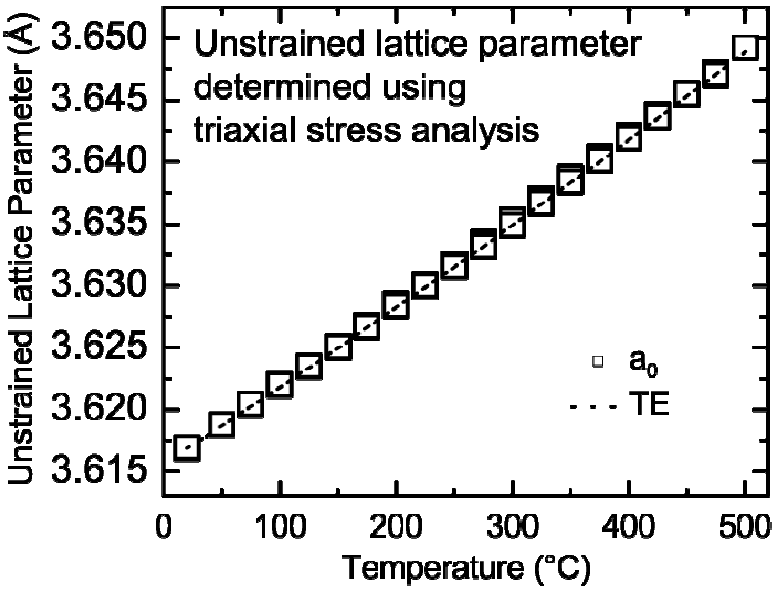

Figure 3.6: The unstrained lattice parameter calculated using Eq. 3.13 in the triaxial analysis used to find the stresses shown in Fig. 3.5 as a function of temperature. The solid line shows the expected thermal expansion behavior. The agreement between the calculated unstrained lattice parameter and the expected thermal expansion is excellent.

3.7.1 Reasonableness of the triaxial stress state

As described in the introduction, the key microstructural feature in determining the average stress states within the different texture components is the texture boundary spacing, d_{tb}. If $d_{tb} >> t_f$, then isostrain conditions will be approached in-plane and the average stresses in the out-of-plane direction will approach zero. If $d_{tb} << t_f$, then isostress conditions will be approached in-plane and out-of-plane stresses are expected.

In the present work, it was not possible to get a direct measurement of d_{tb}. The FIB images provide accurate measurements of grain spacings d_{gb}, but little information about orientations, while EBSD gives accurate orientation data, but with low spatial resolution (≈ 100 nm). However, it is possible to develop a reasonable estimate for d_{tb} from d_{gb} and the average number of twins per grain.

To do so, it is important to realize that twin boundaries always represent texture boundaries. For the case of films with mixed (111)/(100) texture, twin boundaries play a particularly interesting role. Twinned regions within (100) grains have (221)-type out-of-plane orientations, which is only 15.7° from the (111) direction, while twinned regions in (111) grains have (511)-type orientations, which is only 15.7° away from (100). Thus, a film with twinned 100 and 111 grains can be thought of as having four texture components, (100), (111), (221) and (511). Due to the close proximity of the (111) and (221) orientations, they will exhibit similar elastic behavior and to a first approximation can be treated as members of the same texture component. A similar argument applies to the (100) and (511) orientations,

Because there is, on average, one twin per grain in our Cu samples, and some grain boundaries are also texture boundaries, the texture boundary spacing, d_{tb}, must be smaller than the grain boundary spacing (550 nm). Since the nominal film thickness is 500 nm, the distance between texture boundaries is similar to the film thickness.

With this aspect ratio, and strain transfer distances of more than a film thickness from boundaries [27, 28], the in-plane isostress behavior shown in Fig. 3.5 is reasonable.

Additionally, the very good agreement of the temperature dependence of the unstrained lattice parameter obtained from the triaxial analysis with established thermal expansion data (Fig. 3.6) lends confidence to the analysis, especially when compared with the results of the biaxial analysis (Fig. 3.3).

The reasonableness of the stress states shown in Fig. 3.5 are further supported by detailed finite element studies by Wikström and Nygårds [19], who modeled Cu grain structures and assigned orientations such that f_e^{111} = 82.2% and f_e^{100} = 17.8%. Although their volume fractions are slightly different from ours and their films are unpassivated and untwinned, the ratios of out-of-plane to in-plane stress in the different texture components, taken at the same grain aspect ratio as d_{gb}/t_f for our films, are similar to ours at room temperature. For $\sigma_3^{111}/\sigma_f^{111}$ they find -0.09 *vs.* our -0.13, and for $\sigma_3^{100}/\sigma_f^{100}$ they find 0.19 *vs.* our 0.39. The differences are consistent with the difference in passivation and the prevalence of twin boundaries in our film, which will decrease d_{tb} and enhance out-of-plane stresses.

We note that an interesting feature of the biaxial analysis that appeared to support its validity does not actually do so. BKA compared the volume average of the in-plane stresses obtained using x-rays,

$$\sigma_{avg} = f_e^{100}\sigma_{f,B}^{100} + f_e^{111}\sigma_{f,B}^{111} \quad , \tag{3.17}$$

with stress-temperature data obtained independently using a substrate curvature method on similar samples. They found nearly identical results and concluded that neither the x-ray nor the substrate curvature data suffered from significant systematic errors. However, using Eq. 3.16 to replace the stresses obtained using the biaxial stress analysis with the "real" stresses and applying the force balance of Eq. 3.12, it is clear that the volume averaged in-plane stress is the same regardless of whether the bi- or

tri-axial analysis is employed. Thus, this agreement does not validate BKA's reported biaxial stress states.

Thus, we conclude that the stresses determined using our version of the crystallite group method and accounting for out-of-plane stresses, as shown in Fig. 3.5, provide a reasonable description of the average stress states within the (111) and (100) texture components of our film.

3.7.2 Effects of triaxial stress states in thin films

Interest in stress-related phenomena in thin metal films has been high due to the implications for device integrity and reliability. Models for film strength [1, 42, 43], strain hardening [44], stress voiding [45], hillocking [46, 47], abnormal grain growth [48], diffusional relaxation [49-51], and texture formation [16, 52] have been presented. These models generally assume simple biaxial stress states. However, in some cases, model predictions would be different if triaxial stress states were considered. Here we provide the first data for two brief examples: the dimensional constraint on dislocation motion and texture formation.

3.7.2.1 Thin film strength

An intrinisic size effect in the strength of passivated films arises because, in order for a threading dislocation (spans the thickness of the film) to move to relax stresses, misfit dislocation line length must be generated at the film/substrate and film/passivation interfaces. The threading dislocation cannot move ahead unless the strain energy relaxed is equal to or greater than the energy cost of the misfits. Solutions to this problem have been presented [53, 54], and Freund [42] and Nix [1] both generated formulae for the critical stress, referred to by Nix as the "channeling stress," above which dislocations can move. These calculations are all based on a

homogeneous, transversely isotropic, biaxial stress state and provide a single threshold stress level for plasticity in a film.

In contrast, given a transversely isotropic triaxial stress state, as in the present study, the criterion for dislocation motion depends on both the in- and out-of-plane stresses and, following Nix [1], can be shown to be

$$\left|\sigma_f - \sigma_3\right| > \frac{\sin\phi}{\cos\phi\cos\lambda}\frac{b\mu_{eff}}{4\pi(1-\nu)t_f} \quad , \tag{3.18}$$

where ν is the Poisson ratio, b the Burgers vector, t_f the film thickness, ϕ and λ determine the orientation of the slip plane, and μ_{eff} can be considered an effective shear modulus including the shear moduli of the substrate, film, and passivation [15]. Unlike previous descriptions, which include only the film stress, this criterion for dislocation motion depends on both in- and out-of-plane stresses. Thus, a yield locus plot, as shown in Figure 3.7, is a convenient way to visualize the stress states under which dislocation motion may occur. Fig. 3.7 shows yield boundaries calculated using Eq. 3.18 along with the data from Fig. 3.5. The out-of-plane stresses in the (100) texture component increase the hydrostatic stress for this orientation, keeping the trajectory of the data closer to the yield boundary. In the (111) orientation, the out-of-plane stress increases the deviatoric stress, driving this component away from its yield surface, and revealing more hardening than in (100) grains. Of course, yield trajectories are expected to depend on texture fractions and texture boundary spacings so this type of plot is a way to distinguish the plastic behavior of different films.

Surprisingly, in Fig. 3.7 the stress ratios, $\sigma_3^{hkl}/\sigma_f^{hkl}$, remain roughly constant at 0.3 and -0.1 in the (100) and (111) orientations, respectively, during the entire thermal cycle, though it is not yet clear why this should be the case. A strong Bauschinger

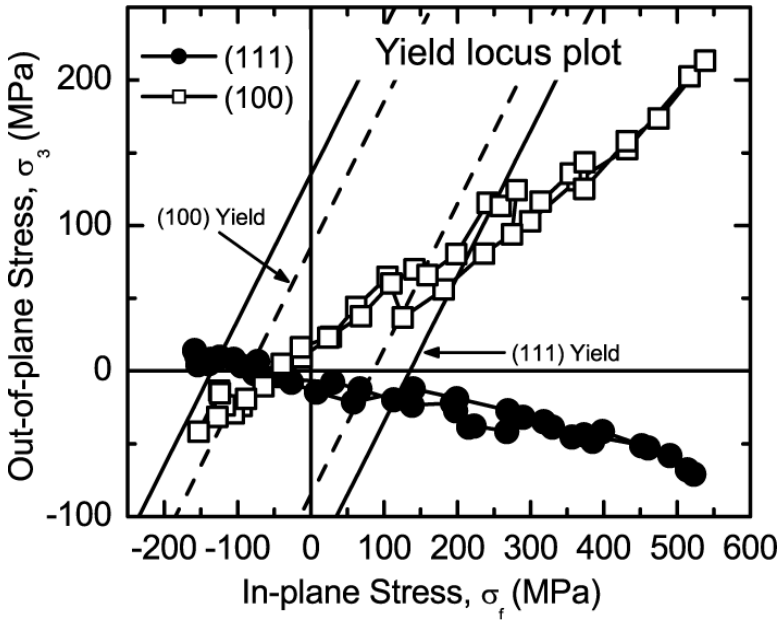

Figure 3.7: A yield locus, showing the loading trajectories of the (111) and (100) orientations with respect to their yield criteria. In the (100) orientation, the out-of-plane stress draws loading more parallel to the yield locus, delaying yield and resulting in less hardening. In the (111) orientation, the out-of-plane stress directs loading nearly perpendicular to the yield surface, promoting early yield and increasing hardening.

effect may help to account for the lack of hysteresis, and the lack of a sharp change in behavior at the yield boundary may be due to the fact that the stress state is inhomogeneous, leading to yielding at different times in different regions. In any event, the onset of yielding in a film with mixed texture and triaxial stresses is much more complicated than a description based on a simple single-valued channeling stress.

3.7.2.2 Texture in thin films

As described in the introduction, in FCC metal films, a (111) texture minimizes interface energy, while, for a given strain, the (100) orientation minimizes the strain energy density. A simple thermodynamic model has been presented to predict when (111) and (100) fiber textures occur in FCC films [16, 52]. A biaxial isostrain analysis is used, and the stresses (and strain energies) are accordingly very different in the different texture components. As a result, a (111) texture is expected for thinner films while (100) is expected for thicker films. This model cannot account for films with mixed texture

However, due to stress interactions between texture components, the strain energies in different orientations cannot be decoupled. Figure 3.8 shows the strain energies in the different texture components based on the triaxial stress states in Fig. 3.5. The strain energies in both orientations were found to be roughly equal throughout the entire temperature cycle. This may explain the stability of mixed texture in many samples. Not only can grain interactions affect strain energies, but these interactions will also change during secondary grain growth as the texture boundary spacing evolves [55]. In order to fully understand texture formation in thin films, the effect of grain interactions on strain energies must be incorporated into the existing models.

3.7.3 Re-interpretation of previous analyses

Our samples were prepared using methods similar to those used by VZB, BKA and H&K, and BKA and H&K reported grain sizes and texture volume fractions similar to ours. While texture boundary spacings were not reported in any of these works, we assume that these are also similar so that the films in all of these studies would have similar responses to applied strain. We thus reinterpret their results in light of the present triaxial stress analysis.

3.7.3.1 Biaxial stress analyses

The biaxial stress analysis data presented in Fig. 3.2 are the same as those obtained by BKA in all substantive ways. Therefore, we assume that, had the BKA data been analyzed using our triaxial method, the results would look very similar to those in Fig. 3.5. This has several consequences for their conclusions.

- BKA found $\sigma_f^{111}/\sigma_f^{100} \approx 2.3$, the ratio of the biaxial moduli during cooling, concluded that isostrain conditions prevailed, and speculated that the spacing between texture boundaries might be quite large. The triaxial analysis applied to their data should show behavior closer to isostress, removing the restriction on texture boundary spacing.
- BKA noted that strain hardening was much higher in (111) than in (100) texture components. As indicated by Eq. 3.16, the maximum shear stresses in each texture component determined by the biaxial and triaxial analyses are the same. Thus, their conclusions about strain hardening hold despite their inaccurate view of the nature of the stress state.

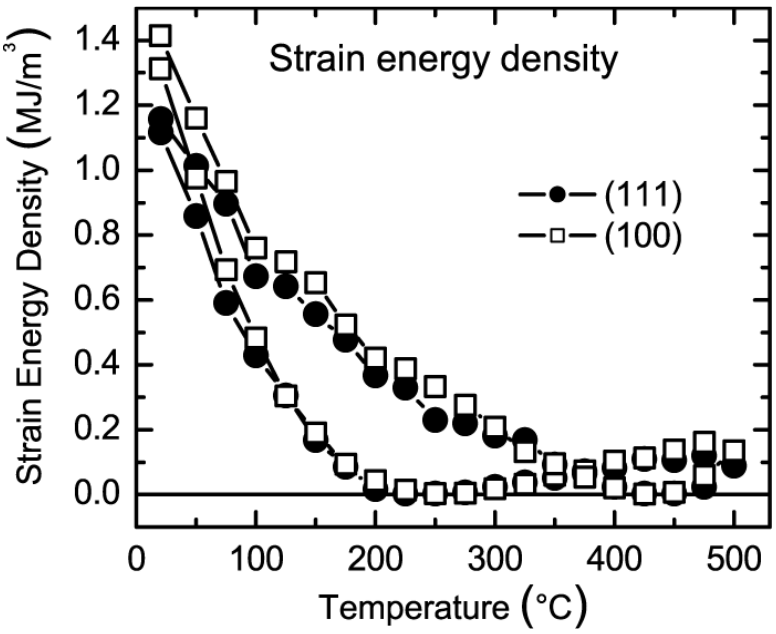

Figure 3.8: Strain energy densities, calculated from the triaxial analysis results, for the (111) and (100) texture components as a function of temperature. Throughout the temperature cycle, strain energy densities in the two orientations are roughly the same. Understanding the role of grain interactions in this case will help to improve models for texture prediction in thin films.

- BKA noted that only very short regions of the initial unloading $\varepsilon_f(T)$ data in each of the texture components followed the expected thermal expansion line and concluded that this might be due a dislocation-based Bauschinger effect. We argue it is not possible to unambiguously state when either texture component is exhibiting elastic behavior due to the complexity of grain interactions. However, it is straightforward to show that, for purely elastic behavior

$$\varepsilon_{th} = f^{111}\varepsilon_f^{111} + f^{100}\varepsilon_f^{100}. \tag{3.19}$$

Using the strain data from Fig. 3.5, this volume averaged elastic strain is plotted along with the expected thermoelastic behavior in Fig. 3.9. It appears that purely elastic behavior is indeed limited to the initial stages of heating, consistent with a Bauschinger effect due to dislocation recovery [56].

VZB obtained stresses in the texture components in their films independently by measuring only the out-of-plane strain and using the assumption σ_3=0 everywhere. They too obtained results that appear similar to Fig. 3.2 which can probably also be reinterpreted in a way similar to that described here.

3.7.3.2 Tensile tests

H&K deposited Cu films on polyimide substrates and subjected them to uniaxial tension. They used a $\sin^2\psi$ method to measure lattice parameters in the plane containing the tensile axis and the film normal, using an unstrained lattice parameter determined prior to loading using Eq. 3.11. The strains along the tensile axis, ε_x^{hkl}, and film normal, ε_z^{hkl}, directions were calculated. The assumption that $\sigma_z^{hkl} = 0$ then allowed the strain along the transverse axis, ε_y^{hkl}, and thus the stresses σ_x^{hkl} and σ_y^{hkl} to be calculated using Hooke's law.

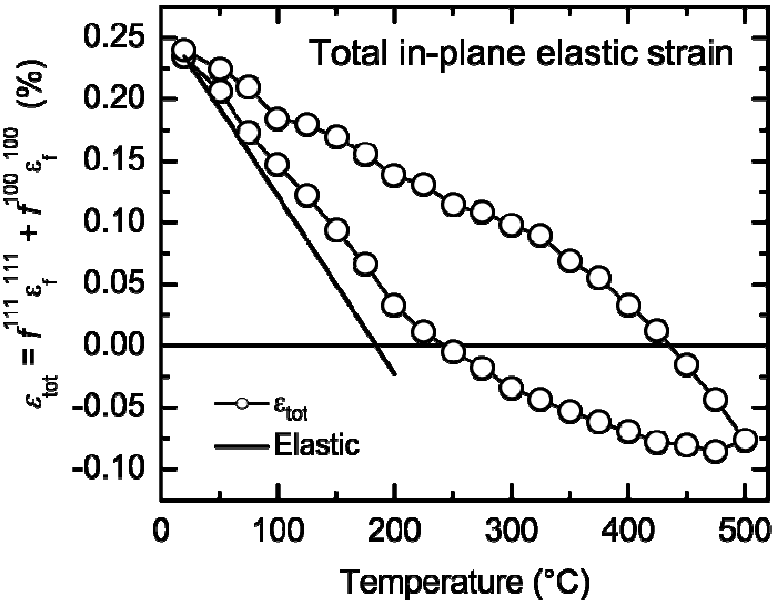

Figure 3.9: The weighted sum of the in-plane elastic strains in the (111) and (100) orientation, obtained from the triaxial stress analysis (Fig. 3.5a), as a function of temperature. The solid line is the expected thermoelastic behavior on heating. It appears purely elastic behavior of the film as a whole is limited to the very beginning of the heating cycle.

Although a different biaxial stress state was assumed, the H&K results are qualitatively similar to the BKA results in that isostrain conditions are found along the tensile axis; again apparently indicating little or no interaction among texture components. However, given the similarities in microstructure, texture interactions in the plane of the film should be expected. Unfortunately, for this loading case it is not possible to solve for the full triaxial stress state without additional x-ray measurements in the plane transverse to the loading axis. Such measurements would be similar to previous characterizations of triaxial stress states within patterned metal lines [21, 57].

3.8 SUMMARY AND CONCLUSIONS

We have presented a variation of the $\sin^2\psi$ x-ray analysis which allows the average triaxial stress states within the (100) and (111) texture components of a mixed texture thin film to be calculated, and applied it to experimental measurements of a Cu film during thermal cycling. Instead of the widespread assumption that the out-of-plane stresses are zero everywhere within such a film, our approach imposes the constraint that the sum of these stresses be zero.

As in previous studies, stresses calculated using a biaxial stress analysis exhibited nearly iso-strain conditions, such that the in-plane stresses within the two texture components were very different. In contrast, the present triaxial analysis reveals the in-plane stresses to be nearly the same in the (100) and (111) texture components throughout thermal cycling. Additionally, out-of-plane stresses were found to be significant—40% of the in-plane stress in the (100) component—and very different from each other.

Applying a biaxial analysis to our experimental data produces results that closely resemble results from previous investigations. However, in contrast to those results, our triaxial analysis correctly reproduced the expected thermal expansion

behavior of the unstrained lattice parameter, and generated stress states consistent both with the experimentally-determined texture boundary spacing to film thickness aspect ratio and with previous finite element studies, lending confidence to the accuracy of this method. By comparing the biaxial and triaxial analysis methods, we determined that, while the conclusions about the stress states based on the biaxial analysis were incorrect, the findings that the strain hardening rate is significantly higher in (111)- than in (100)-oriented grains, and that a significant Bauschinger effect occurs upon initial heating, were correct.

The new results cast the interpretation of many stress-driven phenomena in thin films in a new light, in which accurate knowledge of the full triaxial stress state is critical to understanding. For example, the "channeling stress" becomes not a single-valued film stress at which yielding occurs, but rather a yield criterion, with experimental data best presented on a yield plot such as that shown in Fig. 3.7. The keys to understanding the trajectories of the data in such a plot lie in understanding strain transfer between and plastic deformation in the texture components. As a second example, we found (Fig. 3.8) that strain transfer occurs such that the strain energy remains the same in the texture components throughout the temperature cycle, except near room temperature—where, against expectations, the (111) component has lower strain energy. Clearly strain transfer affects the stress state, and therefore the strain energy in any thermodynamic argument that attempts to predict texture by minimizing strain and interface energies. Accurate knowledge of the (triaxial) stress state should make possible better models for film deformation, texture formation, and a host of other stress-driven phenomena in thin films.

3.9. ACKNOWLEDGEMENTS

AMV was supported in this work by an Applied Materials Fellowship. The work of DEN and SPB in this project was supported by DoE (DE-FG02-02ER46001). SL and OT participated via an NSF-CNRS international collaboration program (INT-0233283). Part of this work was conducted at the Cornell High Energy Synchrotron Source (CHESS) which is supported by NSF and NIH/NIGMS under NSF award DMR-0225180. The authors would like to thank Jonathan B. Shu for sample preparation, Claude Alfonso for FIB imaging, and Ken Finkelstein for assistance at CHESS.

REFERENCES

1. Nix WD. Metallurgical Transactions A 1988; 20A: 2217.
2. Spearing SM. Acta Materialia 2000; 48: 179.
3. Tu KN. Journal of Applied Physics 2003; 94: 5451.
4. Chopra KL, Paulson PD, Dutta V. Progress in Photovoltaics 2004; 12: 69.
5. Love JC, Estroff LA, Kriebel JK, Nuzzo RG, Whitesides GM. Chemical Reviews 2005; 105: 1103.
6. Litster S, McLean G. Journal of Power Sources 2004; 130: 61.
7. Venkatraman R, Bravman JC. Journal of Materials Research 1992; 7: 2040.
8. Vinci RP, Zielinski EM, Bravman JC. Thin Solid Films 1995; 262: 142.
9. Thouless MD. Annual Review of Materials Science 1995; 25: 69.
10. Vinci RP, Vlassak JJ. Annual Review of Materials Science 1996; 26: 431.
11. Arzt E. Acta Materialia 1998; 46: 5611.
12. Baker SP, Kretschmann A, Arzt E. Acta Materialia 2001; 49: 2145.
13. Hommel M, Kraft O. Acta Materialia 2001; 49: 3935.
14. Shu JB, Clyburn B, Mates TE, Baker SP. Journal of Materials Research 2003; 18: 2122.
15. Keller R, Baker SP, Arzt E. Journal of Materials Research 1998; 13: 1307.
16. Thompson CV. Annual Review of Materials Science 2000; 30: 159.
17. Knorr DB, Tracy DP. Materials Chemistry and Physics 1995; 41: 206.
18. Sonnweber-Ribic P, Gruber P, Dehm G, Arzt E. Acta Materialia 2006; 54: 3863.
19. Wikstrom A, Nygards M. Acta Materialia 2002; 50: 857.
20. Clemens BM, Bain JA. MRS Bulletin 1992; 17: 46.
21. Flinn PA, Chiang C. Journal of Applied Physics 1990; 67: 2927.
22. Zielinski EM, Vinci RP, Bravman JC. Applied Physics Letters 1995; 67: 1078.

23. Zoo Y, Alford TL. Journal of Applied Physics 2007; 101: 033505.
24. Korhonen MA, Paszkiet CA. Scripta Metallurgica 1989; 23: 1449.
25. Leung OS, Munkholm A, Brennan S, Nix WD. Journal of Applied Physics 2000; 88: 1389.
26. Noyan IC. Metallurgical Transactions A - Physical Metallurgy and Materials Science 1983; 14: 1907.
27. Blech IA, Levi AA. Transactions of the ASME. Journal of Applied Mechanics 1981; 48: 442.
28. Sauter AI, Nix WD. IEEE Transactions on Components, Hybrids, and Manufacturing Technology 1992; 15: 594.
29. Murakami M, Chaudhari P. Thin Solid Films 1977; 46: 109.
30. Murakami M, Kuan TS, Blech IA. Treatise on Materials Science and Technology 1982; 24: 163.
31. Noyan IC, Cohen JB. Residual Stress. New York: Springer-Verlag, 1987.
32. Hauk V, Vaessen G. Zeitschrift fur Metallkunde 1985; 76: 102.
33. Gergaud P, Labat S, Thomas O. Thin Solid Films 1998; 319: 9.
34. Welzel U, Ligot J, Lamparter P, Vermeulen AC, Mittemeijer EJ. Journal of Applied Crystallography 2005; 38: 1.
35. Labat S, Gergaud P, Thomas O, Gilles B, Marty A. Journal of Applied Physics 2000; 87: 1172.
36. Noyan IC. Metallurgical Transactions A - Physical Metallurgy and Materials Science 1983; 14: 249.
37. Nowak DE. Ph.D. Dissertation. Cornell University, Ithaca, NY, 2006
38. Hellwege KH, Hellwege AM, editors. Landolt-Bernstein Numerical data and functional relationships in science and technology. New York: Springer-Verlag, 1966.

39. Hellwege KH, Hellwege AM, editors. Landolt-Bernstein Numerical data and functional relationships in science and technology. New York: Springer-Verlag, 1969.
40. Touloukian YS, Ho CY, editors. Thermal Expansion: Non-Metallic Elements and Alloys. New York: IFI/Plenum, 1975.
41. Touloukian YS, Ho CY, editors. Thermal Expansion Metallic Elements and Alloys. New York: IFI/Plenum, 1977.
42. Freund LB. Journal of Applied Mechanics 1987; 54: 553.
43. Thompson CV. Journal of Materials Research 1993; 8: 237.
44. Nix WD. Scripta Materialia 1998; 39: 545.
45. Sullivan TD. Annual Review of Materials Science 1996; 26: 333.
46. Kim D, Nix WD, Deal MD, Plummer JD. Journal of Materials Research 2000; 15: 1709.
47. Chaudhari P. Journal of Applied Physics 1974; 45: 4339.
48. Zielinski EM, Vinci RP, Bravman JC. Journal of Applied Physics 1994; 76: 4516.
49. Thouless MD, Gupta J, Harper JME. Journal of Materials Research 1993; 8: 1845.
50. Keller RM, Baker SP, Arzt E. Acta Materialia 1999; 47: 415.
51. Huang R, Gan D, Ho PS. Journal of Applied Physics 2005; 97: 103532.
52. Thompson CV, Carel R. Materials Science and Engineering B-Solid State Materials for Advanced Technology 1995; 32: 211.
53. People R, Bean JC. Applied Physics Letters 1985; 47: 322.
54. Matthews JW, Blakeslee AE. Journal of Crystal Growth 1974; 27: 118.

55. Vodnick AM, Lawrence MD, Little B, Warden D, Shefford BP. Mater. Res. Soc. Symp. Proc.,1027E. Boston, MA: Materials Research Society, 2008. 1027.D01.01.

56. Baker SP, Keller-Flaig R-M, Shu JB. Acta Materialia 2003; 51: 3019.

57. Kuschke WM, Arzt E. Applied Physics Letters 1994; 64: 1097.

CHAPTER 4

Analysis of Plasticity and Hardening in Passivated Thin Films with Mixed Texture

Aaron M. Vodnick and Shefford P. Baker

Cornell University, Department of Materials Science and Engineering, Bard Hall, Ithaca, NY 14853

4.1 ABSTRACT

FCC thin metal films often have mixed (111)/(100) fiber texture. These orientations can have very different in-plane and out-of-plane elastic constants, leading to the possibility of very different stress states in the two texture components. In an earlier paper, an x-ray diffraction strain analysis was used to show the in-plane stresses within the (111) and (100) orientations were nearly equal, but that very large out-of-plane stresses arose in each orientation. As a result of these texture interactions, expected elastic loading trajectories could not be predicted, hindering interpretations of plastic deformation behaviors such as strain hardening and anelasticity. Thus, in the present paper a model is presented to calculate the average required changes in plastic strains and dislocation densities within each texture component during thermal cycling, and thus the amount of in-plane strain transferred between the two orientations. Due to the different active slip system geometries in the (111) vs. (100) texture components, the (111) orientation required roughly twice as many dislocations to achieve similar plastic strains. While macroscropic strain hardening rates were similar in the two orientations, (100) texture component hardened at a rate per-dislocation rate nearly twice as fast as (111) grains. Anelastic behaviors were also very

different, with dislocations in (111) grains apparently forming pile-ups leading to immediate reverse deformation on unloading from the maximum stress. The (100) orientation, in contrast, unloaded largely elastically until the stress neared zero.

4.2 INTRODUCTION

Thin films are important in many applications, but large stresses lead to challenges with performance and reliability. For instance, FCC metal films are commonly employed as electrical interconnects [1, 2], optical reflectors [3, 4], substrates for self assembled monolayers (SAMs) [5], catalysts [6], and structural elements in MicroElectroMechanical systems (MEMS) [7]. However, in each case, large stresses may cause failure through processes such as voiding, hillocking, distortion, fracture, deadhesion, or electromigration [1, 2, 8, 9].

Typical thin film stress measurements (*e.g.* substrate curvature) provide a single value for the stress in the plane of the film, σ_f. As a result, models for the mechanical behaviors of films typically assume a homogeneous equal biaxial stress state in the film plane, with zero stress in the film-normal direction ($\sigma_3 = 0$). However, annealed FCC films commonly form columnar-grained microstructures with (111)/(100) mixed fiber textures, as illustrated in Fig 4.1. For anisotropic materials, the elastic response of these two orientations is very different, both in and normal to the film plane [1, 10]. As a result, very different (triaxial) stress states may be expected to arise in the two texture components [11].

Triaxial stress states within each grain orientation arise from interactions at texture boundaries, which are separated by some distance d_{tb} in the plane of the film (Fig. 4.1). The stress field must be continuous, thus, for a uniform applied tensile strain, *e.g.* due to differential thermal expansion between the film and subsrate, strain must be transferred in the film plane from the more compliant (100) grains to the

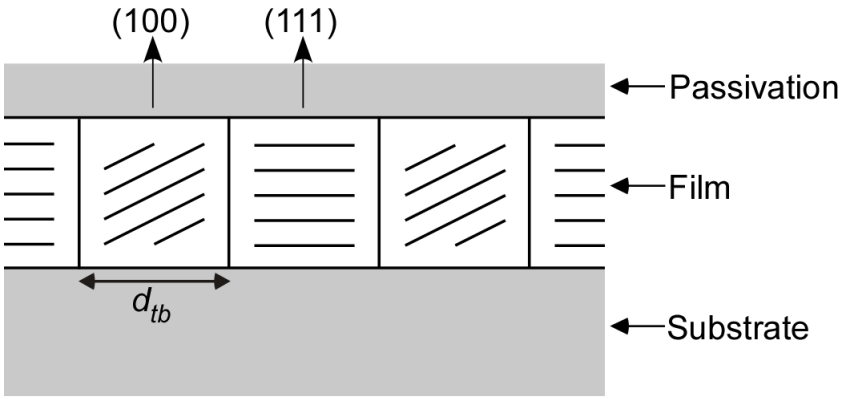

Figure 4.1: Cross section of a passivated film with mixed (111)/(100) texture. Due to large differences in the elastic constants of these orientations, relative to the film plane, significant grain interactions are expected at texture boundaries.

stiffer (111) grains at texture boundaries (by, say, boundary bowing). Additionally, unless sliding occurs along texture boundaries, the out of plane strains along such boundaries must be the same in the two texture components, leading to out-of-plane stresses. Since texture interactions are limited to regions near texture boundaries, the observed average stress states will depend on d_{tb}. Indeed, finite element simulations of Cu films with mixed (111)/(100) texure [11, 12] showed that large out-of-plane stresses arise in a typical microstructure where the grain diameter is roughly equal to the film thickness.

Several attempts have been made to investigate the average stresses in the (111) and (100) texture components in FCC films using x-ray diffraction to measure average strains in each orientation separately [13-16]. In most of these studies [13-15] it was assumed that out-of-plane stress is zero everywhere in the film. However, in previous work [16] we developed a new model to analyze x-ray data from mixed texture films in which non-zero out-of-plane stresses ($\sigma_3^{hkl} \neq 0$, where *hkl* represents the texture orientation) are allowed. The overall condition for a traction free surface is maintained by requiring that $\sum f^{hkl}\sigma_3^{hkl} = 0$, where the sum is performed over the texture components, and the f^{hkl} are the texture volume fractions [16].

We applied this analysis to data obtained from synchrotron x-ray diffraction measurements made during thermal cycles of a 500 nm thick passivated Cu film on a silicon substrate. The stress-temperature results are reproduced in Figure 4.2 [16]. Consistent with expectations based on the microstructure ($d_{\mathrm{tb}} \approx h$), the in-plane stresses were found to be nearly the same in the texture components (*i.e.* isostress) throughout the temperature cycle, and the out of plane stresses were found to be large.

While this x-ray analysis provides a better estimate of the average elastic strains and stresses in a mixed texture film, the stress states make a more refined analysis of deformation behaviors difficult. The in-plane isostress condition shown in

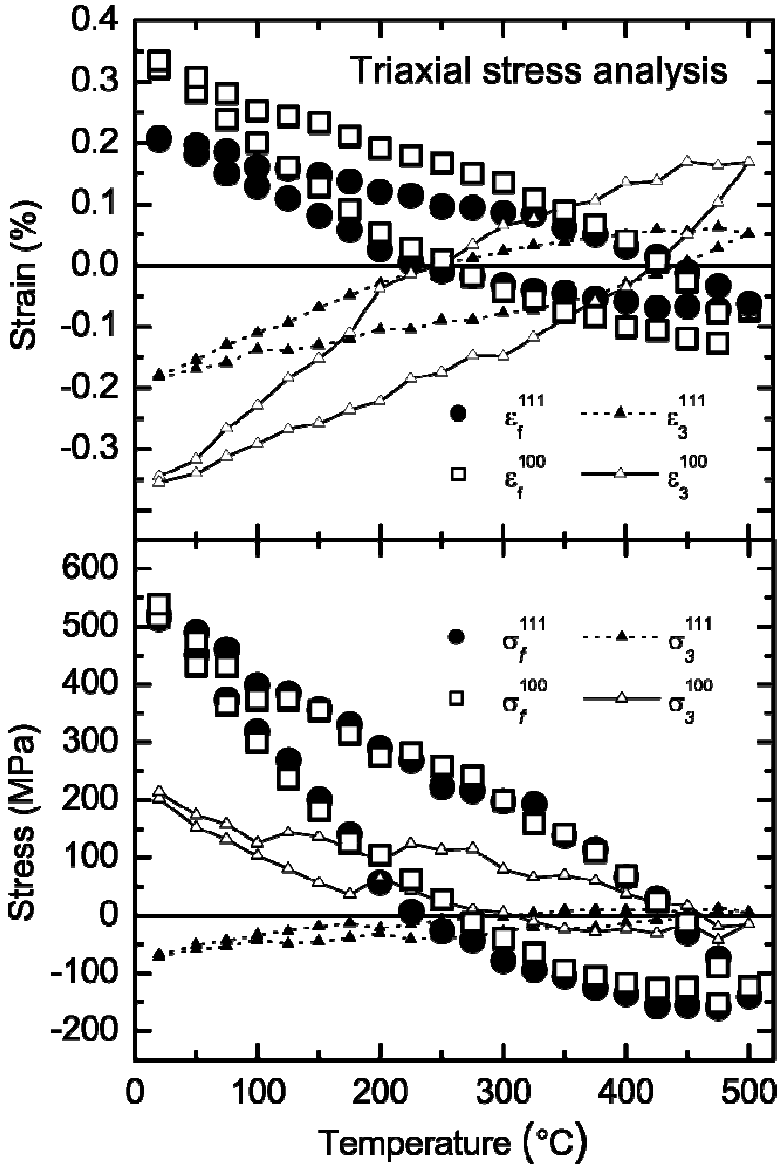

Figure 4.2: Reproduction of strain and stress *vs.* temperature data from the analysis presented in [16]. Due to grain interactions, stresses in-plane are nearly iso-stress, and significant stresses arise in the out-of-plane direction.

Fig. 4.2 requires significant strain transfer between the texture components [16]. In principle, it would be possible to estimate the average strain transfer if the grain size of each texture component were known and the deformation were purely elastic. However in general, neither is the case. Thus, neither the amount of transferred strain for a given loading state, nor the total strain in each of the texture components are known. As a result, even basic attributes of deformation are not directly obtainable from the stress-temperature data in Fig. 4.2. For example, during thermal cycling there is no regime when the data can be expected to follow the predicted thermoelastic line. Furthermore, it is not possible to accurately find the plastic strain by subtracting the elastic strain measured using x-rays from the applied strain. Clearly a model that can be used to independently determine the strain transfer, and thus the elastic and plastic strains in the texture components individually, is required if deformation behaviors such as strain hardening and anelastic deformation are to be quantified and understood.

In the present paper, we present a model that can be used to quantify changes in plastic strains and dislocation densities from x-ray measurements of the elastic strains of a passivated film with mixed texture. We use this model to interpret plastic deformation, strain hardening, and anelastic recovery in the (111) and (100) texture components of the Cu film shown in Fig. 4.2. We show that, although the hardening rate with applied strain is higher in the (111) component, as reported previously [13-15], the hardening rate per dislocation is much higher in the (100) orientation. We also find very large anelastic recovery as reported elsewhere [17] and show that it occurs in the (111) component alone. Finally, we show that peak widths do not accurately describe plastic deformation in this case.

4.3 MODEL

In this section, we develop a model that can be used to estimate the average changes in the plastic strains in each texture component of a passivated film with mixed (111)/(100) texture during thermal cycling. This model utilizes the constraint of the passivated thin film geometry and requires knowledge of the 3-D elastic strains (*e.g.* as determined from our previous analysis [16] as shown in Fig. 4.2). This model is then extended to approximate the changes in dislocation density necessary to achieve these deformations in each grain orientation.

It is important to note two assumptions which are central to the current analysis. The first is that all plastic deformation occurs due to the motion of dislocations, neglecting the possibility of plastic deformation due to diffusional flow, even at high temperatures. This approximation appears reasonable for passivated copper films, where the dominant creep mechanism has been reported to be power law dislocation glide [18, 19]. Additionally, this analysis relies upon the assumption that the average stresses and strains over a texture component are representative of stresses and strains within individual grains in the film and can be used to interpret deformation behaviors. Similar assumptions are widely used [13-15, 20, 21], and although stress distributions within individual grains may exist, and individual grains may have stress states that deviate from the average over the texture component, we will consider the average stress over each texture component to be representative and will use it to characterize the driving force for deformation processes. This model approximates how dislocation processes must scale, on average, within each texture component and allows new insights into thin film deformation behaviors.

4.3.1 Plastic Strains

During thermal cycling, the thermal strain applied to a film on a substrate due to differential thermal expansion is given by

$$\varepsilon_{Th} = \int_{T_0}^{T_f} \left(\alpha_s(T) - \alpha_f(T)\right) dT \tag{4.1}$$

where T_0 and T_f are the initial and final temperatures, and $\alpha_s(T)$ and $\alpha_f(T)$ are the temperature-dependent thermal expansion coefficients of the substrate and film, respectively.

The average total (elastic + plastic) strain in each texture component across the film due to this thermal strain is of the form

$$[\varepsilon] = \begin{bmatrix} \varepsilon_f & 0 & 0 \\ & \varepsilon_f & 0 \\ & & \varepsilon_3 \end{bmatrix} \tag{4.2}$$

where ε_f and ε_3 are the strains in and normal to the film plane, respectively. This is also the form of the average elastic strain tensor, due to the transverse isotropy of the biaxial moduli in the plane of the film in both (111) and (100) grain orientations [1, 16], as well as the plastic strain tensor, due to the symmetry of the active slip systems in each orientation (see Section 3.3.2).

Due the constraint of the substrate, the in-plane dimensions of the film and substrate must be equal. Thus, the total length of (111) and (100) oriented grains must always sum to the length of the substrate. Using this concept, it is easy to show that the average elastic and plastic strains in the plane of the film obey

$$\varepsilon_{Th} = f^{111}\left(\varepsilon_{el,f}^{111} + \varepsilon_{pl,f}^{111}\right) + f^{100}\left(\varepsilon_{el,f}^{100} + \varepsilon_{pl,f}^{100}\right), \tag{4.3}$$

where the f^{hkl} are the texture volume fractions, $\varepsilon_{el,f}^{hkl}$ are the elastic strains in the film plane which can be determined by x-ray diffraction, and $\varepsilon_{pl,f}^{hkl}$ are plastic strains in the plane of the film. Note that Eq. 4.3 does *not* require the total in-plane strain in each

texture component to simply be the applied thermal strain, *i.e.* strain transfer to maintain stress continuity across texture boundaries is allowed.

In the out-of-plane direction, a stiff passivation layer restricts deformations to keep grains of each orientation roughly the same height. Assuming this limiting case,

$$\varepsilon_{el,3}^{111} + \varepsilon_{pl,3}^{111} = \varepsilon_{el,3}^{100} + \varepsilon_{pl,3}^{100}, \tag{4.4}$$

where $\varepsilon_{el,3}^{hkl}$ and $\varepsilon_{pl,3}^{hkl}$ are the elastic and plastic strains, respectively, in the out-of-plane direction.

With the additional boundary condition that plastic strains must be volume conserving,

$$2\varepsilon_{pl,f}^{hkl} + \varepsilon_{pl,3}^{hkl} = 0, \tag{4.5}$$

Eq's 4.3-5 can be solved for the average in-plane plastic strains in each texture component, yielding

$$\varepsilon_{pl,f}^{111} = \varepsilon_{Th} - f^{111}\varepsilon_{el,f}^{111} - f^{100}\varepsilon_{el,f}^{100} - \frac{1}{2}f^{100}\left(\varepsilon_{el,3}^{100} - \varepsilon_{el,3}^{111}\right), \tag{4.6a}$$

and

$$\varepsilon_{pl,f}^{100} = \varepsilon_{Th} - f^{111}\varepsilon_{el,f}^{111} - f^{100}\varepsilon_{el,f}^{100} - \frac{1}{2}f^{111}\left(\varepsilon_{el,3}^{111} - \varepsilon_{el,3}^{100}\right), \tag{4.6b}$$

which are related to the out of plane plastic strains through Eq. 4.5.

4.3.2 Dislocation Density

The average plastic strain tensor $[\varepsilon_{pl}]$ in each texture component can be related to dislocation motion by summing the contributions to plastic strain from each slip system, i, [22]

$$\left[\varepsilon_{pl}\right] = \sum \gamma_i R_i^T \left[P_i\right] R_i, \tag{4.7}$$

where $[P_i]$ is the symmetric portion of the Schmid Tensor,

$$\left[P_i\right] = \frac{1}{2}\left(\vec{s}_i \otimes \vec{n}_i + \vec{n}_i \otimes \vec{s}_i\right), \tag{4.8}$$

R_i is the rotation from crystal to film coordinates, γ_i are the slip system activities, $\vec{s}_i$ and $\vec{n}_i$ are the unit slip directions and unit slip plane normals, respectively, and $\otimes$ denotes the dyadic product. The slip system activity is defined [22] as

$$\gamma_i = \frac{|\vec{b}|\delta A}{V}, \tag{4.9}$$

where $\vec{b}$ is the burgers vector, δA is the area on the slip plane swept out by the dislocation loop, and V is the grain volume [22].

To obtain γ_i, we model each dislocation loop as traversing a cubic grain with the grain size, d, equal to the film thickness, h. If each loop deposits dislocation line at grain boundaries and substrate/passivation interfaces, as shown in Figure 4.3, the average slip system activity can be rewritten as

$$\gamma_i \approx \frac{|\vec{b}|N_i}{d \sin \phi^{hkl}}, \tag{4.10}$$

where N_i is the number of dislocation loops on slip system i, and ϕ^{hkl} is the angle between the slip plane and film normals.

The orientations of the active slip planes in the (111) and (100) texture components are illustrated in Figure 4.4. In each texture component all active slip systems have the same values for ϕ^{hkl} and the angle between the Burgers vector and film normal, λ^{hkl} ($\phi^{111} = 70.5°$, $\lambda^{111} = 35.26°$, $\phi^{100} = 54.7°$, $\lambda^{100} = 45°$). As a result, the dislocation activity described by Equation 4.10 is the same for all slip systems in each texture component, and can be pulled out of the sum in Eq. 4.7. Since, for an equal biaxial stress, all slip systems have the same resolved shear stress (which must be true on average due to the fiber texture of the film and the constraint of the substrate), we assume for purposes of this model that a dislocation is added to all of the active slip planes in each texture component simultaneously. This allows the number of dislocation loops on each slip system, N_i, to be replaced by N/m^{hkl} where N is the total

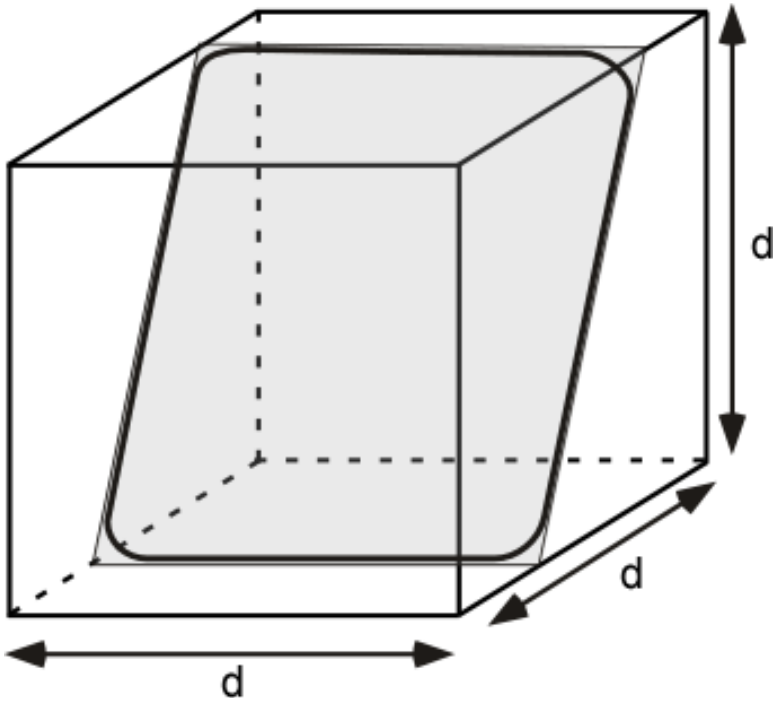

Figure 4.3: Illustration of model for dislocations in a grain. Dislocation line length is considered to be deposited at grain boundary and film/substrate and film/passivation interfaces.

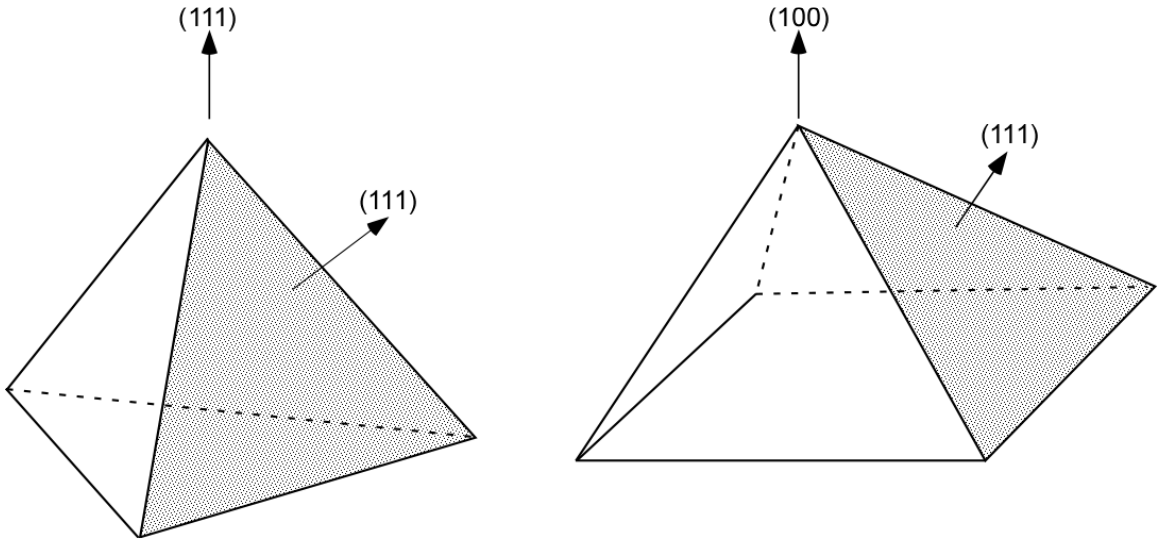

Figure 4.4: Schematic of the active slip systems in (111) and (100) oriented grains. In the (100) orientation, 8 slip systems are active, while in the (111) texture there are only 6.

number of dislocations in a grain and m^{hkl} is the total number of slip systems. It is also important to note that, for equally active slip systems, the anti-symmetric part of the Schmid Tensor sums to zero for both texture components, such that plastic deformation does not result in any crystal rotation.

Using the model that each dislocation loop traverses a cubic grain and deposits dislocation line at the film/passivation and film/substrate interfaces, and at grain boundaries (Fig. 4.3—similar to ref. [14]), the average dislocation density in a grain can be defined in terms of the total number of dislocations per grain as

$$\rho^{hkl} \approx N \frac{2d/\sin\phi^{hkl} + 2d}{d^3}. \tag{4.11}$$

Through combination of Eq.'s 4.7, 4. 9, and 4.11, the plastic strain tensor may be defined in terms of the average dislocation density in each texture component.

$$\left[\varepsilon_{pl}^{hkl}\right] \approx \rho^{hkl} \frac{1}{2m} \frac{\left|\vec{b}\right| d}{\left(1+\sin\phi^{hkl}\right)} \sum_i R_i{}^T \left[P_i\right] R_i \tag{4.12}$$

It is important to note that the amount of strain relaxation *per dislocation* is very different in the two texture components. Completing the sum on the right-hand-side of Eq. (4.12) produces a 3 × 3 diagonal matrix, P^{Tot}, with $P_{11}^{Tot} = P_{22}^{Tot} = 1/2\, P_{33}^{Tot}$. The values are $P_{11}^{Tot} = 0.8165$ for the (111) texture and $P_{11}^{Tot} = 1.633$ for the (100) texture. These P^{Tot} values account for the bulk of the ability of the active slip systems in each orientation to generate plastic stains, though there is an additional contribution on the order of 10% due to γ_i. Thus, P^{Tot} may be considered a good measure of the "*relaxation efficiency*" of slip systems in the two orientations. Of course, only mobile dislocations are captured in this model, a network of immobile dislocations may exist which is not considered in these calculations.

With Equations 4.6 and 4.12, the plastic strain in each grain orientation of a mixed texture film may be extracted from knowledge of the applied thermal strain, ε_{th}

and elastic strains obtained from x-ray measurements such as those shown in Fig. 4.2. These results allow the different strain hardening and anelastic behaviors of the (111) and (100) orientations to be investigated during thermal loading.

4.4 RESULTS

The analysis presented above was used to extract the required changes in plastic strains and dislocation densities from the x-ray measurements of elastic strains shown in Fig. 4.2. Thermal strains were determined using thermal expansion data from [23, 24] in Eq. 4.1. Because x-ray peak widths are commonly used to describe plastic deformation [13, 14, 25, 26], we report the widths of the Bragg peaks corresponding to the strain measurements in Fig. 4.1 for comparison with the model results.

4.4.1. Peak widths

Details of the strain measurements shown in Fig. 4.2 are described in ref. [16]. The measurements used two {420} type reflections for the (111) oriented grains, and two {331} type reflections for the (100) texture. The widths of these peaks are shown as a function of temperature in Figure 4.5. Both peaks measured from each texture component exhibited similar behaviors. Peak widths exhibit perfect reversibility over the temperature cycle, with no hysteresis. This behavior has been rationalized [13] as follows: Upon initial heating (unloading) the dislocation density decreases as threading dislocations (dislocations that span the thickness of the film) move back against the applied stress to reduce misfit dislocation line length (along interfaces), producing a large Bauschinger effect and a decrease in peak width with increasing temperature. Once the supply of these misfit dislocations is exhausted, threading segments move on, creating new misfit dislocations of the opposite sign and the peak width increases. The minimum in peak width is thus thought to indicate a minimum in

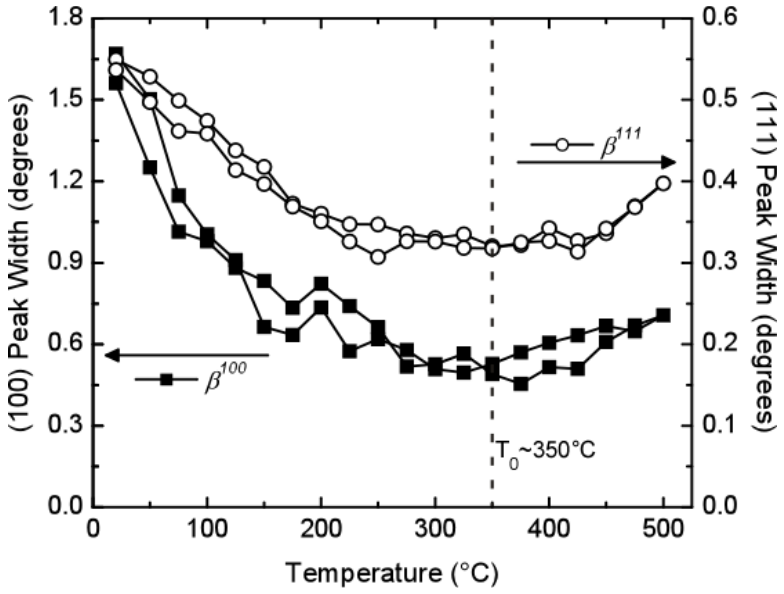

Figure 4.5: Measured diffraction peak widths *vs.* Temperature. For the (100) orientation, a {420} peak is reported, and for the (111) texture a {331} peak. Peak widths in each orientation are perfectly reversible over the temperature cycle. The minimum peak width is assumed to correspond with the minimum dislocation density, and is used to estimate T_0 in Eq. 4.2

dislocation density. On cooling, the misfits laid down during heating are first removed and then new misfits of the opposite sign are again laid down, leading to the reversibility in the peak width. However, this description cannot reconcile the perfectly reversible peak widths with the large stress hysteresis, indicating that other sources of broadening are likely significant.

4.4.2 Plastic strains

Equations 4.6 and 4.12 were used to calculate the in-plane plastic strains and dislocation densities, respectively, in each texture component using the elastic strains shown in Fig. 4.2. The temperature with the minimum peak width in Fig. 4.5 (plausibly the temperature with lowest dislocation density), 350°C, was used as T_0 in Eq. 4.1. These results are reported in Fig. 4.6, plotted *vs.* the total strain (*i.e.* in-plane elastic + plastic strain) in each orientation. Note that, in accord with Eq. 4.3, the total strain, $\varepsilon_{el,f}^{hkl} + \varepsilon_{pl,f}^{hl}$, in each texture component is *not* the thermal strain, $\varepsilon_{\mathrm{Th}}$. This can be seen in Fig. 4.6 where, at the largest tensile strain, the (100) texture component supports slightly more total in-plane strain than the (111) oriented grains. The difference, $\Delta\varepsilon = 3.4 \times 10^{-4}$, is the strain that had to be transferred between texture components (*e.g.* by bowing at grain boundaries) to maintain stress continuity at texture boundaries, as described in the introduction.

Taking a close look at the (100) texture component, on initial heating, the plastic strain in Fig. 4.6(a) remains constant with decreasing total strain, indicating purely elastic deformation in this regime. With increasing temperature (decreasing total strain), the (100) grains begin to plastically deform, with the in-plane plastic strain becoming compressive at the highest temperature (largest compressive total strain). Similarly, on initial cooling, the (100) texture component briefly exhibits purely elastic deformation before the plastic strain increases to near its initial value at

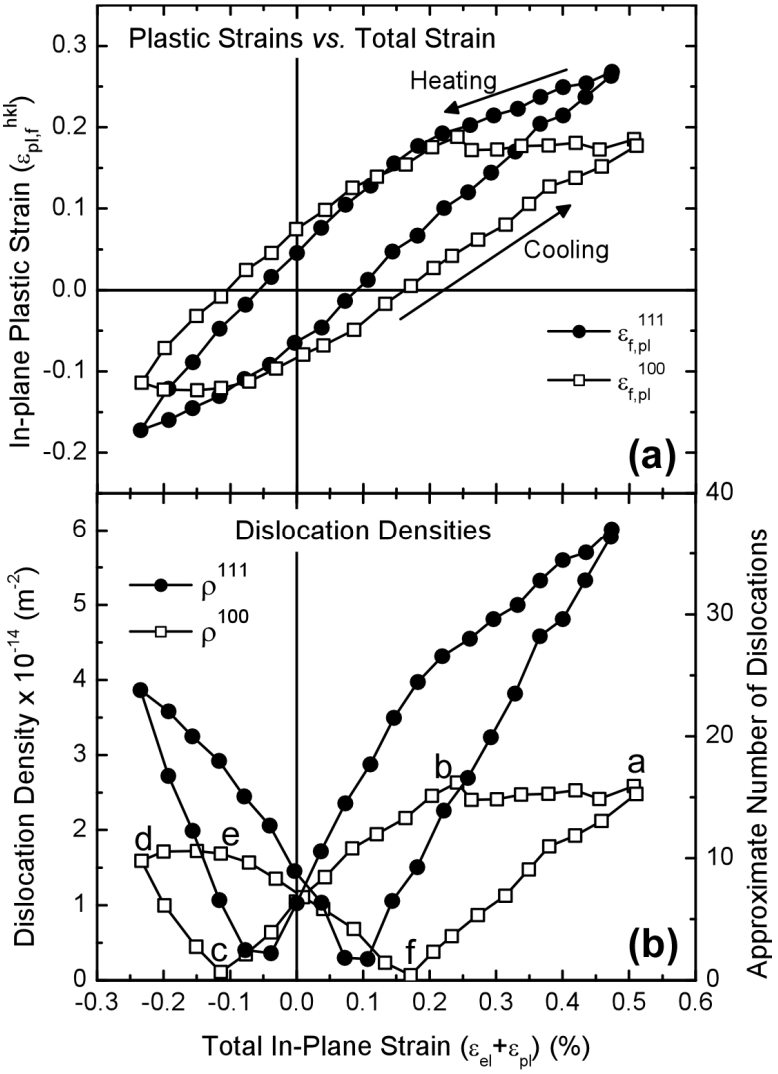

Figure 4.6: Required changes in plastic strain (a) and dislocation densities (b) in each texture component *vs.* applied strain. The hysteresis indicates that the x-ray peak width (Fig. 4.5) cannot arise from dislocation broadening alone. (This will be a pretty long description)

room temperature (largest total strain). Similar overall behavior is found in the (111) texture component except that the plastic strain changes continually during the initial portions of the heating and cooling cycles, indicating that the (111) texture component never exhibits purely elastic deformation.

4.4.3 Dislocation densities

The changes in dislocation densities required to achieve the calculated plastic strains are reported in Fig. 4.6(b). The shape of these curves are the same as those for the in-plane plastic strains (Fig. 4.6(a), except that the dislocation density is always positive. Due to the different relaxation efficiencies of the slip systems in the different orientations, the (111) texture component requires more than twice as many dislocations to achieve plastic strains similar to those in (100). In accord with the plastic strains in Fig 4.6(a) the dislocation density in the (100) orientation remains constant during initial unloading, or heating, (points *a*–*b*) again indicating elastic deformation. Plastic deformation begins at point *b* on unloading, as dislocations are removed from the film until point *c*. As the applied strain becomes more compressive, dislocations of the opposite sign are driven into the film between points *c* and *d*. Similar behavior occurs on cooling (re-loading), where the (100) texture component first deforms elastically (points *d*–*e*), dislocations are removed from the film (points *e*–*f*), and dislocations driven into the film (points *f*–*a*) on cooling back to room temperature. In the (111) texture component, dislocation behaviors are similar except that the (111) orientation never deforms purely elastically.

4.5 DISCUSSION

A previous x-ray analysis model [16] allowed us to determine the 3-D stress states in the texture components of a film having mixed texture individually (Fig. 4.2). The

current model allows us to understand how a uniform applied strain is partitioned across those texture components and how that strain is partitioned into elastic and plastic strains within each texture component (Fig. 4.6). This makes quantification of the average strain transfer between the texture components possible, and allows us to study plasticity in each texture component separately. The results indicate that in this film the strain transfer at peak load is about 7% of the applied strain, and that plastic behavior is very different in the different texture components. Most notably, only the (100) component shows elastic behavior, and then only during initial unloading. The (111) orientation shows reverse plasticity beginning immediately upon unloading. Clearly, knowledge of both the stress states and strain partitioning are needed to understand deformation and stress-driven phenomena, including failure mechanisms, in thin films with mixed texture. In the following, we briefly discuss what the model reveals about strain hardening and anelastic behaviors in the texture components, comment on the validity of using x-ray peak widths as a measure of dislocation density, and discuss the reasonableness of the analysis.

4.5.1 Strain hardening

Initial attempts to study deformation behaviors in the texture components in thin films separately [13-15] found $\sigma_f^{111} \approx 2\sigma_f^{100}$ and reported strain hardening rates as $\theta^{hkl} = \partial\sigma_f^{hkl} \big/ \partial\varepsilon_{app}^{hkl}$, where ε_{app}^{hkl} is the applied (in the present case, thermal) strain, so that $\theta^{111} \approx 2\theta^{100}$. However, these studies assumed a 2-D stress state $\left(\sigma_3^{hkl} = 0\right)$, so the reported stresses were incorrect. The 3-D stress analysis [16] showed that the in-plane stresses were nearly the same in the texture components at each applied stress (Fig. 4.2) but that the maximum shear stresses, $\tau_{\max}^{hkl}$, were correctly predicted by the 2-D analysis such that $\tau_{\max}^{111} \approx 2\tau_{\max}^{100}$. However, to correctly compare strain hardening mechanisms between the (111) and (100) texture components in a 3-D stress state,

both the resolved shear stress on the slip systems and an appropriate strain must be known. In our case, the average resolved shear stress on each slip system is given by

$$\tau_{rss}^{hkl} = \cos\phi^{hkl} \cos\lambda^{hkl} \left(\sigma_f^{hkl} - \sigma_3^{hkl} \right) \tag{4.13}$$

where ϕ and λ are as defined above.

The resolved shear stresses, calculated using Eq. 4.13 and the stresses shown in Fig. 4.2 [16], are plotted *vs.* the total strain in each texture component ($\varepsilon_{tot}^{hkl} = \varepsilon_{el,f}^{hkl} + \varepsilon_{pl,f}^{hl}$) for both of the texture components in Fig. 4.7. On cooling (loading), linear strain hardening is observed, with an overall hardening rate ($\Theta^{hkl} = \partial\tau_{rss}^{hkl} / \partial\varepsilon_{tot}^{hkl}$) slightly larger in the (111) orientation; Θ^{111} = 25.5 GPa, and Θ^{100} = 21.5 GPa. In pure metal films, strain hardening arises from dislocation-dislocation interactions [27], or dislocation blocking by grain boundaries or other interfaces [28]. Since the relaxation efficiency of slip systems is much smaller in (111) grains than in (100) grains (Section 4.3.2), about twice as many dislocations are required per unit plastic strain in the (111) texture component (Fig. 4.7). Thus, one might expect the strain hardening rates to vary by a similar factor, and it is somewhat surprising that the overall strain hardening rates are so similar.

To investigate strain hardening behaviors further, τ_{rss}^{hkl} is plotted *vs.* the change in dislocation density in Figure 4.8, which again illustrates the very different plastic deformation behaviors in the (111) and (100) texture components. The changes in dislocation density on initial unloading (heating) are consistent with the elastic deformation in the (100) texture component and the anelastic recovery of the (111) oriented grains shown in Fig. 4.6. On reloading (cooling), a linear increase of τ_{rss}^{hkl} with dislocation density is observed in both texture components. The increase in τ_{rss}^{hkl} for each added dislocation in a grain is a measure of the strain hardening efficiency *per dislocation* and is much larger in the (100) orientation, with the resolved shear

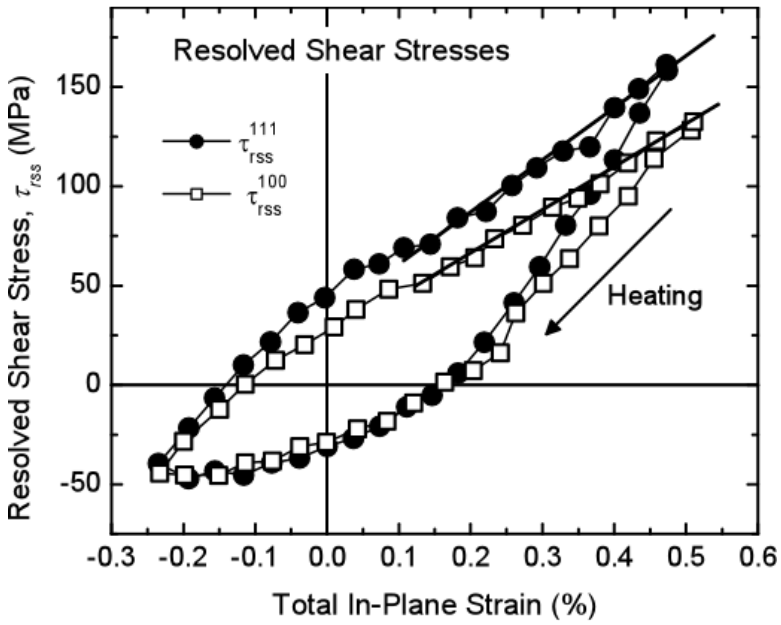

Figure 4.7: Resolved shear stress vs. applied strain for each orientation. The (111) orientation hardens only slightly faster (~20%) with respect to applied strain than the (100) texture component, though its inferior relaxation efficiency requires significantly more dislocations.

stress increasing at a rate of 4.9 MPa/dislocation, compared to 2.6 MPa/dislocation for the (111) texture. While unexpected, this result shows that, despite the fact that the dislocation density rises much more quickly in the (111)-oriented grains (Fig. 4.6), Θ^{111} is only slightly greater than Θ^{100} (Fig. 4.7), because each additional dislocation in (100) contributes significantly more to strain hardening (Fig.4.8).

The difference in the ability of dislocations in each texture component to ihibit further deformation is an interesting phenomenon that requires further study. Pant *et al*. studied the strengths of interactions between dislocations on specific slip planes in (111) and (100) films using discrete dislocation dynamics simulations [27] but did not find differences that could account for the large difference in hardening efficiencies demonstrated in Fig. 4.8. Von Blankenhagen *et al*. modeled the pile-up of dislocations at boundaries as a source of strain hardening in films [28]. In their model, dislocations originate from a repeating source and the stress is predicted to vary with the number of dislocations in a pile-up, N_{disl}, and the grain diameter, d, as $\tau \propto N_{disl}/d$. In terms of the total number of dislocations in a grain, N, this can be expressed as $\tau \propto N/N_0 d$, where N_0 is the number of sources emitting dislocations. Thus, using this pile-up model, the large disparity in hardening efficiencies in Fig. 4.8 could be explained by assuming different source densities, grain sizes, and/or twin densities in (111) and (100) grains. However, to our knowledge, data to support or refute this are not available.

While the source of the difference in hardening efficiencies is unknown, the results shown in Fig's 4.6-8 demonstrate that strain hardening is quite different in the (111) and (100) orientations. Additionally, the linear strain hardening behavior often reported [29-31] appears to hold for the texture components separately; though it must be noted that linear hardening in films is not always observed [17, 32]. The current

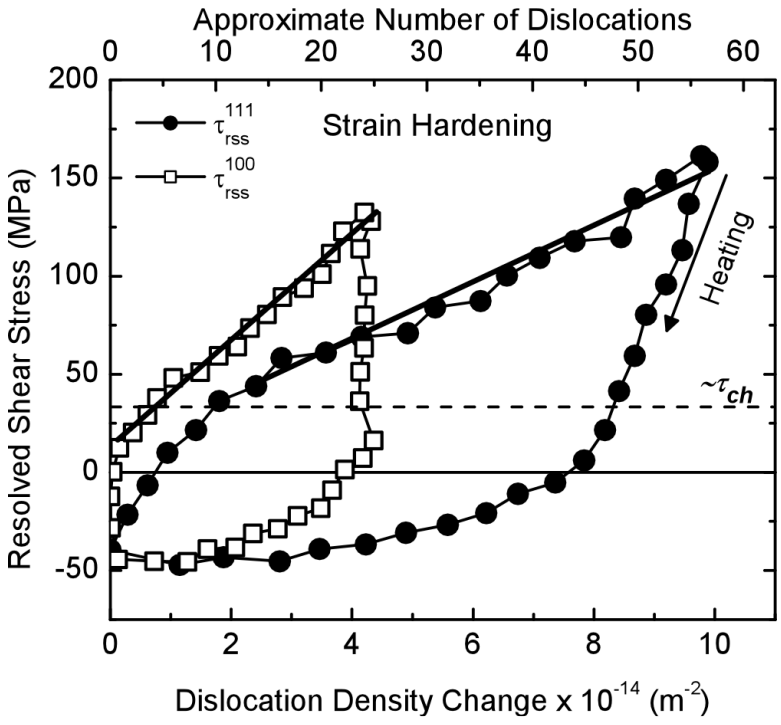

Figure 4.8: Resolved shear stress vs. change in dislocation density for each orientation. Note: Dislocation densities in this figure were calculated from plastic strains which were offset as to not go compressive. This serves only to clarify presentation, and has no impact on the important aspects (*i.e.* slopes and relative changes).

results also do not agree with the behavior expected from Taylor work-hardening ($\tau \sim \sqrt{\rho}$), the most commonly applied dislocation hardening model [33], at least over the limited strain range of these experiments.

4.5.2 Anelastic recovery

Anelastic behavior is widely observed in thin films, defined by the reverse motion of dislocations on unloading (before the negative yield stress is reached, and is attributed to the dislocation channeling behavior dictated by the constraint of the thin film geometry [17] . When a dislocation moves through a film to relax an applied stress, dislocation line length is deposited at interfaces and boundaries (Fig. 4.3). For this to occur, the work done on the dislocation by the film stress must be greater than the energy associated with the misfit dislocation deposited at the interface [1, 34]. Thus there is a critical stress for dislocation advancement, referred to as the "channeling stress," τ_{ch} [29]. A corollary of this behavior is that when the stress in the film falls below τ_{ch}, dislocations are expected to move "backwards," *increasing* the stress to recover the excess energy associated with misfit dislocations at the interfaces. Anelastic behavior is most easily observed on the heating portion of the temperature cycle (e.g. Fig. 4.2) when the data deviates from linearity before the stress crosses zero, a phenomenon also referred to as "negative yielding" [17]. However, as indicated in Fig's 4.6 and 4.8, linearity is not necessarily evidence of elastic behavior, such that the onset of anelastic behavior in either texture component cannot be identified without further analysis.

An important aspect of the current analysis is that it demonstrates that, for the current film, very different anelastic behaviors occur in the two orientations (Fig. 4.8). On unloading, dislocations in the (100) orientation do not begin to move until the resolved shear stress is well below the channeling stress (τ_{ch} = 34.5 MPa for a 500 nm

(100) oriented Cu film). This is consistent with a low dislocation density (no pileups) and some mechanism (perhaps dislocation interactions [27, 35]) that inhibits the recovery of dislocations below τ_{ch}. In contrast, dislocations in the (111) grains immediately begin to move against the applied stress. Since this occurs above the channeling stress (τ_{ch} = 36.5 MPa for this orientation), there must be some additional driving force. The additional backstress required to reverse the motion of dislocations at the largest load, $\tau_{rss}^{111} - \tau_{ch}^{111} \approx 120MPa$, suggests that dislocation pile-ups are an important feature in this texture component. This is, of course, completely consistent with the large difference in plastic relaxation efficiencies and the fact that the (111) orientation requires significantly more dislocations than the (100) texture component to achieve similar plastic deformations.

4.5.3 Comparison with peak widths

In the absence of an independent method for determining plastic strain, the widths of diffraction peaks, β, are often used as a measure of the dislocation density [25, 26]. Paired with *in-situ* x-ray strain measurements, diffraction peak widths have been used to quantitatively [13, 14] or qualitatively [21] interpret deformation behaviors in thin films. While models relating peak widths to dislocation densities vary, models to date are of the form $\beta \propto \sqrt{\rho}$ [25, 26]. However, comparing the peak widths in Fig. 4.5 to the calculated dislocation densities, Fig. 4.6, it is clear that the observed peak width variations cannot arise only from dislocations strain fields since the dislocation densities exhibit pronounced hysteresis while the peak widths are perfectly reversible. Another source of inhomogeneous strains must contribute to the observed diffraction peak widths. Grain interactions have been shown to have a significant contribution to inhomogeneous strains in the material [36, 37], and indeed, we have recently shown

that the convolution of peak broadening due to dislocations and due to grain interactions can reproduce the reversibility of the experimental peak widths in Fig. 4.5 [38].

4.5.4 Reasonableness

In this section, the reasonableness of the assumptions made in the present model is addressed.

The main deviation from the behavior of real films is that we look at average values to interpret deformation behaviors. Clearly local stress/strain deviations likely exist and these will be important to local deformation behaviors. However, we expect our use of separate average trixial stress states in the texture components to be much more accurate than the use of a single biaxial average stress to represent the entire film that has been common to date.

The assumption of a perfectly rigid passivation layer constraining grains to the same height (Eq. 4.4) is also not perfectly accurate. Even with a stiff passivation, the (111) oriented grains are expected to bow out of the film plane, while the (100) grains are expected to bow downward [16]. Errors due to this assumption should not impact the result that the (100) orientation exhibits purely elastic behavior during portions of the temperature cycle, while the (111) orientation does not. However, it will impact the calculated values of plastic strains in each orientation, altering calculated values for strain transfer and strain hardening. The influence of a relaxed out-of-plane boundary condition can be investigated by allowing the (111) grains to bow outward from the (100) grains by some constant offset in Eq. 4.4. This analysis results in even more calculated strain transfer from the (111) to (100) orientation, indicating that the amount of strain transfer calculated assuming a rigid boundary is a lower bound. Since out-of-plane distortions are small compared to the applied strain, the influence

on the calculated plastic strains, and observed strain hardening rates, are expected to be minor.

Another assumption in the current model is that dislocation loops traverse entire grains. If strong dislocation interactions occur in the grain interior, this assumption will be inaccurate. If each dislocation loop stops due to an interaction with another dislocation, the number of dislocation loops (and dislocation density) could be in error by up to a factor of 2. Currently, too little is known about the details of hardening mechanisms to address this shortcoming adequately. Regardless, the result that different anelastic and strain hardening behaviors occur in (111) *vs.* (100) oriented grains would not be impacted.

We have assumed that the texture components have, except for orientation of course, similar microstructural features. Any differences in the average grain diameters between the two orientations would thus lead to errors in the calculated dislocation densities. In order for this to be responsible for the difference in strain hardening behaviors shown in Figure 4.8, the (111) oriented grains would need to have grain diameters roughly twice those of the (100) grains. Though texture dependent grain sizes are not known, an analysis of the grain diameters (ref. [16]) showed no evidence of a bimodal distribution. A texture dependent grain size analysis of Cu films on polyimide substrates by Sonnweber-Ribic *et al.* [39] showed (111) and (100) grain sizes were roughly equal until film thicknesses of several micrometers, after which (100) grains became much larger relative to (111). This is also the case for abnormal grain growth [40] (not observed in the current film), in which (100) grains become much larger than (111). Thus, a texture-dependent grain size typically suggests large (100) grains relative to (111), which would not explain the difference in our calculated strain hardening rates. Differences in twin densities and dislocation source densities between the texture components could also affect the results, but are still unknown.

4.6 SUMMARY AND CONCLUSIONS

A simple framework based on the constrained geometry of a passivated thin metal film with mixed texture was developed to calculate the required changes in plastic strains and dislocation densities in each texture component. This model allows the plastic deformation behaviors to be investigated in a mechanistic way, instead of relying on empirical observations. With this model, it was shown that the strain hardening and anelastic behaviors of the (111) and (100) texture components were very different.

Overall, the strain hardening behaviors with total strain in the (111) and (100) orientations were similar, different by only ~20%. However, when strain hardening per dislocation is considered the (100) orientation hardened more than twice as fast as (111) grains, indicating different features may be controlling hardening in the two orientations, though the mechanism for this behavior is still unclear. Potential sources of this difference include variations in dislocation interaction strengths, dislocation source densities or twin densities.

The different slip system geometries had a significant impact on deformation behaviors within the (111) and (100) texture components, with the (111) orientation requiring more than twice as many dislocations as the (100) orientation to achieve similar plastic strains. As a result, dislocation pile-ups formed in the (111) orientation, leading to pronounced anelastic behavior immediately upon unloading from the maximum stress. In contrast, the (100) orientation deformed elastically until the stress neared zero, indicating a lack of dislocation pile-ups and perhaps even dislocation interactions to prohibit reverse deformation.

Through the present analysis, it is clear that the widths of diffraction peaks are not representative of dislocation activity in the film, as the dislocation density must exhibit significant hysteresis over the temperature cycle, while the peak widths are

perfectly reversible. Thus, some other source of heterogeneous strains, perhaps texture interactions, must be contributing to the diffraction peak widths.

4.7 ACKNOWLEDGEMENTS

Aaron Vodnick was funded in part through an Applied Materials Graduate Fellowship. This work is based upon research conducted at the Cornell High Energy Synchrotron Source (CHESS) which is supported by the National Science Foundation and the National Institutes of Health/National Institute of General Medical Sciences under NSF award DMR-0225180. Thank you to David Nowak (Intel, USA), Stephane Labat (IM2NP, UMR CNRS, Marseille, France) Olivier Thomas (IM2NP, UMR CNRS, Marseille, France), and Ken Finkelstein (CHESS, USA) for providing the CHESS data used in the analysis.

REFERENCES

1. Nix WD. Metallurgical Transactions A 1989; 20A: 2217.
2. Tu KN. Journal of Applied Physics 2003; 94: 5451.
3. Chopra KL, Paulson PD, Dutta V. Progress in Photovoltaics 2004; 12: 69.
4. Hornbeck LJ. MRS Bulletin 2001; 26: 325.
5. Love JC, Estroff LA, Kriebel JK, Nuzzo RG, Whitesides GM. Chemical Reviews 2005; 105: 1103.
6. Shin W, Matsumiya M, Izu N, Murayama N. Sensors and Actuators B-Chemical 2003; 93: 304.
7. Spearing SM. Acta Materialia 2000; 48: 179.
8. Sauter AI, Nix WD. Journal of Materials Research 1992; 7: 1133.
9. Sullivan TD. Annual Review of Materials Science 1996; 26: 333.
10. Murakami M, Chaudhari P. Thin Solid Films 1977; 46: 109.
11. Wikstrom A, Nygards M. Acta Materialia 2002; 50: 857.
12. Vinci RP, Bravman JC. Materials Reliability in Microelectronics VI. Symposium, 8-12 April 1996. San Francisco, CA, USA: Mater. Res. Soc, 1997. 481.
13. Baker SP, Kretschmann A, Arzt E. Acta Materialia 2001; 49: 2145.
14. Hommel M, Kraft O. Acta Materialia 2001; 49: 3935.
15. Vinci RP, Zielinski EM, Bravman JC. Thin Solid Films 1995; 262: 142.
16. Vodnick AM, Nowak DE, Labat S, Thomas O, Baker SP. Acta Materialia (accepted) 2009.
17. Baker SP, Keller-Flaig R-M, Shu JB. Acta Materialia 2003; 51: 3019.
18. Keller RM, Baker SP, Arzt E. Acta Materialia 1999; 47: 415.
19. Thouless MD, Rodbell KP, Cabral C. Journal of Vacuum Science & Technology a-Vacuum Surfaces and Films 1996; 14: 2454.

20. Xiang Y, Vlassak JJ. Acta Materialia 2006; 54: 5449.
21. Gruber PA, Olliges S, Arzt E, Spolenak R. Journal of Materials Research 2008; 23: 2406.
22. Kocks, Tome, Wenk. Texture and Anisotropy, 1998.
23. Hellwege KH, Hellwege AM, editors. Landolt-Bernstein Numerical data and functional relationships in science and technology. New York: Springer-Verlag, 1966.
24. Hellwege KH, Hellwege AM, editors. Landolt-Bernstein Numerical data and functional relationships in science and technology. New York: Springer-Verlag, 1969.
25. Ungar T, Borbely A. Applied Physics Letters 1996; 69: 3173.
26. Ungar T, Dragomir I, Revesz A, Borbely A. Journal of Applied Crystallography 1999; 32: 992.
27. Pant P, Schwarz KW, Baker SP. Acta Materialia 2003; 51: 3243.
28. von Blanckenhagen B, Arzt E, Gumbsch P. Acta Materialia 2004; 52: 773.
29. Nix WD. Scripta Materialia 1998; 39: 545.
30. Shen Y-L, Suresh S, He MY, Bagchi A, Kienzle O, Ruhle M, Evans AG. Journal of Materials Research 1998; 13: 1928.
31. Weihnacht V, Bruckner W. Acta Materialia 2001; 49: 2365.
32. Weiss D, Gao H, Arzt E. Acta Materialia 2001; 49: 2395.
33. Arzt E. Acta Materialia 1998; 46: 5611.
34. Freund LB. Journal of Applied Mechanics 1987; 54: 553.
35. Pant P. Ph.D. Dissertation. Cornell University, Ithaca, NY, 2004
36. Budrovic Z, Van Swygenhoven H, Derlet PM, Van Petegem S, Schmitt B. Science 2004; 304: 273.

37. Dawson PR, Boyce DE, Rogge RB. Materials Science and Engineering a-Structural Materials Properties Microstructure and Processing 2005; 399: 13.
38. Vodnick AM, Baker SP. in preparation 2009.
39. Sonnweber-Ribic P, Gruber P, Dehm G, Arzt E. Acta Materialia 2006; 54: 3863.
40. Zielinski EM, Vinci RP, Bravman JC. Journal of Applied Physics 1994; 76: 4516.

CHAPTER 5

Stress Partitioning in Passivated Copper Films with Mixed Texture and Application to Mixed Texture Stability

Aaron M. Vodnick and Shefford P. Baker

Cornell University, Department of Materials Science and Engineering, Bard Hall, Ithaca, NY 14853

5.1 ABSTRACT

The partitioning of stresses across the different texture components of mixed (111)/(100) fiber textured Cu films is investigated for a wide range of grain aspect ratios and film textures using finite element models of idealized grain structures. Average stress states within the two texture components are a strong function of grain aspect ratio, and for typical thin film grain aspect ratios near one in-plane grain interaction behaviors should be nearer to isostress than isostrain with significant out-of-plane stresses, is in agreement with a recent experimental report. An upper bound on the magnitude of out-of-plane stresses in each texture component of a mixed texture film is determined using a continuum elasticity model. Knowledge of stress partitioning is applied to discuss the thermodynamics of film texture evolution, and a mechanism is proposed to explain the stability of mixed texture films based on the distribution of grain aspect ratios and stress states in typical films.

5.2 INTRODUCTION

Many phenomena in FCC metal films are driven by large stresses that commonly arise, including deformation and failure mechanisms [1], and microstructural evolution [2]. Despite the importance of the stress state to these processes, little is known about the partitioning of stresses throughout inhomogeneous and anisotropic film microstructures.

FCC metal films tend to have highly oriented columnar grains with (111) or (100) crystal planes parallel to the film surface and random orientations in the plane of the film (fiber texture) [2]. Mixed texture films, with both (111) and (100) orientations, are very common [3].

The (111) and (100) texture components have biaxial moduli which are transversely isostropic, such that for single-textured films, an applied equal biaxial strain in the film plane (*e.g.* due to differential thermal expansion with the substrate), ε_f, results in a stress state that is also equal biaxial in the plane on the film, σ_f. The pertinent elastic constants describing a film under a biaxial strain state are the biaxial modulus, $Y^{hkl} = \sigma_f^{hkl} \big/ \varepsilon_f^{hkl}$, and the biaxial Poisson ratio, $\nu^{hkl} = \varepsilon_3^{hkl} \big/ \varepsilon_f^{hkl}$ [1, 4], where ε_3^{hkl} is the out-of-plane strain and *hkl* indicates the orientation. The (100) and (111) grain orientations often have very different elastic constants with respect to the film plane [1]. For Copper films, for instance, these elastic constants are different by a roughly factor of two; Y^{111}=261 GPa and Y^{100}=115 GPa, and $\nu^{111} = 0.73$ compared to $\nu^{100} = 1.44$. As a result of this large difference in elastic constants between the two texture components, very different stress states are expected in each texture component in mixed texture films [5-8]. Additionally, at texture boundaries significant stress interactions will arise in order to maintain stress continuity across the boundary [5, 7], leading to a redistribution of stress near the boundary.

Details of how stresses are partitioned throughout a mixed texture (111)/(100) film will influence all stress driven phenomena in mixed texture films, including plastic deformation [1], electromigration [9], voiding and hillocking [10], diffusion paths [11, 12], and texture evolution [2, 13]. Thus it is important to understand how the microstructure influences stress states. Since stress interactions between texture interactions are limited to regions near texture boundaries, stress partitioning will depend on the aspect ratio of the film thickness, t, to distance between texture boundaries, d_{tb} [7, 8]. As a result, in-plane stress partitioning will range from isostress for small distances between texture boundaries (d_{tb}<<t), to isostrain for large texture boundary distances (d_{tb}>>t). For texture boundary distances between these bounds, on the order of the film thickness (as would be expected if d_{tb} is roughly equivalent to the grain size [2]), stress partitioning is not well understood.

To understand stress distributions in real films, experimental studies have been performed to characterize the partitioning of stress amongst the different texture components using x-ray diffraction [5-7, 14]. In the majority of these studies, the potential for out-of-plane stresses was neglected [5, 6, 14] and the in-plane stress in the (111) orientation was found to be significantly larger than the stress in the (100) orientation, suggesting near isostrain behaviors. However, in a more recent investigation, in which out-of-plane stresses arising from large differences in ν^{hkl} were accounted for, a very different picture of stress partitioning was reported; nearly isostress behavior in-plane ($\sigma_f^{111} \approx \sigma_f^{100}$), with very large out-of-plane stresses [7].

Finite element models (FEM) have supported experimental investigations [8, 15, 16] by providing insights into which stress states which should be expected, but have been limited in scope. Wikstrom *et al.* [8, 16] reported detailed simulations of realistic mixed texture Cu films with a specific texture for many texture boundary spacings. A useful result of Wikstrom's analysis was the magnitude of the out-of-

plane stresses for this specific film texture. However, a description of the in-plane interactions relative to the isostrain and isostress bounds was not reported. In another FEM study, Vinci and Bravman [15] investigated an isolated (100) oriented grain with different aspect ratios in a much larger (111) oriented film, and found that grain interactions had significant impact on the stress states in the (100) grain, including significant out-of-plane stresses, though only this limiting texture was discussed. The effect of different (111) and (100) texture fractions and texture boundary spacings on the partitioning of stresses has not been reported in the literature. Due to the impact on stress driven processes, it is important to have an accurate description of stress partitioning.

Texture evolution in thin films is a stress driven phenomena directly impacted by the partitioning of stresses across a film microstructure. Film texture is driven by a competition between interfacial and strain energies in order to minimize the total energy of the film [2]. For FCC metal films the (111) orientation has the smallest interfacial energies, and is preferred for thin films. Strain energies are minimized in (100) oriented grains, which are the most compliant, such that (100) texture is preferred for thick films and at large strains. In this model, [2] an energetic boundary is predicted, in film thickness and strain space, at which a sharp transition between (111) and (100) texture is expected; mixed texture is not expected anywhere except along this boundary. Therefore, this texture model cannot explain or predict the stability of mixed texture films.

In this paper, we present the results of finite element models of idealized grain structures within passivated mixed texture Cu films. A continuum grain interaction model is also presented to describe the behavior of tall, narrow, “needle-like” grains in for films with mixed (111)/(100) fiber texture. The partitioning of stresses amongst the (111) and (100) texture components from FEM is reported, in order to understand both

in-plane and out-of-plane grain interactions at texture boundary aspect ratios between well defined limiting bounds. These modeled interactions are then compared to experimental reports of stress partitioning in mixed texture films. The effect of stress partitioning is discussed in terms of strain energy and texture evolution. We then demonstrate that the mixed texture microstructures may be stabilized by the distribution of stress in the film.

5.3 GRAIN INTERACTION MODELS

Stress partitioning in a mixed texture film is a function of the grain geometry, *i.e.* film thickness to texture boundary spacing aspect ratio, t/d_{tb}. At (111)/(100) texture boundaries, in-plane stresses in each texture component, acting normal to the boundary, must be equal in order to maintain equilibrium. However, since the film is attached to a substrate, this interaction will be limited to the regions within a few film thicknesses of (111)/(100) texture boundaries [17, 18]. Thus, for widely spaced texture boundaries ($t/d_{tb} \to 0$) in a film subjected to a uniform applied strain the average strain in each orientation would approach the applied strain, producing an average in-plane isostrain behavior and the ratio of the in-plane stresses in each orientation $\sigma_f^{111}/\sigma_f^{100}$ would be the same as the ratio of the biaxial moduli, Y^{111}/Y^{100}. At the other aspect ratio extreme, as ($t/d_{tb} \to \infty$), the limited distance between texture boundaries does not permit substantial stress redistribution, and the in-plane stresses in each orientation would be equal ($\sigma_f^{111}/\sigma_f^{100} = 1$). Only the average stress states in the (111) and (100) texture components will be considered in the present study.

Out-of-plane stresses are also expected to arise near texture boundaries due to large differences in the biaxial poisons ratio, ν^{hkl}, between the two orientations [7]. For very wide texture boundary spacings ($t/d_{tb} \to 0$) out-of-plane stresses are limited to the region near texture boundaries and will approach zero, on average, over each

grain. However, for tall, narrow, "needle-like" grains, texture boundary spacings may be small ($t/d_{tb} \to \infty$), such that non-zero out-of-plane stresses are expected to arise in each orientation. Stress partitioning for this limiting case ($t/d_{tb} \to \infty$) has not yet been described, requiring a texture interaction model to quantify the triaxial stress state at this limiting bound. For texture boundary spacings between these extreme aspect ratio bounds, finite element models are required to describe interaction behaviors.

5.3.1 Continuum model for needle-like grains

If texture boundary spacings are related to grain diameters, *d*, the limiting geometry of needle-like grains ($t/d \to \infty$) allows boundary conditions to be applied to the average stresses and strains in the grains of a mixed texture film, in order to calculate the average stress state in each texture component arising from the application of an equal biaxial strain. A thermal strain, $\varepsilon_{\mathrm{Th}}$, will be considered, which arises due to the difference in thermal expansion coefficients between the film, α_{film}, and substrate, α_{sub}; $\varepsilon_{Th} = \Delta\alpha\Delta T$, where $\Delta\alpha = \alpha_{sub} - \alpha_{film}$ and ΔT is a change in temperature.

Due to the narrow distance between texture boundaries, for needle-like grains the in-plane stresses must be continuous across texture boundaries such that in-plane isostress behavior is expected, *i.e.*

$$\sigma_f^{111} = \sigma_f^{100}. \tag{5.1}$$

In the film normal direction, since the free surface cannot support a normal traction, the average of the out-of-plane stress over the film must sum to zero, giving the boundary condition

$$\sum f^{hkl}\sigma_3^{hkl} = 0, \tag{5.2}$$

where the sum is performed over each texture component, *hkl*, and f^{hkl} is the volume fraction of each grain orientation.

Boundary conditions can also be applied to the strains in the film. For needle-like grains, the out-of-plane deformations in each grain orientation are unable to relax relative to each other (as long as grain boundary sliding is not allowed), such that grains of each orientation must remain the same height, *i.e.*

$$\varepsilon_3^{111} = \varepsilon_3^{100}. \tag{5.3}$$

Furthermore, in-plane, since the film is attached to the substrate, the dimensions of the film and substrate must be equal. In terms of strains, this requires the total in-plane strain in the film to equal the applied thermal strain, ε_{Th}. Weighting the average in-plane strains in each orientation, ε_f^{hkl}, by the texture volume fractions, provides the boundary condition

$$\varepsilon_{Th} = f^{111}\varepsilon_f^{111} + f^{100}\varepsilon_f^{100}. \tag{5.4}$$

The average in- and out-of-plane stresses withinin the (111) and (100) texture components of a mixed texture film, using Hooke's law, are defined as

$$\begin{aligned}
\sigma_f^{100} &= \varepsilon_f^{100}\left(C_{11} + C_{12}\right) + \varepsilon_3^{100}C_{12} \\
\sigma_3^{100} &= 2\varepsilon_f^{100}C_{12} + \varepsilon_3^{100}C_{11} \\
\sigma_f^{111} &= \varepsilon_f^{111}\left(C_{11}^{'} + C_{12}^{'}\right) + \varepsilon_3^{111}C_{13}^{'} \\
\sigma_3^{111} &= 2\varepsilon_f^{111}C_{13}^{'} + \varepsilon_3^{111}C_{33}^{'}
\end{aligned} \tag{5.5}$$

where C_{ij} are the single crystal elastic stiffness constants in crystal coordinates, $C_{ij}^{'}$ are the stiffness constants for the (111) texture component in film coordinates (see ref.'s [6] or [19]), and ε_3^{hkl} are the average out-of-plane strains in each orientation.

Based on Eq.'s 5.5, and boundary conditions on the stresses (Eq.'s 5.1, 5.2) and strains (Eq.'s 5.3, 5.4), the stress-thermal strain behaviors of each orientation of a mixed texture film with needle-like grains can be described. The stress boundary conditions allow Eq.'s 5.5 and the strain boundary conditions (Eq.'s 5.3, 5.4) to be expressed in matrix form $[A] = [B][\varepsilon]$,

$$\begin{bmatrix} 0 \\ 0 \\ \varepsilon_{Th} \\ 0 \end{bmatrix} = \begin{bmatrix} \left(C_{11}^{'} + C_{12}^{'}\right) & C_{13}^{'} & -\left(C_{11} + C_{12}\right) & -C_{12} \\ 2f^{111}C_{13}^{'} & f^{111}C_{33}^{'} & 2f^{100}C_{12} & f^{100}C_{11} \\ f^{111} & 0 & f^{100} & 0 \\ 0 & 1 & 0 & -1 \end{bmatrix} \begin{bmatrix} \varepsilon_f^{111} \\ \varepsilon_3^{111} \\ \varepsilon_f^{100} \\ \varepsilon_3^{100} \end{bmatrix}, \quad (5.6)$$

where the first line assures in-plane isostress behavior, the second that the average out-of-plane stress is zero, the third line that the film has the dimensions of the substrate, and the fourth line that all grains have equal heights. This equation can easily be solved for the strains, $[B]^{-1}[A] = [I][\varepsilon]$, where $[I]$ is the identity matrix. This model predicts large out-of-plane stresses, with the triaxial stress state in each texture component being a strong function of film texture.

With this analytic model for needle-like grains the limiting grain interaction behaviors for extreme aspect ratios can now be described. However, it is important to fill in the behavior of grains with moderate aspect ratios lying between these bounds—representing grain geometries in real films.

5.3.2 Finite element model

Stresses and strains in the (111) and (100) texture components of a mixed texture Cu film on a Si substrate, passivated with SiN_x, were modeled using the commercial finite element program ANSYS® (Academic Research, V. 11.0). Thermal stresses were applied to idealized grain structures, using orthotropic elastic constants as summarized in Table 5.1. These elastic properties capture the important behaviors driving texture interactions; the in-plane biaxial moduli, Y^{hkl}, and out-of-plane biaxial Poisson ratios, ν^{hkl}. While this elastic constant simplification will lose some detail compared to individual grains in a film, orthotropic elastic constants are expected to provide representative values for averages over many grains [15] as would be provided by x-ray measurements.

Table 5.1: Summary of the orthotropic elastic constants used in the FEM model for the (111) and (100) fiber textured grains, an (001) oriented Si substrate, and an isostropic SiN_x passivation layer.

	$E_{x,y}$ GPa	E_z GPa	$G_{xz,yz}$ GPa	G_{xy} GPa	$\nu_{xz,yz}$	ν_{xy}
(100) Grain	87	67	76	49	0.56	0.23
(111) Grain	129	191	41	58	0.18	0.50
Si	130.2	130.2	79.4	79.4	0.28	0.28
SiN_x	180	(isotropic)			0.3	

The simulation cell for the FE model is described in Figure 5.1. A full 3-D grain structure was used in order to get a direct, accurate, measure of the strain distributions in each texture component. A plan view illustration of the model geometry is shown in Figure 5.1 (a). A central hexagonal grain with out-of-plane crystal orientation *hkl* and width d_{tb1} is surrounded by a material with orientation *mno* and width d_{tb2}. It can be imagined how this cell may be tessellated to represent a mixed texture film as shown in Fig. 5.1(b). Boundaries between like-oriented grains (shown in the tessellation) are not included, as these are not expected to produce interactions due to the transverse isotropy of the biaxial moduli for the (100) and (111) orientations. A cross section view (Fig 5.1, (c)) shows the columnar nature of the grains, along with the substrate and passivation layer.

Volume fractions were varied from by changing the relative dimensions of the inner and outer grains, or swapping orientations, and the grain aspect ratios, *t*/*d*, reported are for texture boundary spacing corresponding to the inner grain diameter, d_{tb1},for the minority texture component. Grain aspect ratios were controlled at each texture fraction by changing the grain heights, while keeping the in-plane grain dimensions constant. Film textures modeled were f^{111} = 0.05, 0.25, 0.75, and 0.95, with the remainder (100) oriented, for grain aspect ratios of *t*/*d* = 1/5, 1/2, 1/1, 2/1, and 5/1. The passivation layer thickness was maintained at a constant fraction of the film thickness, $t_p = t_f / 100$. The substrate thickness was adjusted such that stresses approached zero far from the film/substrate interface; on average the substrate was stress free.

All interfaces were rigidly bonded. At the bottom of the substrate, a rigid, zero displacement boundary condition was applied. On the vertical edges of the simulation cell, zero normal displacement boundary conditions were applied to the faces. The

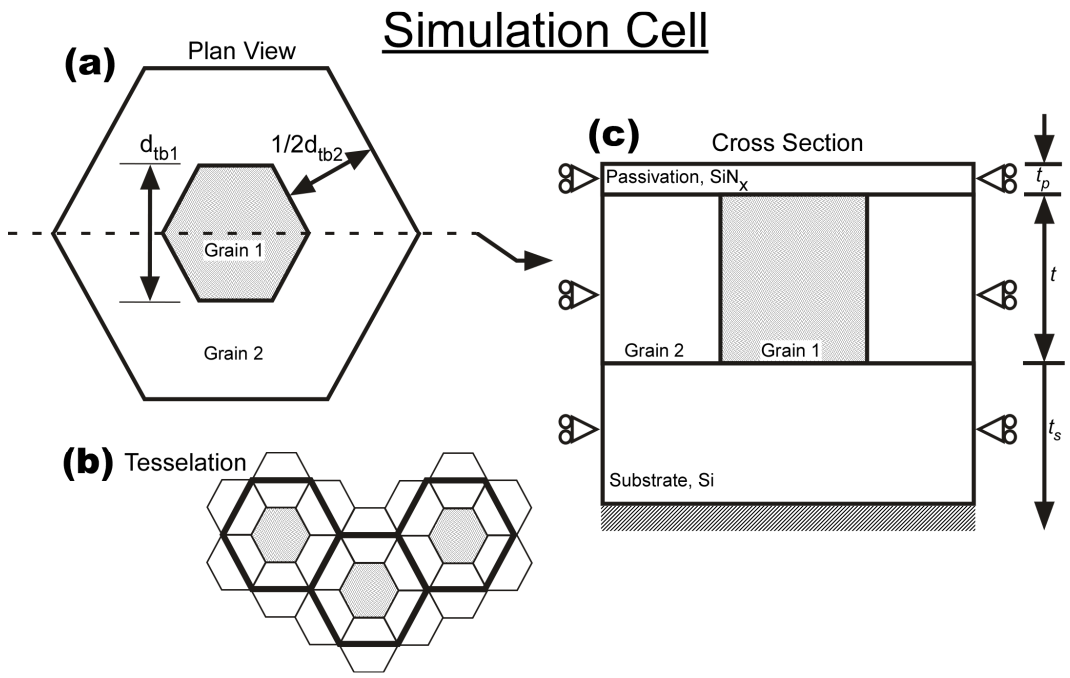

Figure 5.1: Schematic of the simulation cell used in the ANSYS models. A tessellated grain structure with two grain orientations is considered (bottom left). Since, interactions between like texture components are expected to be small in contrast with interactions at (111)/(100) texture boundaries, boundaries between like-textured grains are neglected. A plan view illustrates a grain with orientation *hkl* surrounded by material with orientation *mno*. A cross section demonstrates the columnar grains, substrate, passivation layer, and boundary conditions, as described in the text.

structure was allowed to deform vertically. Meshing was performed using ANSYS automatic meshing functions, with roughly 250,000 nodes in each simulation.

Strains were imposed through differential thermal expansion with the substrate. As an approximation, the thermal expansion coefficient of both the substrate and passivation were set to zero, and the linear thermal expansion coefficient of the grains in the film were set to α_f-α_s=1.1×10^{-5} °C^{-1} [20, 21], accurately representing the difference between Si and Cu. A temperature change $\Delta T = -180^\circ C$ was applied, though since the model is linear, results at other values of ΔT may be extrapolated.

5.4 RESULTS AND ANALYSIS

Stresses and strains reported from the present model are average values over the volume of each texture component. The resulting stress and strain tensors, in the film coordinate system, had similar forms; both were equal biaxial in the film plane, with some out-of-plane value, and off-diagonal (shear) terms that averaged to zero over each orientation.

In-plane grain interactions are summarized in Figure 5.2 where the ratio of the in-plane stresses, $\sigma_f^{111} / \sigma_f^{100}$, are shown as a function of the grain aspect ratio, *t/d*, for the different film texture fractions. The extreme grain interaction limits are isostrain ($\sigma_f^{111} / \sigma_f^{111} = Y^{111} / Y^{100} = 2.3$) at low aspect ratios, and isostress ($\sigma_f^{111} / \sigma_f^{100} = 1$) at large *t/d*, though the behaviors of all grain aspect ratios ($t/d = 1/5 \rightarrow 5/1$) and film textures ($f^{111} = 0.05 \rightarrow 0.95$) modeled fell well between these bounds. Extreme aspect ratios, beyond those realistic for most metal films, and well beyond those presently considered, are needed to achieve these limiting bounds. For typical grain aspect ratios near one, in-plane grain interactions more closely resemble isostress than isostrain behaviors. Film texture has only a small influence on the in-plane texture interactions.

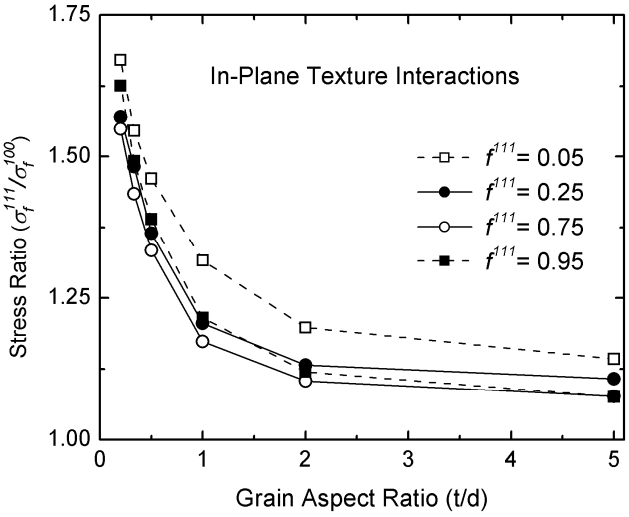

Figure 5.2: Summary of the in-plane texture interactions for various grain aspect ratios and film textures. The ratio of the average in plane stresses, $\sigma_f^{111}/\sigma_f^{100}$, in the two orientations is plotted *vs.* the grain aspect ratio. The in-plane isostrain and isostress limits would be found at stress ratios of 2.3 and 1, respectively. All grain structured modeled fell well between these limits. For typical grain aspect ratios in thin films, behaviors should be expected to fall nearer to isostress than isostrain, with a stress ratio of $\sigma_f^{111}/\sigma_f^{100} \approx 1.2$.

Out-of-plane grain interactions are summarized in Figure 5.3, which presents the ratio of the out-of-plane to in-plane stress, σ_3/σ_f , in each grain orientation for multiple grain aspect ratios as a function of film texture. For the limit of very small grain aspect ratios ($t/d \to 0$), the out-of-plane stresses are zero for every film texture.

At the other bound, for needle-like grains ($t/d \to \infty$), as described in Section 5.3.1, large out-of-plane stresses are predicted; this limit is represented by solid lines for each texture component. Due to the difference in elastic constants between the (111) and (100) orientations, the stress ratio σ_3/σ_f is always positive for the (100) texture component and always negative for the (111) orientation. For typical aspect ratios near 1, at all texture fractions, out-of-plane stresses are expected to be significant in at least one of the two orientations, with out-of-plane stresses ranging from 20-70% of the stress in the plane of the film. Especially when the (111) texture is the minority texture component, and grain aspect ratios are small, out-of-plane stresses in the (111) orientation are expected to be very large.

5.5 DISCUSSION

Stress partitioning was investigated using finite element models (FEM) in mixed (111)/(100) texture films for multiple grain aspect ratios and film texture fractions. Excellent agreement is found between the FEM results and a recent experimental report of stress partitioning based on x-ray diffraction measurements. Texture interactions have a significant impact on the strain energies within grains of different orientations and aspect ratios. It is demonstrated that distributions of strain energies within mixed texture films with broad grain size distributions may act to stabilize the mixed texture microstructure.

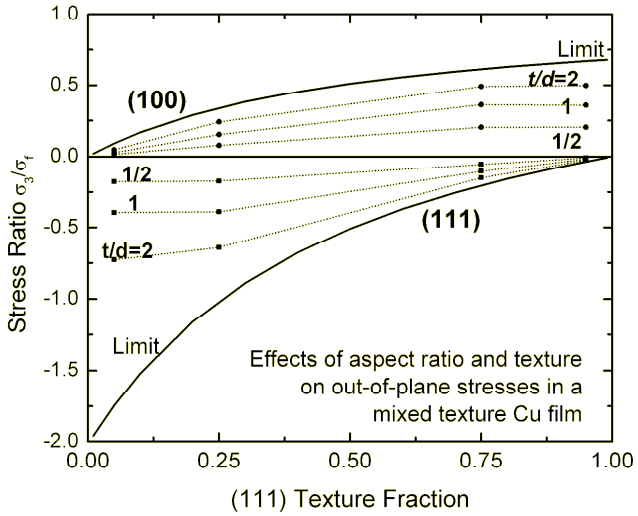

Figure 5.3: Summary of the out-of-plane texture interactions for various grain aspect ratios and film textures. For very wide grains (small aspect ratios), the out-of-plane stress is, on average, zero in each texture component. The limit on out-of-plane stresses for large aspect ratio grains, using the model from Section 2.1, is represented by solid dark lines. Due to the differences in elastic constants between the (100) and (111) texture components, the ratio of the out-of-plane to in-plane stress, σ_3/σ_f, is always positive for the (100) orientation, and negative for (111) grains. For typical grain aspect ratios near one large out-of-plane stresses, relative to the in-plane stress, can be expected in at least one of the texture components for all film textures.

5.5.1 Stress states in real films

5.5.1.1 Comparison with experimental results

In experimental reports of stress partitioning in thin films, various interaction behaviors have been suggested, from limited interactions producing nearly isostrain behavior in-plane, with $\sigma_3 = 0$ [5, 6], to interactions producing roughly isostress behavior in-plane, with significant out-of-plane stresses [7]. The present FEM results (Fig.'s 5.2-5.3) support the latter triaxial stress state reported in ref. [7], and similar stresses should be observed in typical film microstructures.

The experimentally reported out-of-plane stresses were significant fractions of the in-plane stress [7], and are in agreement with the values from the present models. Experimentally, for a film with a texture of $f^{111} = 0.75$ and $f^{100} = 0.25$ and a grain aspect ratio near one, it was found $\sigma_3^{100} / \sigma_f^{100} = 0.39$ compared to the present result of 0.36, and $\sigma_3^{111} / \sigma_f^{111} = -0.13$ compared to -0.10 from the the present model. However, the excellent agreement between the experimental results and finite element models of idealized microstructures results may be a fortunate result, as real films have small random texture fractions that will moderate the severity of texture interactions. In a more detailed FEM study of a realistic Cu film microstructure by Wikström *et al.* [8, 16], which included a considerable fraction of randomly oriented grains, the out-of-plane stresses were somewhat smaller than those predicted by the present model. Regardless of the exact values, the experimentally reported grain interactions behaviors of in-plane close to isostress and large out-of-plane stresses [7] are reasonable and similar interactions should be found for typical film microstructures.

5.5.1.2 Grain size distributions

In terms of texture interactions, another important aspect of real film microstructures is that thin films typically have broad lognormal grain size

distributions [22, 23]. Comparisons with experimental reports of stress partitioning are based on average aspect ratios and the average stress state [5-7, 14]. However, the range of grain sizes leads to a range of aspect ratios, and, in turn to a range of stress states and mechanical responses in the different grains of a film. Therefore, if a stress driven process is driven by extreme stresses in the film, the average experimental values may not capture this behavior and the distribution must be considered. Texture evolution is a stress driven phenomena for which stress partitioning and the grain size distribution have direct implications.

5.5.2 Mechanism for the stability of mixed texture films

5.5.2.1. Texture selection driving forces

Texture selection in thin films, as presented by Thompson [2], is driven by the difference in the interfacial, $\Delta\gamma$, and strain energies, ΔW_ε, between (111) and (100) oriented grains. The difference in energy density between these orientations due to interfacial energies, ΔW_i, is given by

$$\Delta W_i = \frac{2\Delta\gamma}{t} \quad , \tag{5.7}$$

where $\Delta\gamma = \gamma^{111} - \gamma^{100}$, h is the film thickness, and the factor of 2 accounts for both the film/substrate and film/passivation interfaces. This energy has the most significant contribution to the total energy for small film thicknesses, and promotes a (111) orientation, which has the smallest interfacial energy in FCC metals [2].

The interfacial energy density is in competition with the difference in the strain energy density between the two orientations, $\Delta W_\varepsilon = W^{111} - W^{100}$, to determine texture. The strain energy in each orientation is defined as $W = 1/2\,\sigma_{ij}\varepsilon_{ij}$. Typically, an isostrain grain interaction model is assumed for this value, imagining the difference in energy when a perfectly oriented (111) film is removed from the substrate and

replaced by a (100) textured film with the same strain. The large difference in biaxial moduli, Y^{hkl}, between the two orientations drives the strain energy difference, which for this isostrain model, $\Delta W_{\varepsilon\text{-}iso}$, is defined as [2]

$$\Delta W_{\varepsilon-iso} = \left(Y^{100} - Y^{111}\right)\varepsilon_{Th}{}^{2}, \tag{5.8}$$

where ε_{Th} is an applied thermal strain. Since the (100) orientation has the lowest biaxial modulus for all FCC grain orientations, and the (111) has the largest biaxial modulus, strain energy driving force gives a preferences for (100) texture

Under this thermodynamic model, a sharp transition from (111) to (100) texture is expected at the point when these driving forces balance, *i.e.*

$$\frac{2\Delta\gamma}{t} = \left(Y^{111} - Y^{100}\right)\varepsilon_{Th}{}^{2}. \tag{5.9}$$

This equilibrium boundary is commonly visualized on a "texture map" of the thermal strain *vs.* film thickness. This model predicts that for thin films with small strains, (111) texture will be stable. For thicker films and large strains, the model predicts a (100) texture. While this trend with film thickness is often observed in the literature, the sharp transition from (111) to (100) texture with increasing film thickness has rarely been reported. Instead, films with mixed (111)/(100) texture are typically observed [5, 24], with a slow transition from (111) to (100) dominated microstructures as the thickness increases. Variations of this model have been proposed, such as altering the strain energy term by allowing grains of different orientations to yield at different stresses while conceptually still applying the same strain to each orientation [24, 25]. However, these adapted models still cannot justify the stability of mixed texture films.

Knowledge of grain interaction behaviors from the present analysis requires an altered view of the strain energy driving force, ΔW_{ε}, such that the thermodynamic

equilibrium condition can no longer simply be described using an isostrain assumption (Eq. 5.9) and must be considered more generically

$$\frac{2\Delta\gamma}{t} = \Delta W_{\varepsilon}\,. \tag{5.10}$$

Insights into texture evolution can be extracted from the current finite element models, considering the distribution of texture interaction behaviors in a film and the effects on ΔW_{ε}.

5.5.2.2. Stability of mixed texture films

The strain energy driving force for texture evolution, ΔW_{ε}, calculated from the FEM results is a strong function of grain aspect ratio. Figure 5.4 presents the strain energy driving force ΔW_{ε}, normalized to the isostrain value, $\Delta W_{\varepsilon-iso}$, as a function of film texture for various grain aspect ratios. Also included for comparison are the values for different limiting grain interaction models. For the common isostrain assumption, the normalized strain energy density difference is of course equal to one. For in-plane isostress behavior, with no out-of-plane stresses, the normalized value is equal to -0.53—in this case the strain energy driving force promotes a (111) texture. The analytic grain interaction model for needle-like grains described in Sec. 5.3.1 (in-plane isostress and out-of-plane isostrain), is represented by the bold solid line. This needle-like grain model is strongly dependent on film texture, such that for strongly (100) textured films there is a large strain energy preference for further (100) grain growth, which quickly diminishes with increasing (111) texture fraction. At a texture fraction of $f^{111} = 0.75$, the strain energy driving force for this analytic model passes through zero, indicating no strain energy driving force for either texture. For strongly (111) textured films, the model for needle-like grains predicts the strain energy driving

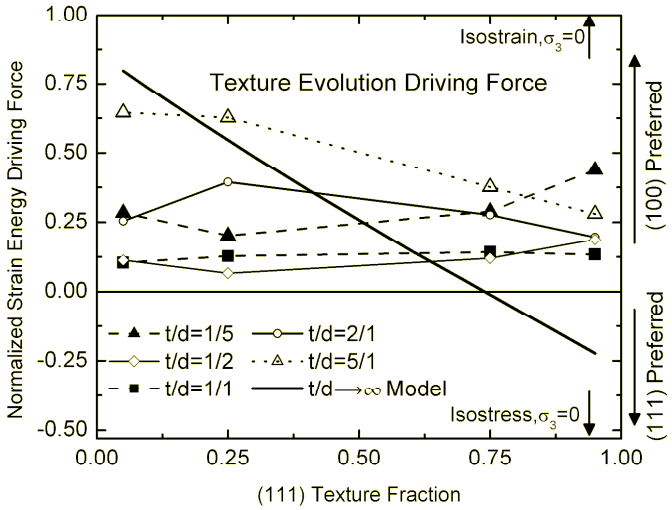

Figure 5.4: Strain energy driving forces for texture evolution, normalized to the isostrain value, for various grain aspect ratios and film texture fractions. For values greater than zero the strain energy driving force prefers (100) texture growth, and values less than zero mean strain energy is reduced with (111). Typical grain interaction bounds, assuming zero out-of-plane stress are found at 1 and -0.53 for the isostrain and isostress models, respectively. For the model presented in Section 2.1, in-plane isostress and out-of-plane isostrain, the driving force is a significant function of texture fraction. Most grain aspect ratios, other than *t:d* = 5:1, show only a small variation of driving force with film texture. However, driving forces vary widely based on grain aspect ratios.

force will promote further (111) grain growth. However, very large grain aspect ratios are required to approach this bound.

For all grain aspect ratios modeled with FEM (Fig. 5.4), the strain energy density difference is significantly reduced from the commonly assumed isostrain limit. For grains with 5/1 aspect ratios, the strain energy driving force is still a significant function of film texture. However, as aspect ratios get smaller, out-of-plane stresses decrease and texture has a diminishing effect on ΔW_ε. For aspect ratios near 1/1 or 1/2 the strain energy driving force is a minimum at all film textures, as also reported by Vinci and Bravman for an isolated (100) grain in a (111) film [15]. As aspect ratios continue to decrease, the strain energy density difference again increases such that for aspect ratios approaching zero, the isostrain bound should be approached.

The large range of strain energy density differences in grains of various aspect ratios will have a pronounced impact on the microstructural evolution of real films with broad grain size distributions. The strain energy in any grain in a film will be a function of its diameter and surrounding microstructure, and will therefore be different from the strain and thickness equilibrium conditions of the texture transition described by Eq. 5.10.

A common depiction of the conditions for texture selection in thin films [2, 25] is a plot of the equilibrium texture boundary (Eq. 5.10) on a "texture map" of the thermal strain *vs.* film thickness, demonstrating conditions which would lead to (111) or (100) texture selection. Only for a strain/thickness combination directly on the boundary (in equilibrium) would a mixed texture film be stable. However, a result of the present analysis is that, in real polycrystalline films, there is no single thermodynamic boundary for texture evolution, due to the range of interaction types described in Figures 5.2-5.4. The range of texture behaviors found in our FEM models is shown in Figure 5.5, which shows separate thermodynamic equilibrium boundaries

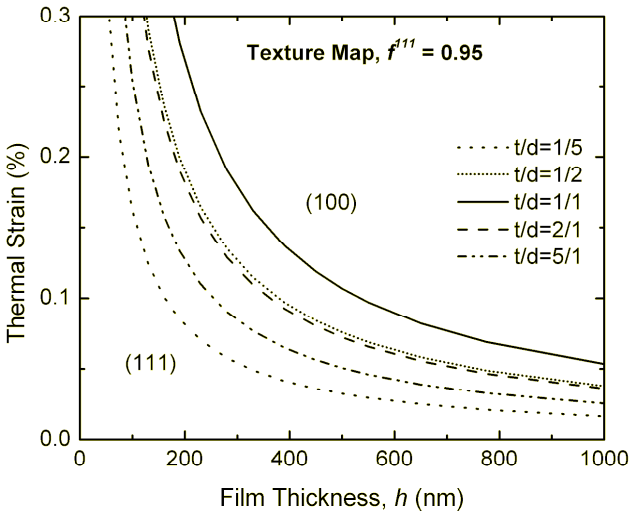

Figure 5.5: Texture map for various grain aspect ratios in a film with $f^{111} = 0.95$. The equilibrium condition for texture evolution is a strong function of aspect ratio. For strain-thickness criteria in the envelope between the different equilibrium conditions, grains with different aspect ratios will be stable with different orientations.

for texture evolution (Eq. 5.10) for various grain aspect ratios modeled in a film with a texture of $f^{111} = 0.95$, using the differences in strain energy density from Fig 5.4 (linearly extrapolated to different temperatures). The interfacial energy difference between the two orientations used for the calculations was $\Delta\gamma = 10 mJ/m^2$. (This $\Delta\gamma$ is based on the value used by Zielinksi *et al.*, ref. [26]. While this value may not be accurate, the important conclusion to be drawn from Figure 5.5 is not affected by the exact value).

As demonstrated in Figure 5.5, films with a broad grain diameter distribution should have a strain-thickness envelope in which grains with different aspect ratios are stable with different orientations. This has direct implications on texture development in thin films, as it suggests mixed texture should be expected within this range. Let us consider the thermodynamic driving forces for texture evolution in films of different thicknesses, but similar grain aspect ratio distributions and texture ($f^{111} = 0.95$). In this case, the thinnest films would have grains of all aspect ratios stable in the (111) texture. For films with increasing thickness, at the same strain, grains with aspect ratios below 1/5 should first become more stable in the (100) orientation, while all other aspect ratios remain stable in the (111) orientation. As film thicknesses continue to increase, grains with 5/1, 2/1 and 1/2 aspect ratios would progressively become stable in the (100) orientation. Finally, for the thickest films, (100) would eventually become the stable orientation for grains with 1/1 aspect ratios, and the texture transition with thickness completes. Thus, this argument predicts texture transitions should occur over a range of thickness for films with a range of grain diameters, as observed in practice [5, 24].

Following this logic, the thickness range over which texture transitions occur (e.g. see ref. [24]) should depend on the applied strain during annealing. For very large applied strains, the transition should occur over a narrow thickness regime, which

should broaden as the thermal strain is reduced. Alternately, under this mechanism the strain-thickness envelope in which mixed texture films are stable could be controlled by management of the breadth of the grain size distribution, with narrow distributions producing sharper texture transitions with increasing film thickness.

While this is an explanatory model, and not predictive, it is the first mechanistic description for the stability of mixed texture in metal films. Enhancements to this mechanism will need to incorporate second order effects, since the thermodynamic conditions will change as the microstructure evolves. Though the description in Fig. 5.5 was specifically for a film with $f^{111} = 0.95$, the range of strain energy density driving forces at all film textures (see Fig. 5.4) will produce similar predictions. While interactions in real thin film microstructures will indeed be complex, a broad range of texture interaction behaviors, producing a distribution of strain energies, will stabilize mixed texture microstructures.

5.5. SUMMARY AND CONCLUSIONS

Stress partitioning in passivated mixed texture copper films was modeled using finite element analyses of idealized grain structures. It was shown for typical grain aspect ratios found in typical films, in-plane grain interactions should be nearer to isostress behaviors than isostrain, in agreement with a recent experimental report. Additionally, for a wide range of grain aspect ratios and film textures, large out-of-plane stresses should be expected. A new grain interaction model, specific to mixed texture thin films, was also presented for the limiting case of very tall, narrow, “needle-like” grains. While this limit is not expected to be reached in most films, it provides a useful bound on possible stress partitioning in thin films.

A strong dependence of grain interactions on the grain aspect ratios was used to propose a mechanism for the stability of mixed texture film microstructures, which

has been poorly understood. Since metal films commonly have broad lognormal grain size distributions leading to a wide range of interaction behaviors, the strain energies of grains with different aspect ratios will also vary widely. With film texture driven by a competition between interfacial and strain energies, in many cases, the strain energy distribution should allow different aspect ratio grains of to be stable with different orientations, producing stable mixed texture films.

5.6. ACKNOWLEDGEMENTS

Aaron Vodnick was funded through an Applied Materials Graduate Fellowship. ANSYS access was supported in part by the Swanson Engineering Simulation Program at Cornell (Ithaca, NY USA), thanks to Rajesh Bhaskaran.

REFERENCES

1. Nix WD. Metallurgical Transactions A 1989; 20A: 2217.
2. Thompson CV. Annual Review of Materials Science 2000; 30: 159.
3. Knorr DB, Tracy DP. Materials Chemistry and Physics 1995; 41: 206.
4. Murakami M, Kuan TS, Blech IA. Treatise on Materials Science and Technology 1982; 24: 163.
5. Baker SP, Kretschmann A, Arzt E. Acta Materialia 2001; 49: 2145.
6. Vinci RP, Zielinski EM, Bravman JC. Thin Solid Films 1995; 262: 142.
7. Vodnick AM, Nowak DE, Labat S, Thomas O, Baker SP. Acta Materialia (accepted) 2009.
8. Wikstrom A, Nygards M. Acta Materialia 2002; 50: 857.
9. Tu KN. Journal of Applied Physics 2003; 94: 5451.
10. Sullivan TD. Annual Review of Materials Science 1996; 26: 333.
11. Thouless MD, Gupta J, Harper JME. Journal of Materials Research 1993; 8: 1845.
12. Thouless MD, Rodbell KP, Cabral C. Journal of Vacuum Science & Technology a-Vacuum Surfaces and Films 1996; 14: 2454.
13. Thompson CV, Carel R. Journal of the Mechanics and Physics of Solids 1996; 44: 657.
14. Hommel M, Kraft O. Acta Materialia 2001; 49: 3935.
15. Vinci RP, Bravman JC. Materials Reliability in Microelectronics VI. Symposium, 8-12 April 1996. San Francisco, CA, USA: Mater. Res. Soc, 1996. 481.
16. Gudmundson P, Wikstrom A. Microelectronic Engineering 2002; 60: 17.
17. Blech IA, Levi AA. Transactions of the ASME. Journal of Applied Mechanics 1981; 48: 442.

18. Sauter AI, Nix WD. IEEE Transactions on Components, Hybrids, and Manufacturing Technology 1992; 15: 594.
19. Bohm J, Gruber P, Spolenak R, Stierle A, Wanner A, Arzt E. Review of Scientific Instruments 2004; 75: 1110.
20. Touloukian YS, Ho CY, editors. Thermal Expansion: Non-Metallic Elements and Alloys. New York: IFI/Plenum, 1975.
21. Touloukian YS, Ho CY, editors. Thermal Expansion Metallic Elements and Alloys. New York: IFI/Plenum, 1977.
22. Thompson CV. Annual Review of Materials Science 1990; 20: 245.
23. Zielinski EM, Vinci RP, Bravman JC. Journal of Applied Physics 1994; 76: 4516.
24. Sonnweber-Ribic P, Gruber P, Dehm G, Arzt E. Acta Materialia 2006; 54: 3863.
25. Thompson CV, Carel R. Materials Science and Engineering B-Solid State Materials for Advanced Technology 1995; 32: 211.
26. Zielinski EM, Vinci RP, Bravman JC. Applied Physics Letters 1995; 67: 1078.

CHAPTER 6

Reversible X-ray Peak Broadening in Supported Metal Films with Mixed Texture during Thermal Cycling

Aaron M. Vodnick and Shefford P. Baker

Cornell University, Department of Materials Science and Engineering, Bard Hall, Ithaca, NY 14853

6.1 ABSTRACT

Thin metal films on substrates typically show hysteretic stress-strain behavior during thermal cycling. However, perfectly reversible x-ray peak widths, with no hysteresis, have been observed during thermal cycling of thin Cu films on Si substrates. While diffraction peak widths are commonly interpreted in terms of dislocation strain fields, the perfect reversibility cannot be justified based on dislocation mechanisms. It is demonstrated that interrelated broadening from sources dislocation strain fields and elastic grain interactions work in concert to eliminate hysteresis over the loading cycle.

6.2 LETTER BODY

FCC metal films on substrates have received much attention [1-6]. Such films are used in a variety of applications, and often support high stresses, leading to problems with performance and reliability [6, 7]. Grain structures of annealed FCC metal films are typically columnar and highly oriented. Depending on thickness, (111) or (100) fiber texture is predicted [8], and real films often have mixed (111)/(100) texture [2, 4, 5]. For anisotropic materials, these two texture components have very different elastic

constants with respect to the film plane. For example, in FCC materials, both of these texture components have biaxial moduli, $Y_f = \sigma_f / \varepsilon_f$, which are transversely isotropic, meaning that a uniform biaxial strain, ε_f, applied in the plane of the film results in a uniform biaxial stress, σ_f. For copper, $Y_f^{111} \big/ Y_f^{100} = 2.3$. In addition, the "biaxial Poisson ratio," $\nu_b = -\varepsilon_3 \big/ \varepsilon_f$, where ε_3 is the out-of-plane strain is quite different depending on orientation, with $\nu_b^{111} = 1.44$ and $\nu_b^{100} = 0.73$ for Cu. Thus, very different mechanical responses may be expected in each orientation [9].

Since deformation and failure mechanisms depend on local stresses, not film averaged stresses, x-ray strain measurements have been used to characterize the stresses in the (111) and (100) texture components in Cu films with mixed (111)/(100) texture separately during loading [1, 4, 5, 9]. Recent analyses have provided improved descriptions of triaxial stress states [9] (Fig. 6.1a) and plastic deformation processes (Fig. 6.1b) [10] than provided with previous methods, which assumed the out-of-plane stress was zero within each texture component [1, 4, 5]. To obtain these data (Fig. 6.1), strain measurements were performed as a function of temperature on 500 nm copper films with mixed (111)/(100) texture at the C1 hutch at the Cornell High Energy Synchrotron Source (CHESS) [9]. Films were deposited on Si substrates and were passivated with SiN_x. Four Bragg peaks were measured at each temperature. For grains having (111) orientations, {420} reflections were measured at angles from the film normal of $\psi = 26.6°$ and 63.4°. For the (100) texture component, reflections from the {331} planes at $\psi = 22.0°$ and 48.5° were used. The average grain size in the film was 550 nm.

The average stresses in each texture component [9] are shown in Fig. 6.1a. Despite large differences in the elastic constants of the (111) and (100) texture components [7], the in-plane stress components are nearly the same in the texture components, indicating significant stress interactions between texture components as

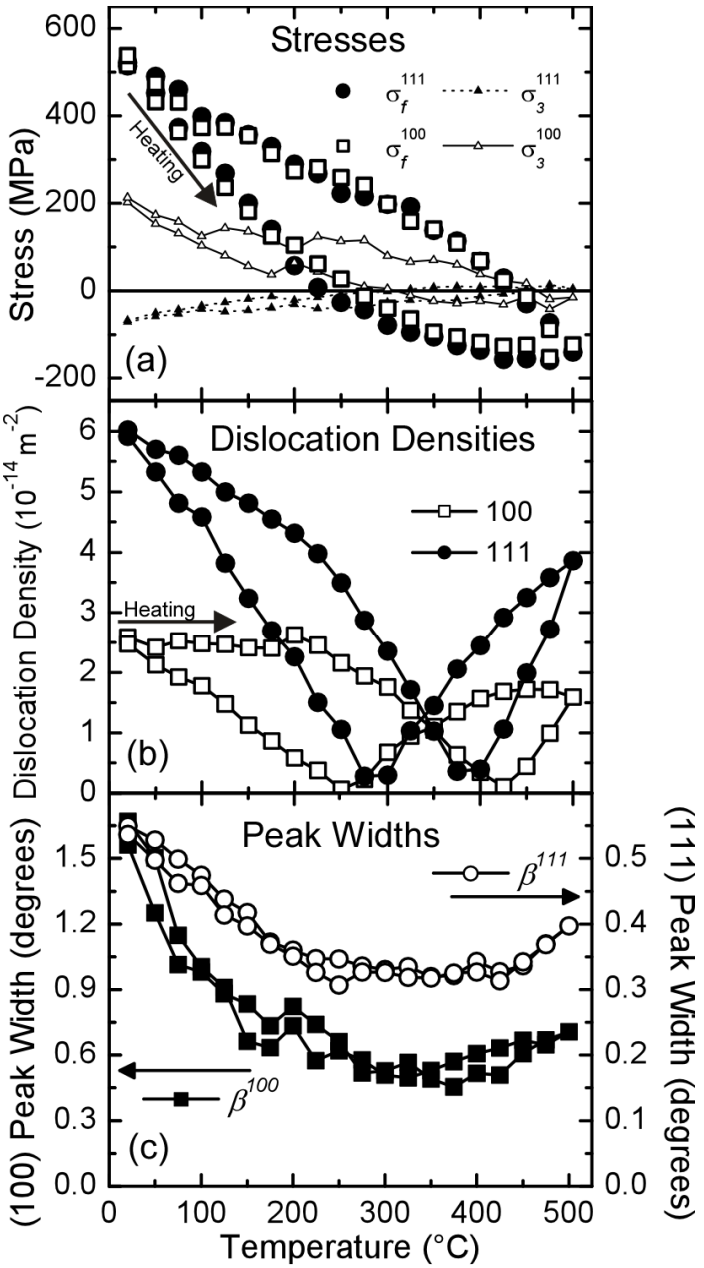

Figure 6.1: (a) The triaxial stress states in each texture component as a function of temperature, duplicated from ref.[9]. In-plane stresses are equal in each grain orientation, and large out-of-plane stresses arise. (b) The required changes in the dislocation density in each grain orientation during thermal loading. Significant hysteresis is observed. (c) Peak widths from a {331} peak from the (111) texture component, and {420} peak of the (100) texture component as a function of temperature. Perfect reversibility over the temperature cycle is observed. This behavior has been rationalized in terms of dislocation processes, though this mechanism is unable to fully account for the lack of hysteresis.

expected for a film where the spacing between texture boundaries is comparable to the film thickness. The out of plane stresses are also significant due to the large difference in the biaxial Poisson ratios.

The changes in the density of geometrically necessary dislocations associated with the stress-temperature behavior shown in Fig. 6.1a are shown in Fig. 6.1b [10]. In this model, dislocations driven into the film under an applied stress sweep across a grain and are stored at interfaces and grain boundaries. On unloading, those same dislocations come out of the film. The minimum in dislocation density is approximately set to the minimum x-ray peak width (Figure 6.1c). On heating (unloading) in Fig. 6.1b, the (100) texture component initially deforms elastically (constant ρ), until dislocations come out of the film (decreasing ρ) until the supply of stored dislocations is exhausted. The dislocations of the opposite sign are driven in (increasing ρ) up to the highest temperature. On cooling, the same behavior—elasticity, dislocations driven out of, and back into, the film—occurs as well. Similar behavior is observed in the (111) orientation, except that significant anelastic behavior is found both on initial heating and cooling—this texture never deforms purely elastically. No remnant dislocation structure is accumulated in either texture component, and this behavior is repeatable over subsequent cycles.

The widths (full width at half maximum), β, of the {420} peak measured at ψ =63.4° and {331} peak at ψ=48.5° are shown in Figure 6.1c as a function of temperature. Remarkably, the peak widths are nearly perfectly reversible across the temperature range. No corrections for instrumental broadening have been made, as this value is small relative to the experimental values, and coherence length effects are neglected as these should be small in a 500 nm film. Instead, inhomogeneous strains are expected to dominate peak broadening behaviors. Often, dislocation strain fields are treated as the primary source of strain heterogeneities [4, 5]. However, given the

significant hysteresis in the dislocation densities in each texture component (Fig. 6.1b), dislocation strain fields alone cannot account for the measured peak widths (Fig. 6.1c). Another source of strain inhomogeneity that may contribute significantly to broadening is elastic grain interactions [11, 12], as must occur at (111)/(100) texture boundaries to achieve the average isostress behavior in Fig. 6.1a [9]. These interactions occur when these boundaries bow or slide in order to maintain stress continuity across texture boundaries, producing local strain gradients which will broaden diffraction peaks.

To investigate the contribution of texture interactions to peak broadening, finite element models (FEM) of idealized grain structures in mixed texture Cu films were performed [13]. The experimental peak widths at room temperature, Figure 6.1c, correspond to heterogeneous strains ($\Delta\varepsilon = 1/4\beta\cot\theta$ [14]) of about $\Delta\varepsilon = 2 \times 10^{-3}$ in the (100) texture and $\Delta\varepsilon = 1 \times 10^{-3}$ in the (111) grain orientation. In comparison, at a similar stress the strain heterogeneity due to grain interactions, approximated as the standard deviation of strains from FEM for grains with thickness to grain diameter aspect ratios of $t/d = 1$, is roughly one fourth the experimental value ($\Delta\varepsilon = 5.5 \times 10^{-4}$ in (100), 2.3×10^{-4} in (111)). Additionally, grain interactions depend on the grain aspect ratio [13], such that the mean strain in any grain in a film will depend on its diameter. For grain aspect ratios from $t/d = 1/2 \rightarrow 2/1$, the variation of the average strains is roughly of the same scale as the standard deviation within an individual grain, and this intragranular term will also produce broadening. Thus, to first order, the total strain heterogeneity due to elastic grain interactions in a film with a distribution of grain sizes can account for approximately 50% of the experimental peak width at room temperature.

During thermal cycling, deformations remain small such that grain interactions remain nearly linear, such that the ratios of the strain standard deviation to the mean

remain roughly constant in each orientation at each temperature. Therefore, relative changes in peak-width due to elastic grain interactions, β_{el}, throughout the thermal cycle can be described as the absolute value of the ratio of the current stress (Fig. 6.1a) normalized by the maximum stress at room temperature

$$\beta_{el} \propto \left| \frac{\sigma}{\sigma_{\max}} \right|. \tag{6.1}$$

This is an approximation, as it implies when the mean stress is zero the standard deviation is also zero, though some range of stress may exist even when the average is zero. Without a model to estimate this baseline, it will be assumed small relative to the maximum.

With Eq. 6.1, broadening due to texture interactions can be contrasted with the broadening contribution from dislocations. Though models for dislocation peak broadening are widespread [15-17], these are not appropriate for quantitative analysis of thin films for two reasons: (1) Highly polarized dislocation structures on specific slip systems in films require the use of so called "Dislocation Contrast Factors" [15, 16], which have not yet been addressed in the literature for Cu films. (2) Significant dislocation line length in passivated thin films is located at the film/substrate and film/passivation interfaces [7]. Therefore, much of the strain field associated with interfacial dislocations will exist outside the sampled volume.

Although a quantitative analysis for dislocation peak broadening, β_{dis}, in textured films does not yet exist, models relating dislocation density to peak width to date are of the form $\beta_{dis} = C\sqrt{\rho}$ [15-17], where C is a constant that includes materials, dislocation, and reflection dependent parameters. Thus, relative changes in dislocation peak broadening can be described, normalized to the maximum value, as

$$\beta_{dis} \propto \left(\frac{\rho}{\rho_{\max}} \right)^{1/2}. \tag{6.2}$$

Since only the average mobile dislocation density is represented in Fig. 6.1b, there is likely a remnant dislocation structure even when the calculated average passes through zero. Without knowledge of this minimum density, it will be assumed to be small relative to the maximum.

Using stress and dislocation density data from Fig.'s 6.1a,b, [9, 10] the normalized peak width contributions from both elastic grain interactions and dislocation strain fields (Eq.'s 6.1-2) are shown in Figure 6.2 for each texture component. During the initial portion of the heating cycle, as the (100) texture deforms elastically, the dislocation contribution to broadening stays flat, while the stress interaction contribution diminishes rapidly. In this same temperature range on cooling, the film deforms plastically, and broadening contributions from both stress interaction and dislocations increase at similar rates. A comparable behavior is observed in the (111) data, which exhibits anelastic deformation on initial heating and cooling. The key behavior here is that the two sources of inhomogeneous strains are not independent, such that when one varies rapidly the other varies slowly. That is, during elastic deformation the stress varies the most rapidly, while the dislocation density remains constant. At the other extreme, when the dislocation density changes rapidly to relax stress, the stress changes slowly.

As a result of these interrelated sources of inhomogeneous strains an interesting phenomena is produced; the composite effect on the peak width eliminates hysteresis over the temperature cycle. Since the elastic interaction broadening term is roughly 50% of the total strain heterogeneity at the largest load, the total effect of the two broadening contributions can be approximated by superimposing the strain fields. The resulting peak width, β_{tot}, normalized to one, can be written as $\beta_{tot} = 1/2\left(\beta_{el} + \beta_{dis}\right)$. The composite peak width is shown in comparison to the

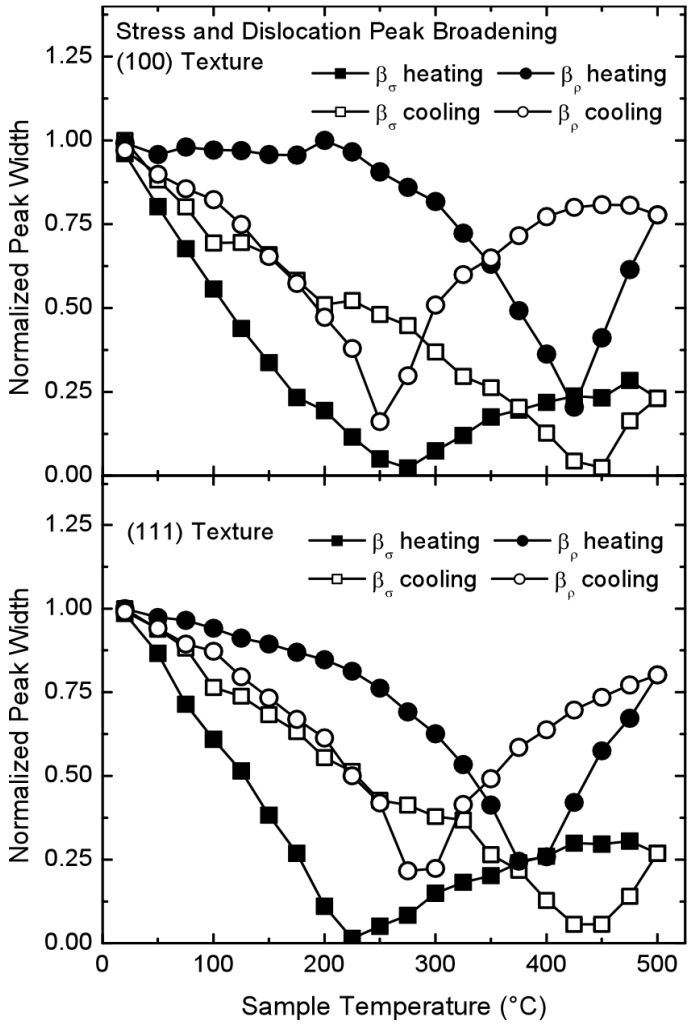

Figure 6.2: The expected contributions to broadening from elastic grain interactions and dislocation strain fields during the temperature cycle for the (111) and (100) grain orientations. Each contribution to peak broadening exhibits significant hysteresis, but are interrelated such that when one changes rapidly, the other varies slowly.

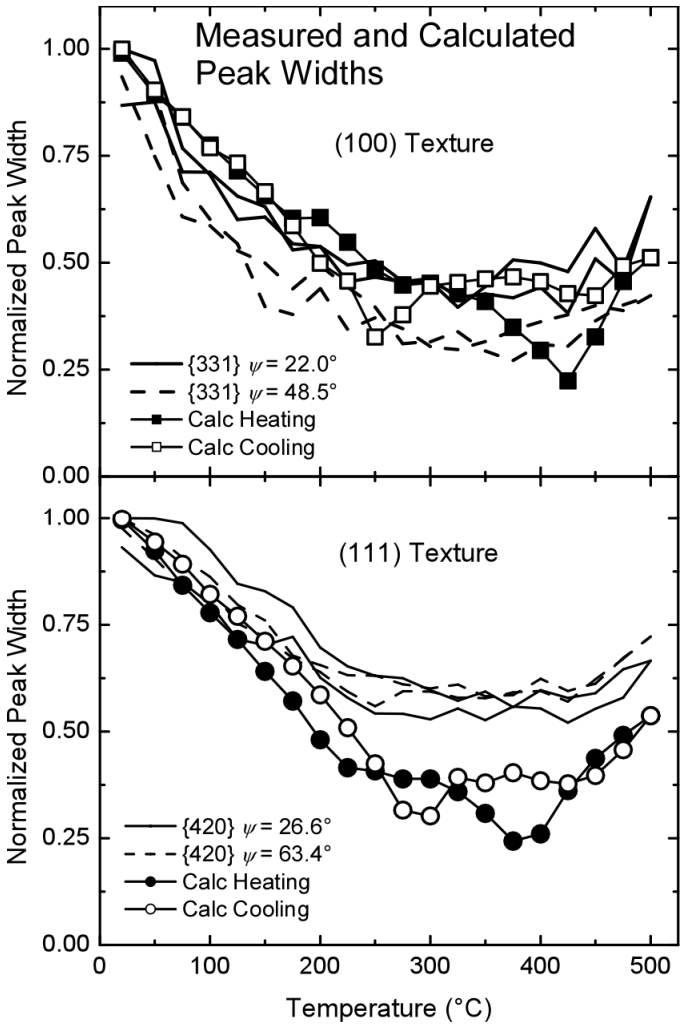

Figure 6.3: The composite peak widths expected from the combination of elastic grain interactions and dislocation strain fields, for the (111) and (100) texture components, plotted along with the normalized experimental peak widths, as a function of temperature. The reversibility of the experimental peak widths are well represented over the entire loading range the by the combination of inhomogeneous strains from grain interaction and dislocations.

normalized experimental values in Figure 6.3. The reversibility of the experimental values is well reproduced over the majority of the temperature cycle by the combination of stress interaction and dislocation broadening contributions.

Reports describing reversible peak broadening in nanocrystalline Ni films (26 nm grain size) under uniaxial loading have been presented by Budrovic *et al.* [11, 18]. In these papers, Budrovic *et al.* reported peak widths which increased rapidly on loading and were completely recoverable after the load was released, indicating deformation occurred without accumulation of a remnant dislocation field attributed to dislocation emission and absorption from grain boundaries. This resulted in recoverable peak widths which exhibited significant hysteresis with applied strain, but little hysteresis with applied stress [11, 18]. A different phenomenon is reported in the present analysis, producing reversible peak widths with no hysteresis when plotted *vs.* the applied strain (Fig. 6.1c). Similar to Budrovic *et al.*, the present peak width reversibility requires a remnant dislocation structure not form over the temperature cycle, likely due to the reversible emission and recovery of dislocations [19]. The present phenomenon is due to an intricate balance and interrelationship between the inhomogeneous strains from dislocations and texture interactions.

Understanding the factors comprising diffraction peaks from thin films will inform future investigations of deformation behaviors with *in-situ* diffraction measurements. For instance, knowledge of the expected strain distributions due to grain interactions allows this contribution to be subtracted from experimental peak width in order to isolate plastic deformation behaviors [12]. The ability of the present analysis to mimic the reversibility of the experimental peak widths also lends confidence to the method used to calculate the average changes in dislocation densities in ref. [10] (*i.e.* Fig 6.2b). Current results will also be of benefit in investigations in which the widths of diffraction peaks are used to examine dislocation densities [4, 5],

support proposed deformation models [5], or interpret deformation processes [20] in textured films.

6.3ACKNOWLEDGEMENTS

This work is based upon research conducted at the Cornell High Energy Synchrotron Source (CHESS) which is supported by the National Science Foundation and the National Institutes of Health/National Institute of General Medical Sciences under NSF award DMR-0225180. Aaron Vodnick was funded in part by an Applied Materials graduate fellowship.

REFERENCES

1. Vinci RP, Zielinski EM, Bravman JC. Thin Solid Films 1995; 262: 142.
2. Knorr DB, Tracy DP. Materials Chemistry and Physics 1995; 41: 206.
3. Keller R, Baker SP, Arzt E. Journal of Materials Research 1998; 13: 1307.
4. Baker SP, Kretschmann A, Arzt E. Acta Materialia 2001; 49: 2145.
5. Hommel M, Kraft O. Acta Materialia 2001; 49: 3935.
6. Thouless MD. Annual Review of Materials Science 1995; 25: 69.
7. Nix WD. Metallurgical Transactions A 1989; 20A: 2217.
8. Thompson CV. Annual Review of Materials Science 2000; 30: 159.
9. Vodnick AM, Nowak DE, Labat S, Thomas O, Baker SP. Acta Materialia (accepted) 2009.
10. Vodnick AM, Baker SP. in preparation 2009.
11. Budrovic Z, Van Swygenhoven H, Derlet PM, Van Petegem S, Schmitt B. Science 2004; 304: 273.
12. Dawson PR, Boyce DE, Rogge RB. Materials Science and Engineering a-Structural Materials Properties Microstructure and Processing 2005; 399: 13.
13. Vodnick AM, Baker SP. in preparation 2009.
14. Megaw HD, Stokes AR. Journal of the Institute of Metals 1945; 71: 279.
15. Ungar T, Dragomir I, Revesz A, Borbely A. Journal of Applied Crystallography 1999; 32: 992.
16. Ungar T, Tichy G. Physica Status Solidi a-Applied Research 1999; 171: 425.
17. Scardi P, Leoni M, Delhez R. Journal of Applied Crystallography 2004; 37: 381.
18. Budrovic Z, Van Petegem S, Derlet PM, Schmitt B, Van Swygenhoven H, Schafler E, Zehetbauer M. Applied Physics Letters 2005; 86.

19. Baker SP, Keller-Flaig R-M, Shu JB. Acta Materialia 2003; 51: 3019.

20. Gruber PA, Olliges S, Arzt E, Spolenak R. Journal of Materials Research 2008; 23: 2406.

CHAPTER 7

This chapter contains preliminary research as an example of a class of problems that can be addressed using the background in x-ray strain measurements and stress partitioning in FCC metal films with mixed texture developed in chapters 3-6 of this thesis. *In-situ* x-ray strain measurements were performed in the (111) and (100) texture components of a silver film during texture evolution, providing detailed knowledge of the strain energies driving texture selection throughout recrystallization. Future work similar to this will aid in the development of improved models for microstructural evolution in thin films, and of tailored microstructures allowing enhanced device reliability.

Synchrotron Characterization of Texture and Stress Evolution in Ag Films

Aaron Vodnick[1], Michael Lawrence[1], Bethany Little[2], Derek Worden[2], and Shefford Baker[1]

[1]*Department of Materials Science and Engineering, Cornell University, Ithaca, NY, 14853*

[2]*Department of Physics, Houghton College, Houghton, NY, 14744*

7.1 ABSTRACT

Real-time in-situ synchrotron x-ray diffraction measurements were performed at the Cornell High Energy Synchrotron Source to characterize both the texture evolution and stresses within the individual texture components of Ag films during texture transformations. As deposited films had a nearly perfect (111) fiber texture. During

isothermal anneals, stress and texture were characterized in real time as the texture evolved into a strong (001) fiber. An Avrami analysis of the evolving texture fractions yielded very different activation energies for films on different barrier layers, suggesting that different governing mechanisms were responsible for secondary grain growth. The strains were used to test a common model for texture prediction that assumes the same strain within each texture component. It was found that secondary (001) grains were able to grow primarily strain free. Selection for this strain energy minimizing orientation occurred during the nucleation process during which texture interactions play an important role. By using real time x-ray diffraction measurements, we are able to show that driving forces for texture transformations in metal films may not be as simple previously described.

7.2 INTRODUCTION

The mechanical behavior of metal films is highly dependent on their microstructures. FCC metal films tend to have highly oriented columnar grains with either the <111> or <001> crystal orientation normal to the film plane. It is widely accepted that these two orientations arise due to a minimization of interface or strain energy, respectively [1]. The preferred orientation will minimize the total energy of the film, which depends on the relative contributions of the surface ($W_\gamma = \Delta\gamma / h$) and strain energies ($W_\varepsilon = \Delta Y \varepsilon^2$), where $\Delta\gamma$ and ΔY are the difference in interface energies and biaxial moduli between (111) and (001) orientations, respectively, h is the film thickness, and ε is the applied strain. Improvements to this model have been made by considering the different yield stresses [2, 3] for the different texture components, and the effect of changing strain due to grain growth [3], though the latter has been utilized much less. These energy models for texture selection predict a critical thickness at which a sharp texture transition occurs, but in real films the texture transition often occurs over a

wide thickness range (e.g. [2]). The mixed texture observed in many films is also not explained using this model. Mixed texture may be explained by interactions between anisotropic texture components, which may significantly affect the strain energies in both orientations. For instance, recent work showed the strain energies within the (111) and (001) grain orientations in a 500 nm annealed copper film with mixed texture were equal as a result of significant grain interactions [4]. Improvement to our understanding of film microstructures therefore relies in part on bettering our knowledge of the stress states as a driving force for recrystallization.

Real-time *in-situ* synchrotron x-ray diffraction offers powerful tools to analyze this texture development model. Specifically, high intensity x-rays can be used to probe both the kinetics of texture evolution, and lattice strains. The relative amounts of the (111) and (001) texture components may be characterized by monitoring the intensity of peaks corresponding to these orientations [5]. Additionally, synchrotron x-rays allow for measurement of the stresses within the (111) and (001) texture components individually, thus providing the strain energy driving force for recrystallization [4, 6, 7].

7.3 EXPERIMENT

Silver films were deposited at room temperature by magnetron sputtering in a deposition chamber with a base pressure $< 7 \times 10^{-9}$ Torr onto <001> Si wafers with either a 50 nm PECVD SiN_x or 500nm SiO_x barrier layer. The Argon pressure was 8 mTorr and the power was 100 W DC, which resulted in a deposition rate of 50 nm/min. At the top and bottom of the Ag film a 20 nm Ti adhesion layer was included, deposited at 13 mTorr and 100 W DC. Without breaking vacuum, films were passivated with SiN_x deposited to 50 nm by r.f. reactive sputtering in 3 mTorr each of Ar and N_2. All depositions were performed at room temperature. The Ag films on the

SiO_x and SiN_x barriers had thicknesses of 1200 nm and 1300 nm, respectively. Films were removed from vacuum and cleaved into many separate samples before subsequent characterization. Transmission electron microscopy images of the SiO_x barrier showed significant surface roughness on the order of tens of nanometers.

Real-time *in-situ* texture and strain evolution characterizations were performed in the G2 hutch at the Cornell High Energy Synchrotron Source (CHESS). The station is equipped with a six-circle kappa diffractometer, an Ordela 1100x gas proportional detector (Ordela, Oakridge, TN) and sample oven allowing controlled annealing atmospheres [8]. All measurements were performed in the vertical scattering plane at a beam energy of 9.8 keV. Isothermal recrystallization experiments were performed at temperatures between 117°C and 160°C, with a ramp rate to the final temperature of 15°C/min. The annealing atmospheres for the two samples were different; the 1200 nm film on SiO_x was annealed at atmospheric pressure in a reducing gas of N_2 with 900 ppm CO to reduce oxygen content, while the 1300 nm film on SiN_x was annealed in high vacuum with a base pressure of 2×10^{-7} Torr.

In order to characterize texture, the intensities of the (222) and (004) reflections with scattering vectors normal to the film plane were monitored during the recrystallization. After correcting for scattering geometry, structure factor, monitor counts, and the Lorentz factor, the volume fractions of the (111) and (001) texture components can be roughly estimated from the areas, A^{hkl}, of the peaks (*i.e.* $f^{001} = A^{004} \big/ A^{004} + A^{222}$). Corrections for multiplicity need not be made, and since measurements were in the vertical scattering plane the polarization factor for synchrotron radiation is unity. The time required to capture both these peaks when characterizing texture in real time was about 40 seconds.

The stress states within the (111) and (001) texture components were also characterized as a function of time using the $sin^2\psi$ method [6, 7, 9]. The (222) and (004) out-of-plane reflections were used along with (240) peaks measured at angles from the film normal of $\psi = 63.4$ and $\psi = 39.3$ for the (001) and (111) texture components, respectively. If it is assumed the out-of-plane stress is zero, this allows the biaxial stress and unstrained lattice parameters to be calculated for both orientations separately [4, 6]. The time required to capture these four peaks was just over 2 minutes.

7.4 RESULTS AND ANALYSIS

7.4.1 Recrystallization Kinetics

Prior to recrystallization, both as-deposited films showed very strong (111) fiber textures with very small volume fractions of (001) oriented grains, $f^{001} < 0.05\%$. As recrystallization progressed during the isothermal holds, (001) oriented grains develop until about 99% of the film became (001) textured. Plotting f^{001} as a function of time (Figure 7.1) we see the recrystallization follows a conventional s-shaped nucleation and growth curve, which can be modeled using the Avrami equation, $f^{001} = 1 - \exp\left(-kt^n\right)$, where k primarily includes kinetic information of the boundary velocity and n contains information on growth geometry ($n = 2$ expected for 2D growth in a thin film) or if there is nucleation ($n = 3$ for 2D growth with constant nucleation) [10]. Both films showed similar behaviors with the 1300 nm film on SiN_x recrystallizing at a slightly lower temperature.

An Arrhenius plot of the Avrami coefficients k found for texture transformations at different temperatures (Fig. 7.2) yields straight lines with slopes

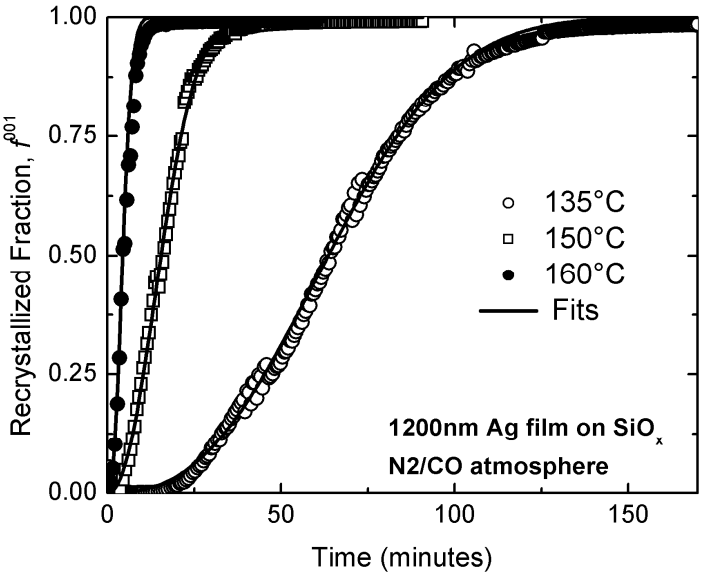

Figure 7.1. Recrystallized (001) volume fraction *vs.* time during isothermal anneals for 1200 nm Ag film on SiO_x barrier layer. Black lines are fits of the Avrami equation to the data.

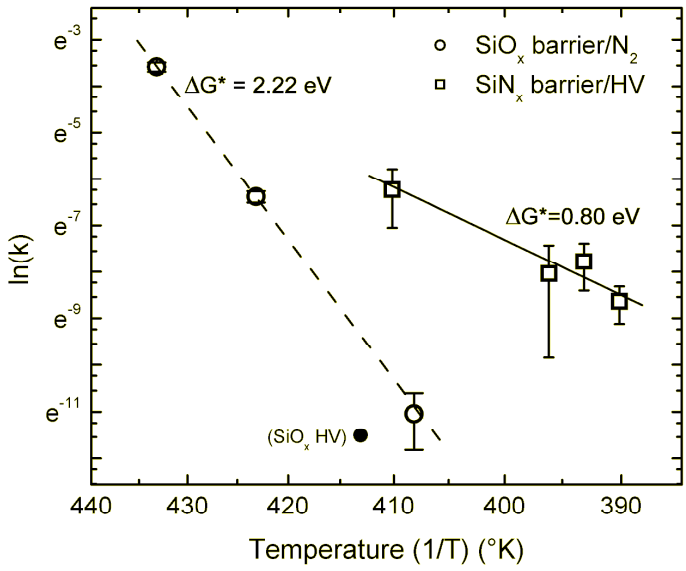

Figure 7.2. Avrami coefficient *k* versus the reciprocal temperature for Ag films on SiO_x and SiN_x barrier layers. The large disparity in the slopes of the lines indicates different controlling processes for the recrystallization.

representing the activation energy for the governing processes for texture evolution. The large difference in the slopes, which represent activation energies, for the two samples indicates very different controlling processes. Assuming two dimensional growth the slopes represent activation energies of 2.2 and 0.8 eV for the films on SiO_x and SiN_x, which suggest bulk and grain boundary diffusion mechanisms for growth, respectively. This large dissimilarity does not appear to be due only to the difference in the annealing ambient—included in Fig. 7.2 is a single point for recrystallization of the film on SiO_x in high vacuum, which is similar to the behavior in nitrogen. One explanation for the difference between the two samples may be due to large surface roughness observed for the SiO_x barrier layer.

Insights into the microstructural evolution of the films can also be garnered by analyzing the widths of the diffraction peaks during the recrystallization (not shown here). The widths of the off-normal (240) peaks in the (001) texture decrease rapidly as f^{001} begins to increase. This corresponds to rapid growth of the first (001) grains, which then dominate the diffracted intensity. Conversely, the widths of the diffraction peak from the (111) texture component remain unchanged during the entire recrystallization, indicating little or microstructural change in this subset of grains. This is consistent with preliminary electron backscattered diffraction images which show pockets of small (111) oriented grains located at triple junctions between abnormally large (001) grains.

7.4.2 Stress Analysis

Using the $sin^2\psi$ analysis, assuming the out-of-plane stress is zero, both the unstrained lattice parameter and biaxial in-plane stress can be calculated for both texture components. However, care must be taken when making this assumption for

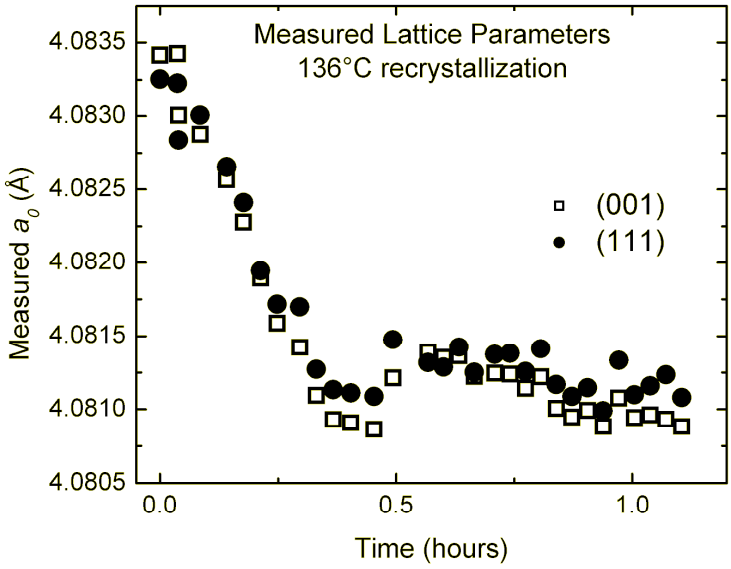

Figure 7.3. Lattice parameters calculated using the assumption of a biaxial stress state for both texture components in the 1300 nm Ag film on the SiN_x barrier.

passivated films, as interactions between the anisotropic texture components may lead to significant out-of-plane stresses [4]. The biaxial stress state assumption appears to be adequate for the present samples. A plot of the calculated unstrained lattice parameters is shown in Figure 7.3 during an isothermal anneal at 136°C. Similar behavior was seen for all recrystallizations of the 1300 nm film on SiN_x. The lattice parameters in both orientations change in concert, indicating a real change in a_0 and not a measurement artifact due to the biaxial stress state assumption. This change could arise due to some compositional change of the Ag film, such as the expulsion of Argon trapped in the lattice during the sputtering process.

Typical stress and evolution data during recrystallization are shown in Figure 4 for a sample annealed at 117°C. Features of this data set are similar to those observed at all other temperatures. The largest changes in stress for both the (111) and (001) orientations occurred when fraction of the film recrystallized was <10%. Stresses then remained constant for the majority of the secondary grain growth until the transformation was about 70% complete, when the stress in the (111) orientation began to relax. The most important feature of these data is that the (001) texture component develops virtually unstrained. Only very early on during the nucleation stage of recrystallization is any stress measured in grains with an (001) orientation. This is due to the small (001) grains being compressed by the surrounding stressed (111) matrix. Later in the recrystallization, a similar grain interaction comes into play as the isolated, now minority, (111) oriented grains relax into the surrounding unstrained (001) texture.

7.5 DISCUSSION

A previous study characterized the strain energy driving force prior to grain growth for copper films on silicon substrates [7]. For these measurements out-of-plane peaks were measured to characterize the full strain state in the sample using a lattice parameter determined at room temperature. The variation in the measured lattice parameters reported above demonstrate how important it is to include the off-axis peak for each strain measurement. Without these peaks there is no way of knowing the lattice parameter changes and the change would be manifest as errors in the strains.

The strain-free growth of the (001) oriented grains is significant because models used to predict the preferred orientations of thin films typically assume the strain energy driving force is determined by differences in elastic properties or yields strengths. The strain free growth also raises an important question: If strain free grains can be grown, why favor the high surface energy (001) orientation? The answer must be that the strain energy minimizing (001) grains are favored during the nucleation stage of recrystallization. The eventual strain free growth can then be explained by elimination of free volume within the film as the preferred (001) nuclei grow. The change in strain $\Delta\varepsilon$ due to grain growth eliminating free volume at grain boundaries given by

$$\Delta\varepsilon = \delta\left(\frac{1}{d_i} - \frac{1}{d_f}\right), \tag{7.1}$$

where δ is the grain boundary width and d_i and d_f are the initial and final grain diameters, respectively. Therefore, as the preferred low strain-energy (001) nuclei grow their energies are further reduced, increasing the preference for their development. In Figure 7. 4 the difference in strains corresponding to the stress difference is about 0.0005. This is roughly the limiting change in strain possible for an

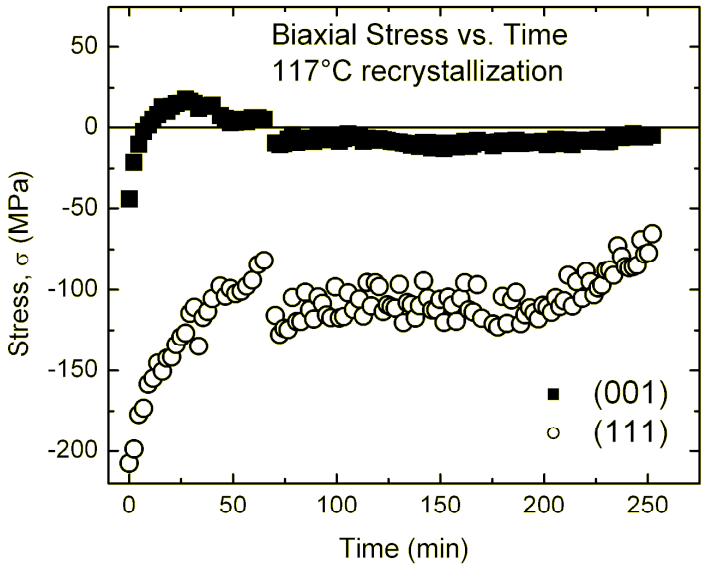

Figure 4. Biaxial stress vs. Time for the 1300nm Ag film during recrystallization at 117°C.

initial grain size of 200 nm and a grain boundary width of 1 Å, which are reasonable values. This correction to the driving force must be made, and though it has been proposed [3], has rarely been applied.

Due to abnormal grain growth, texture interactions play a role only in the early and late stages of texture evolution. Effects of stress interactions between texture components will be limited to regions near the grain boundary [6]. Therefore, interactions are expected to become much more dominant for small grains surrounded by the opposing texture component. These grain interactions are likely the reason the recrystallization did not run to completion, as the minority (111) grains are robbed of strain energy by relaxing into the unstrained (001) matrix. Interactions between texture components will likely play a much larger role in the microstructural evolution of films with typical grain sizes approximately equal to the film thickness [2].

7.6 CONCLUSIONS

Real-time *in-situ* x-ray diffraction has been used to simultaneously characterize texture and the stress state in an evolving silver film microstructure. The kinetics of recrystallization were very different for two seemingly similar films deposited on different barrier layers. An activation energy of 0.8 eV for the film on SiN_x is roughly that of grain boundary diffusion, while the larger energy of 2.2 eV for the film on SiO_x suggests a bulk diffusional process. It was also shown that the standard iso-strain model for predicting the strain energy driving force is not applicable, as secondary grains grew predominantly strain-free. The selection of the strain-energy minimizing (001) orientation occurred very early in the recrystallization process during the nucleation stage. Due to abnormal grain growth of the secondary grains, interactions between the elastically anisotropic (111) and (001) texture components were limited to the early and late stages of the texture evolution.

7.7 ACKNOWLEDGEMENTS

This work is based upon research conducted at the Cornell High Energy Synchrotron Source (CHESS) which is supported by the National Science Foundation and the National Institutes of Health/National Institute of General Medical Sciences under NSF award DMR-0225180. Support for this work was provided through an Applied Materials Graduate Fellowship. The authors would like to thank Arthur Woll and Ray Fertig for their assistance and helpful discussions.

REFERENCES

1. Thompson CV. Annual Review of Materials Science 2000; 30: 159.
2. Sonnweber-Ribic P, Gruber P, Dehm G, Arzt E. Acta Materialia 2006; 54: 3863.
3. Thompson CV, Carel R. Journal of the Mechanics and Physics of Solids 1996; 44: 657.
4. Vodnick AM, Nowak DE, Baker SP. to be submitted 2008.
5. Ozcan AS, Ludwig KF, Lavoie C, Cabral C, Harper JME, Bradley RM. Journal of Applied Physics 2002; 92: 5189.
6. Baker SP, Kretschmann A, Arzt E. Acta Materialia 2001; 49: 2145.
7. Zielinski EM, Vinci RP, Bravman JC. Applied Physics Letters 1995; 67: 1078.
8. Nowak DE, Blasini DR, Vodnick AM, Blank B, Tate MW, Deyhim A, Smilgies DM, Abruna H, Gruner SM, Baker SP. Review of Scientific Instruments 2006; 77: 113301.
9. Vinci RP, Zielinski EM, Bravman JC. Thin Solid Films 1995; 262: 142.
10. Porter DA, Easterling KE. Phase Transformations in Metals and Alloys: Chapman & Hall, 1992.

Chapter 8

Summary and Outlook

This thesis has been dedicated toward understanding the partitioning of stresses amongst the different texture components of FCC metal films and the impact this has on stress-driven phenomena.

A new x-ray strain analysis was developed and used to characterize, for the first time, 3-D stress states within the (111) and (100) texture components of a mixed texture Cu film (§3). This new analysis showed that stress states are drastically different than previously reported in the literature—nearly isostress behavior in-plane, compared to previously reported behaviors near isostrain, with large out-of-plane stresses, compared to the widespread assumption that these stresses are equal to zero. The triaxial stress states characterized with x-ray diffraction were shown to be reasonable using finite element models of idealized grain structures in mixed texture films (§5). This enhanced description of the stress partitioning throughout the microstructure of mixed texture films should influence the understanding of all stress driven processes.

The 3-D stress states characterized with x-ray diffraction in (§3) arose due to significant strain transfer between (111) and (100) oriented grains. However, these interactions obscure the total strain in each texture component, and therefore the distinction between elastic and plastic strain, making it difficult to accurately describe plastic deformation processes such as strain hardening and anelastic recovery (one cannot simply subtract the elastic strain measured using x-ray diffraction from the applied strain to get plastic strain). Thus, an analyses was developed in §4 to calculate the required changes in plastic strain and dislocation density within each orientation

over a temperature cycle. This analysis demonstrated that the (111) texture component never deforms purely elastically, exhibiting significant anelastic behavior immediately upon unloading. The (100) orientation, in contrast, deforms elastically on unloading until the stress nears zero, when dislocation loops begin to close. This difference in behavior between the (111) and (100) orientations can be attributed to the very different dislocation densities required to achieve the applied deformations within these two orientations, with the (111) orientation requiring more than twice as many dislocations, which then form pile-ups providing a backstress for reverse deformation. This analysis (§4) also demonstrated that the (111) and (100) orientations have very different hardening behaviors, with the (100) orientation hardening more than twice as fast per dislocation. The controlling mechanisms are unclear, though some causes for the difference in hardening may include variations in dislocation interaction strengths between the two orientations, different dislocation source densities, or different twin densities or grain sizes.

Texture evolution is a stress driven process which may be directly addressed by the improved descriptions of stress partitioning provided in this thesis. The stability of mixed (111)/(100) textured films has provided a long standing problem for the thin film community. Thus far, the accepted model for texture selection is thermodynamic, and predicts either a (111) or (100) orientation, depending on strain and film thickness, but cannot account for the prevalence of mixed texture. For the first time, in this thesis, a mechanism was proposed to explain the stability of mixed texture films over a wide range of film thickness (§5), based on the distribution of strain energies found in films with broad ranges of grain size.

Peak widths from x-ray diffraction strain measurements are commonly used to gain insights into dislocation processes during loading. In this thesis (§6), it was demonstrated that inhomogeneous strains arising from texture interactions in thin

films contribute significantly to the widths of diffraction peaks, which in combination with dislocation broadening, leads to perfect reversibility of diffraction peaks during thermal cycling. The knowledge that texture interactions can lead to substantial broadening will allow for improved x-ray investigations of deformation processes.

Experimental characterization of texture evolution was also presented (§7), using *in-situ* x-ray diffraction techniques to characterize the average strains within the (111) and (100) texture components of an evolving Ag film microstructure. Preferred nucleation and growth of (100) oriented grains in a (111) oriented matrix rapidly decreases the strain energies of these grains, increasing the preference for them in further growth, leading to abnormal grain growth. Future work investigating texture evolution will benefit from similar analyses in order to provide the average strain energies in the different texture components of evolving microstructures.

Superior descriptions of stress partitioning in thin films, and improved *in-situ* characterization methods, will aid in the understanding of stress driven phenomena in thin films. Based on the work presented in this thesis, there are many opportunities for future research, some of which include:

- Strain hardening and anelastic behaviors: The elastic and plastic strain analyses presented in §3 and §4, respectively, and insights into stress states and deformation processes contained in these chapters, offer useful tools and insights to address the classic materials science problem of uncovering structure-property relationships. *In-situ* characterization of films with different thicknesses, interfacial properties, and thermal histories should be performed using these improved analyses in order to understand the controlling deformation mechanisms. Since large stresses often drive failure mechanisms, understanding these features is critical for improving the reliability of devices containing thin film metallizations.

- Texture evolution: A texture-dependent grain size analysis, coupled with x-ray strain measurements (§3) and finite element models (§5) of the stresses in the (111) and (100) texture components of a stabilized mixed texture microstructure will allow the mechanism for mixed texture films stability, presented in §5, to be explored, tested and expanded. Since this model for mixed texture stability is based on different aspect ratio grains being stable in different orientations, the texture-dependent grain size analysis can be referenced against texture map, predicted by FEM, similar to Figure 5.5, for films with different thickness and annealed at different strains. Understanding the thermodynamics of this stable grain structure is a step toward developing tailored microstructures.
- Texture evolution: *In-situ* x-ray analyses of strains within each orientation of an evolving microstructure during annealing (§7) will help to understand recrystallization processes, with the goal of producing tailored microstructures. An emphasis should be placed on the conditions required for nucleation and growth of secondary grains (strain, temperature, initial microstructure), the density of which will control the characteristics of the stabilized grain structure. Finite element models of strain energies in grains with densification strains (arising from grain growth) will be useful in support of these investigations to provide information on how the strain energy varies within a growing grain.
- Strain distributions: The systematic spatial distribution of the resolved shear stresses in (111) and (100) grains, arising due to texture interactions, (in instead of the average stresses reported in §5) will provide insights into the dislocations behaviors, and thus strain hardening, in each orientation. For instance, if we imagine the in-plane stress as the key driver for

dislocation motion a potentially interesting behavior is easily described. To maintain stress equilibrium at texture boundaries, the in-plane stress in each orientation must be equal across these boundaries. However, in the (100) orientation the stress is expected to decrease with distance away from the boundary, while the stress in the (111) orientation is expected to increase with increasing distance from the boundary. Since dislocation nucleation is likely to occur at grain boundaries, two very different behaviors may be expected in the two orientations: (1) In the (100) orientation, the texture boundary is at a maximum stress to nucleate dislocations. As the dislocation moves away from the boundary into a region of lower stress it may become stagnant in the center of the grain, or linger in the grain center long enough for interaction with another dislocation. (2) In the (111) orientation, the texture boundary is at a minimum stress. Thus, as a dislocation moves across the grain it may never see a stress below the critical nucleation stress, such that the dislocation can quickly traverse the grain to the opposite boundary. Of course, a proper analysis of this sort must include the local triaxial stress state, as may be determined from FEM.

Many other stress driven processes in mixed texture films could also be addressed based on the knowledge of stress partitioning presented in this thesis (*e.g.* electromigration, stress voiding, hillocking, diffusional relaxation, fracture, delamination). Progress made in this thesis represents another step toward understanding structure-property relationships in thin films. Eventually, efforts in this field will allow for materials and microstructures to be engineered for specific applications, improving device performance, reliability, and manufacturability.

APPENDIX 1

The $sin^2\psi$ equation

For a strain tensor ε_{ij} in sample coordinates, the normal strain, ε_ψ, along a unit vector n_i at an angle ψ from the film normal is given by $\varepsilon_\psi = \varepsilon_{ij} n_i n_j$. Since the focus of this thesis is films with fiber texture, in-plane orientations are unimportant and we can consider the strains within a single plane, simplifying the derivation. The coordinate system is defined in Figure A1.1 (similar to Fig 2.1), along with a description of the components for n_i,

$$n_i = \begin{bmatrix} 0 \\ \sin\psi \\ \cos\psi \end{bmatrix}. \tag{A1.1}$$

With ε_{ij} in the form of Eq. 1.3, ε_ψ becomes

$$\varepsilon_\psi = \varepsilon_{22}\sin^2\psi + \varepsilon_{33}\cos^2\psi, \tag{A1.2}$$

which, using the identity $\sin^2\psi + \cos^2\psi = 1$, can be written as

$$\varepsilon_\psi = \varepsilon_{22}\sin^2\psi + \varepsilon_{33}\left(1 - \sin^2\psi\right). \tag{A1.3}$$

Rearranging Equation A1.3 gives the well known $sin^2\psi$ equation

$$\varepsilon_\psi = \left(\varepsilon_{22} - \varepsilon_{33}\right)\sin^2\psi + \varepsilon_{33}, \tag{A1.4}$$

where, throughout this thesis we have used the notation $\varepsilon_{22} = \varepsilon_f$ and $\varepsilon_{33} = \varepsilon_3$.

An analogous approach, common in the literature, is to perform a tensor rotation to calculate the strain along an angle ψ, $\varepsilon'_{33} = a_{3i}a_{3j}\varepsilon_{ij}$, which leads to a similar calculations, with the rotation matrix

$$a_{mn} = \begin{bmatrix} 1 & 0 & 0 \\ 0 & \cos\psi & \sin\psi \\ 0 & -\sin\psi & \cos\psi \end{bmatrix}. \tag{A1.3}$$

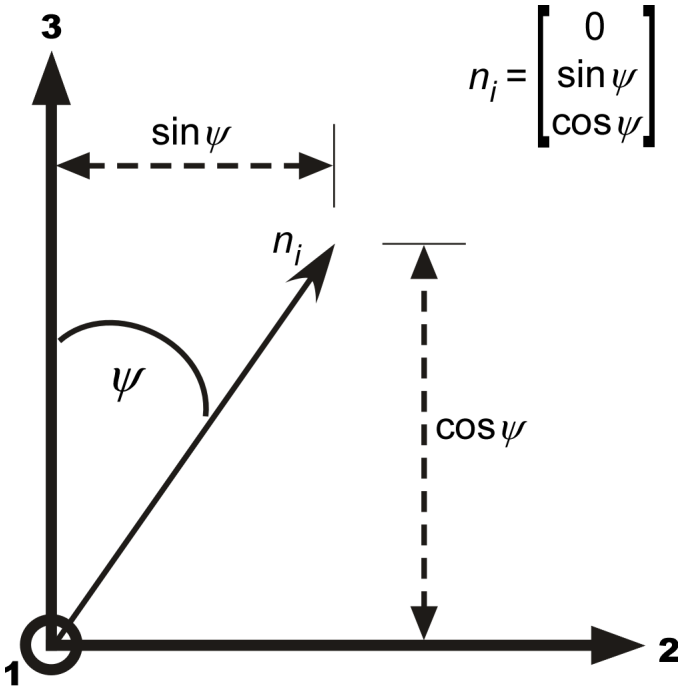

Figure A1.1. Coordinate system describing the unit vector, n_i, used in the derivation of the $sin^2\psi$ equation.

APPENDIX 2

Errors associated with incorrect biaxial stress assumption

A common assumption in x-ray analyses of thin films and surface layers is that the out-of-plane stress is zero everywhere in the film. As demonstrated in §3, this may not be the case. Here, it is demonstrated how this incorrect assumption will influence the results, showing the stress calculated with the biaxial stress assumption, σ_B, is equal to the difference between the actual in- and out-of-plane stresses in the sample, $\sigma_B = \sigma_f - \sigma_3$. While this relation has been commonly reported (for instance, Noyan, *Met. Trans. A*; 14, 249, 1982) the derivation is rarely presented.

This derivation will be performed for a (100) oriented grain using the Crystallite Group Method approach as discussed in §3. While the details of the calculation are specific, the same results could be found for the (111) texture component, or an isostropic film (discussed in §2), by comparing the solutions for stress under an assumed biaxial and triaxial stress state.

For a (100) textured film under a triaxial stress state $\left(\sigma_1 = \sigma_2 = \sigma_f \neq \sigma_3\right)$ it can be shown that (Eq. 3.10)

$$a_\psi^{100} = a_0\left(S_{11} - S_{12}\right)\left(\sigma_f^{100} - \sigma_3^{100}\right)\sin^2\psi + 2a_0 S_{12}\sigma_f^{100} + S_{11}a_0\sigma_3^{100} + a_0 . \qquad \text{(A2.1)}$$

For a biaxial stress state, $\sigma_3 = 0$, this equation becomes (Eq. 2.16)

$$a_\psi^{100} = a_0\left(S_{11} - S_{12}\right)\left(\sigma_B^{100}\right)\sin^2\psi + 2a_0 S_{12}\sigma_B^{100} + a_0 , \qquad \text{(A2.2)}$$

which has the slope, *m*, and intercept, *b*,

$$m = a_0\left(S_{11} - S_{12}\right)\left(\sigma_B^{100}\right), \qquad \text{(A2.3)}$$

$$b = 2a_0 S_{12}\sigma_f^{100} + S_{11}a_0\sigma_3^{100} + a_0 . \qquad \text{(A2.4)}$$

By solving Eq.'s A2.3-4 for a_0 and setting these equal to each other, we find

$$m + 2mS_{12}\sigma_B^{100} = b(S_{11} - S_{12})\sigma_B^{100}, \tag{A2.5}$$

which can be solved for the biaxial stress which is measured when a biaxial stress state is assumed,

$$\sigma_B^{100} = \frac{m}{b(S_{11} - S_{12}) - 2mS_{12}}. \tag{A2.5}$$

This important result must be contrasted with the result when a similar procedure is followed for a triaxial stress state. The slope, *m*, and intercept, *b*, of the $sin^2\psi$ line for the (100) orientation under a triaxial stress state (Eq. A2.1) are

$$m = a_0(S_{11} - S_{12})(\sigma_f^{100} - \sigma_3^{100}), \tag{A2.6}$$

$$b = a_0(2S_{12}\sigma_f^{100} + S_{11}\sigma_3^{100} + 1). \tag{A2.7}$$

Solving these equations for a_0, setting them equal to each other, and solving for σ_f^{100}, yields

$$\sigma_f^{100} = \sigma_3^{100}\left[\frac{b(S_{11} - S_{12}) - mS_{11}}{b(S_{11} - S_{12}) - 2mS_{12}}\right] + \frac{m}{b(S_{11} - S_{12}) - 2mS_{12}}. \tag{A2.8}$$

The term on the far right is equal to the biaxial stress calculated when a planar stress state is assumed (Eq. A2.5), giving

$$\sigma_B = \sigma_f^{100} - \sigma_3^{100}\left[\frac{b(S_{11} - S_{12}) - mS_{11}}{b(S_{11} - S_{12}) - 2mS_{12}}\right]. \tag{A2.9}$$

Now, the multiplier on σ_3^{100} must be addressed and simplified. The slope of a $sin^2\psi$ line is related to the distortion of the unit cell from its unstrained position, and the intercept is equal to the unstrained value minus some distortion. Since elastic distortions are small, it is clear that $m << b$. Thus, since the compliance constant coefficients S_{ij} are the same order of magnitude the terms with *m* are negligible and this multiplier reduces to unity.

$$\left[\frac{b(S_{11}-S_{12})-mS_{11}}{b(S_{11}-S_{12})-2mS_{12}}\right]\approx 1, \tag{A2.10}$$

Hence, we find the result that if a biaxial stress state is incorrectly assumed, the measured stress, σ_B ,will be equal to

$$\sigma_B = \sigma_f^{100} - \sigma_3^{100}. \tag{A2.9}$$